Physik-Department

Model Selection for Partial-Wave Analysis of $\pi^- + p \to \pi^-\pi^+\pi^- + p$ at the COMPASS Experiment at CERN

Diplomarbeit von Oliver Johann Drotleff

Technische Universität München

Technische Universität München
Physik-Department E18

Model Selection for Partial-Wave Analysis of $\pi^- + p \to \pi^-\pi^+\pi^- + p$ at the COMPASS Experiment at CERN

Oliver Johann Drotleff

Erstgutachter (Themensteller): Prof. Dr. Stephan Paul
Zweitgutachter: Prof. Dr. Allen Caldwell

Die Diplomarbeit wurde am 02.11.2015 eingereicht.

Contents

CHAPTER 1

Introduction

Ever since the discovery that atomic nuclei are positively charged, scientists wondered what counteracts the electrostatic repulsion and holds them together. In an article from 1934, Yukawa predicted that the nuclear force is carried by a particle of approximately 200 times the mass of an electron. This particle was first observed in 1947 in cosmic-ray experiments using photo-emulsion plates and was called the *pion*. Soon after this initial breakthrough, the usage of particle accelerators became common and many other short-lived, strongly-interacting particles were discovered in inelastic scattering experiments and were named *hadrons*. It was now up to the theorists to classify these new particles in a conclusive model.

The first attempt at such a theoretical model was made independently by Gell-Mann and Ne'eman called the *Eightfold Way*. It organized the hadrons into octets (see figure 1.1), using a new quantum number, the Strangeness S, in addition to the charge, to differentiate between the hadrons. The additional symmetry connected to S directly led to the proposition of the *Constituent Quark Model* (CQM) by Gell-Mann and Zweig, suggesting that hadrons are comprised of spin-½ constituents called *quarks*.

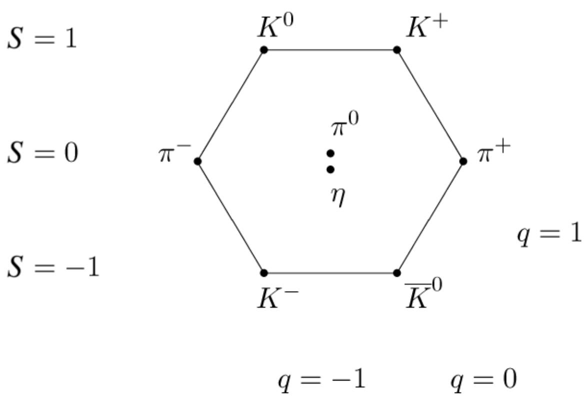

Figure 1.1: The meson octet for spinless mesons with negative parity. Particles on the same horizontal line have the same strangeness, the meson charge is constant on diagonal lines.

The discovery of the Δ^{++} baryon, which consists of three up-quarks with parallel spins, posed a challenge for the quark model: Since quarks are fermions, the Δ^{++} seemed to violate the Pauli principle. Therefore, in 1965 an additional SU(3) degree of freedom for quarks, called *color charge*, was proposed alongside gauge-bosons, the *gluons*, that were responsible for the interaction between quarks. This lead to the development of the quantum field theory of the strong interaction which is called *quantum chromodynamics*. The name already hints that it was constructed in analogy to quantum electrodynamics, but there are important differences between the two theories. Gluons, unlike their electromagnetic counterparts, the photons, which carry no electric charge, do carry color charge and can therefore interact with one another. This has large consequences for the way hadrons behave.

One phenomenon of the strong force is called *confinement*, which describes the effect that the attracting force between two quarks does not decrease when they are separated. Therefore, when a quark is pulled out of a hadron, the creation of a new quark-antiquark pair is energetically favourable. Confinement is the reason that there has never been an observation of a free quark. Another property of the strong force is the *asymptotic freedom*, which means that quarks interact only weakly at high energy scales. At the energy scale of hadrons, the coupling is in the order of 1. Therefore perturbation theory, called *perturbative QCD* (pQCD), does not converge at low energies.

In the following text, the two most important theoretical concepts, the constituent quark model and quantum chromodynamics, are looked at closer in the context of light mesons[1]. Thereafter, the experimental side of light-meson spectroscopy is addressed. This is followed by a chapter on the COMPASS experiment, which provided the data for this analysis and finally the structure for the remainder of the thesis is explained.

1.1 Light Mesons

1.1.1 Constituent Quark Model

In the constituent quark model, mesons are the simplest hadron. They represent a bound quark and antiquark system. The spins of the two quarks can couple to the total spin S in two different ways:

$$\begin{aligned} |\uparrow\downarrow\rangle \ &: \ S = 0 \\ |\uparrow\uparrow\rangle \ &: \ S = 1 \end{aligned} \tag{1.1}$$

A relative orbital angular momentum L between the two quarks couples with the spin S to the total angular momentum J, which is equal to the spin of the meson:

$$|L - S| \leq J \leq L + S \tag{1.2}$$

[1] Mesons that contain only u,d and s quarks.

The combination of the intrinsic parities of the quark (= +1), the antiquark (= −1) and the spatial wave function with the angular momentum L ($= -1^L$) results in the total parity P of the meson:

$$P = (+1)(-1)(-1)^L = (-1)^{L+1} \tag{1.3}$$

If the meson satisfies the equation $P = (-1)^J$, it is defined to have the positive naturality $\eta = +1$. In case of $P = (-1)^{J+1}$ the naturality is negative with $\eta = -1$. Therefore the naturality is defined as

$$\eta = P(-1)^J \tag{1.4}$$

The C-parity is another multiplicative quantum number that describes the symmetry of the particle under charge conjugation. A neutral meson, which consists of a quark and the respective antiquark, is a C-parity eigenstate with eigenvalue

$$C = (-1)^{L+S}. \tag{1.5}$$

Charged mesons with the z component of the isospin $I_3 \neq 0$ are not eigenstates, but by convention the C-parity of the neutral isospin partner state is assigned to them. To extend the C-parity to charged states, one can introduce the G-parity, which is a multiplicative quantum number defined for all non-strange mesons. It is defined as the charge conjugation, followed by a 180° rotation around the y-axis in isospin space. The latter corresponds to a charge reversal.

$$G = Ce^{\imath\pi I_2} = C(-1)^I \tag{1.6}$$

The G-parity is a good quantum number for all non-strange, light mesons. Based on the definitions of the quantum numbers, the mesons listed in table 1.2 can be constructed in the CQM. The rules forbid certain J^{PC} combinations, which is why they are called *spin-exotic*:

$$J^{PC} = 0^{--}, \text{even}^{+-}, \text{odd}^{-+} \tag{1.7}$$

1.1.2 Quantum Chromodynamics

The constituent quark model is quite successful in classifying hadrons and, considering its simplicity, it predicts the masses of many hadrons reasonably well. However, exact calculations using potential models fail, because on this energy scale the quarks in the meson can not be regarded as quasi-free and the perturbation approximation breaks down. The mass is then dominated by self-interaction of quarks and gluons that cannot be calculated by current models.

Even today it is impossible to calculate the light-meson spectrum from first principles. One approach that is most promising in this respect is called *lattice QCD*. It performs a numeric simulation of QCD on a grid in space and time using the grid spacing a. Since the computations are dimensionless, a physical scale has to be established, which is done by fixing the mass of the pion. The challenge of lattice QCD is that it is computationally very expensive. The computing costs scale with a^{-6} and m_π^{-2} [1]. The reason for the rising costs with smaller pion masses is the amount of vacuum loops that have to be calculated. An example for a state-of-the-art calculation in the field of meson spectroscopy is shown in figure 1.2, which was calculated using a lattice spacing of $a = 0.12\,\text{fm}$ and an unphysically large pion mass of $m_\pi = 396\,\text{MeV}/c^2$. Although the mesons are shifted to

J	L	S	I	$I^G J^{PC}$	Mesons	Type
0	0	0	0	0^+0^{-+}	$\eta, \eta'(958), \ldots$	Pseudo-scalar
0	0	0	1	1^-0^{-+}	$\pi, \pi(1300), \pi(1800), \ldots$	
0	1	1	0	0^+0^{++}	$\sigma, f_0(980), \ldots$	Scalar
0	1	1	1	1^-0^{++}	$a_0(980)$	
1	0	1	0	0^-1^{--}	$\omega(782), \phi(1020), \ldots$	Vector
1	0	1	1	1^+1^{--}	$\rho(770), \ldots$	
1	1	0	0	0^-1^{+-}	$h_1(1170), \ldots$	Pseudo-vector
1	1	0	1	1^+1^{+-}	$b_1(1235), \ldots$	
1	1	1	0	0^+1^{++}	$f_1(1285), \ldots$	Axial-vector
1	1	1	1	1^-1^{++}	$a_1(1260), \ldots$	
2	2	1	0	0^+2^{-+}	$\eta_2(1645), \ldots$	Tensor
2	2	0	1	1^-2^{-+}	$\pi_2(1670), \pi_2(1880), \ldots$	
2	1	1	0	0^+2^{++}	$f_2(1270), \ldots$	Tensor
2	1	1	1	1^-2^{++}	$a_2(1320), \ldots$	

Table 1.2: Overview of the allowed meson states with $J \leq 2$ within the constituent quark model.

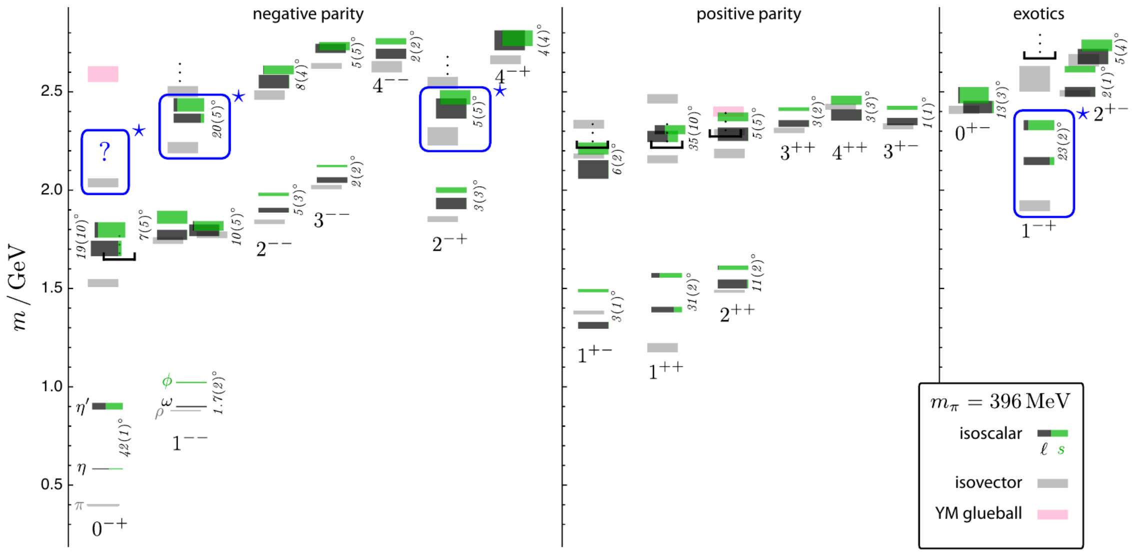

Figure 1.2: Light-meson spectrum derived from lattice QCD calculations.

higher masses, most experimentally confirmed resonances can be identified. Additionally, in the right column, some resonances are predicted in the spin-exotic sector, which do not exist in the constituent quark model. This includes resonances that are not predicted by the quark model including resonances in the spin-exotic regime.

The continuing technological progress will undoubtedly lead to better predictions of the light-meson spectrum, as the pion mass will be reduced to realistic values.

1.1.3 Light-Meson Spectroscopy Experiments

As always in physics, the theories have to be experimentally confirmed or invalidated. With the discovery of many light mesons in the 60s and 70s, it was presumed that most of their spectrum was discovered. With the increasing center-of-mass energies accelerators could achieve, high-energy experiments were focused, which showed good success within the approximation of perturbative QCD.

But for the last 20 years, a revival of light-meson spectroscopy could be observed. Several experiments around the world put their efforts into exploring the physics of non-perturbative QCD, hunting for exotic states. The analysis in this thesis is performed with data from the COMPASS experiment at CERN; other experiments researching light mesons include the GlueX and CLAS at JLab (US) and the VES collaboration (RUS).

There are different types of experiments to perform hadron spectroscopy, the two most common being formation and production experiments. In *formation experiments*, two colliding particles form a resonance. When this happens the cross section of the reaction peaks at a certain center-of-mass energy. The downside of this method is, that the possible quantum numbers of the resonance are limited by the colliding particles and their energy. In *production experiments*, which the COMPASS experiments belongs to, a constant high-energy beam collides with a target. A resonance is not identified by changes in the cross section at certain center-of-mass energies, but rather by peaks in the final-state invariant mass spectrum. This makes finding resonances harder than in formation experiments, because one has to first consider all accessible final states. But the advantage is that more resonances are accessible with this method.

1.1.4 Meson Production in Diffractive Dissociation

The *production mechanism*, meaning the physical process that creates the resonance, exploited at the COMPASS experiment is called *diffractive dissociation*. It describes a scattering reaction mediated by the strong force, where an incoming beam hadron collides with a target. Through strong interaction with the target, the beam particle is excited into an intermediate state X, which dissociates into the final state. The reaction explored in this thesis is that of a negatively charged $190\,\mathrm{GeV}/c$ beam pion interacting with a proton target. The produced excited intermediate state then decays into a final state

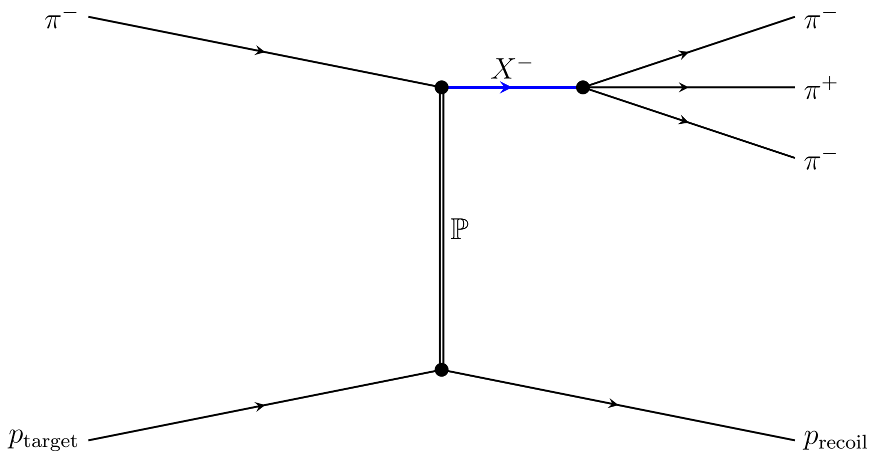

Figure 1.3: Diffractive dissociation of a beam pion on a target proton into the three charged pion final state.

comprised of two negatively and one positively charged pion. The target proton stays intact:

$$\pi^- \, p \rightarrow \pi^- \, \pi^+ \, \pi^- \, p \tag{1.8}$$

Figure 1.3 visualizes this reaction. The exchange particle $\mathbb{P}$ that excites the beam pion is the *pomeron*. It is a hypothetical, strongly-interacting quasi-particle that carries vacuum quantum numbers. This allows us to calculate the possible quantum numbers of the resonances X^-. Since the strong interaction conserves isospin and G-parity, the X^- has to obey $G = -1$:

$$G(X^-) = G(\pi) \cdot G(\mathbb{P}) = G(\pi)^3 = -1 \tag{1.9}$$

Because the final-state pions carry a charge of -1, the resonance has to have at least an isospin of 1 ($I \geq 1$). Isospin $I = 1$ is assumed, because no flavour-exotic mesons with isospin $I = 2$ have been observed so far. With equation (1.6) we can immediately conclude, that $C = +1$. This leaves us only with the possible J^P combinations. We can immediately rule out the combination of $J^P = 0^+$. This is because a spinless state with positive parity cannot decay $\pi^-\pi^+\pi^-$. All other J^P combinations are accessible.

The invariant mass of the X^- is the most important kinematic variable of the reaction. It can be calculated from the four-momenta $p_{\pi,i}$ of the final state pions:

$$m_X^2 = m_{3\pi}^2 = \frac{p_X^2}{c^2} = \frac{\left(\sum_{i=1}^{3} p_{\pi,i}\right)^2}{c^2} \tag{1.10}$$

Another important kinematic variable is the Mandelstam variable t, which is the squared four-momentum transfer between the beam and the target:

$$t = -(p_{\mathrm{beam}} - p_X)^2 = (p_{\mathrm{target}} - p_{\mathrm{recoil}})^2 < 0 \tag{1.11}$$

A downside of using t as a kinematic variable is, that its spectrum does not start at $t = 0$, since even at forward scattering angles there is a small momentum transfer required in order to excite the pion to X.

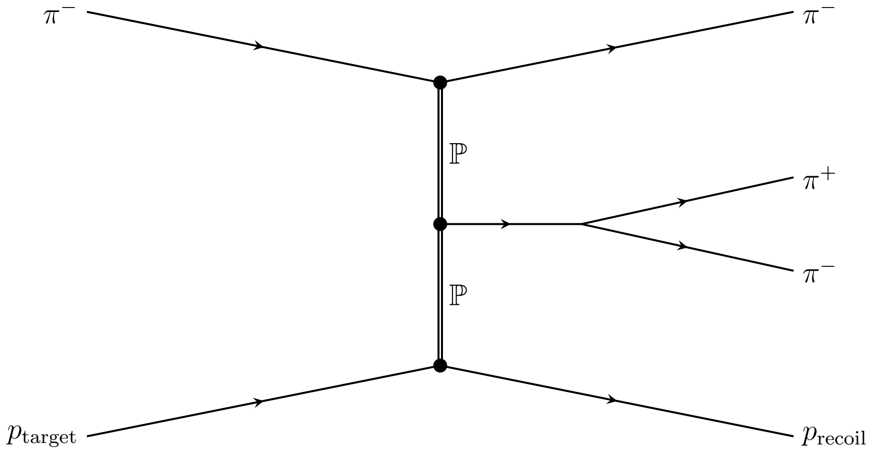

Figure 1.4: Central production reaction leading to a three-charged-pion final state.

Therefore, in this analysis, we will subtract this minimum momentum transfer and define the *reduced four-momentum transfer squared* t':

$$t' = |t| - |t|_{\text{min}} \geq 0 \tag{1.12}$$

1.1.5 Other Production Mechanisms

Besides diffractive dissociation, the $\pi^-\pi^+\pi^-$ final state can also be obtained by other production mechanisms, which enter the data set as potential backgrounds. This section will cover the two mechanisms that have the largest effect on the data.

Central Production

The first alternative production mechanism is *central production*. The process is shown in figure 1.4. The initial and final state are the same as in diffractive dissociation, but here the final state is produced by double-pomeron exchange. The two pomerons create an intermediate state that decays into two charged pions. Since there is no three-pion intermediate state, the kinematic signature of both processes is different. Therefore, it can be partially separated from diffractive dissociation in the event selection process, as described in section 1.2.3.

Deck-Effect

Another production mechanism is the *Deck effect* [2], which is a reaction that also ends in the $\pi^-\pi^+\pi^-$ final state, but has no three-pion intermediate state (see figure 1.5). In this process, the pion beam decays into a two-pion resonance and a pion, which softly scatters off the proton via a pomeron. This

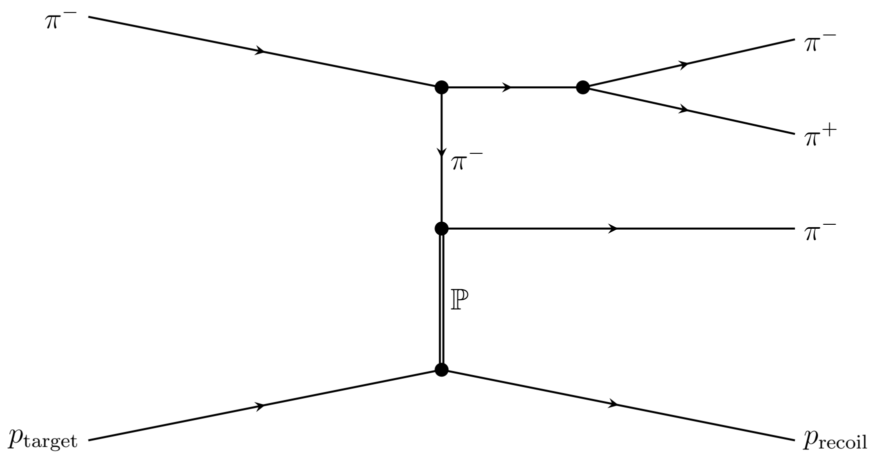

Figure 1.5: One possible diagram for the Deck effect resulting in the three-charged-pion final state.

process is hard to distinguish from diffractive dissociation and therefore enters as background into the data.

1.2 The COMPASS Experiment

The **Co**mmon **M**uon **P**roton **A**pparatus for **S**tructure and **S**pectroscopy is a high-energy fixed-target experiment at CERN in Geneva, Switzerland. The scientific goal of the experiment is to learn more about the structure and spectrum of hadrons in the region of non-perturbative QCD. COMPASS is located in the North Area of CERN and uses the M2 beam line which is fed by the Super Proton Synchrotron (SPS). The experiment is operating since 2002 and has undergone several modifications to accommodate different scientific goals. The flexible experiment layout and the M2 beam line, which is able to deliver different particle beams, make COMPASS a true multi-purpose experiment. The wide physics program includes muon scattering to measure i.e. the gluon polarization in the nucleon and spectroscopy in the light-meson sector.

1.2.1 The M2 Beam Line

Primary protons with a momentum of 400 GeV/c are extracted from the SPS and are then guided onto a 50 cm long beryllium production target called T6. The thickness of the target is adjustable which modifies the beam intensity as well as the composition of the secondary beam. Reactions in the production target create secondary hadrons. For the data analyzed in this thesis, a negatively-charged hadronic beam with 190 GeV/c momentum with the composition listed in table 1.3 was used. Particle identification of the different beam particles takes place in front of the COMPASS target in two Cherenkov detectors (CEDARs).

Particle	Fraction at T6 Target	Fraction at COMPASS Target
π^-	0.947	0.968
K^-	0.046	0.028
$\bar{p}$	0.007	0.008

Table 1.3: Main components of the negative hadron beam at the 50 cm T6 production target and the COMPASS target. [3]

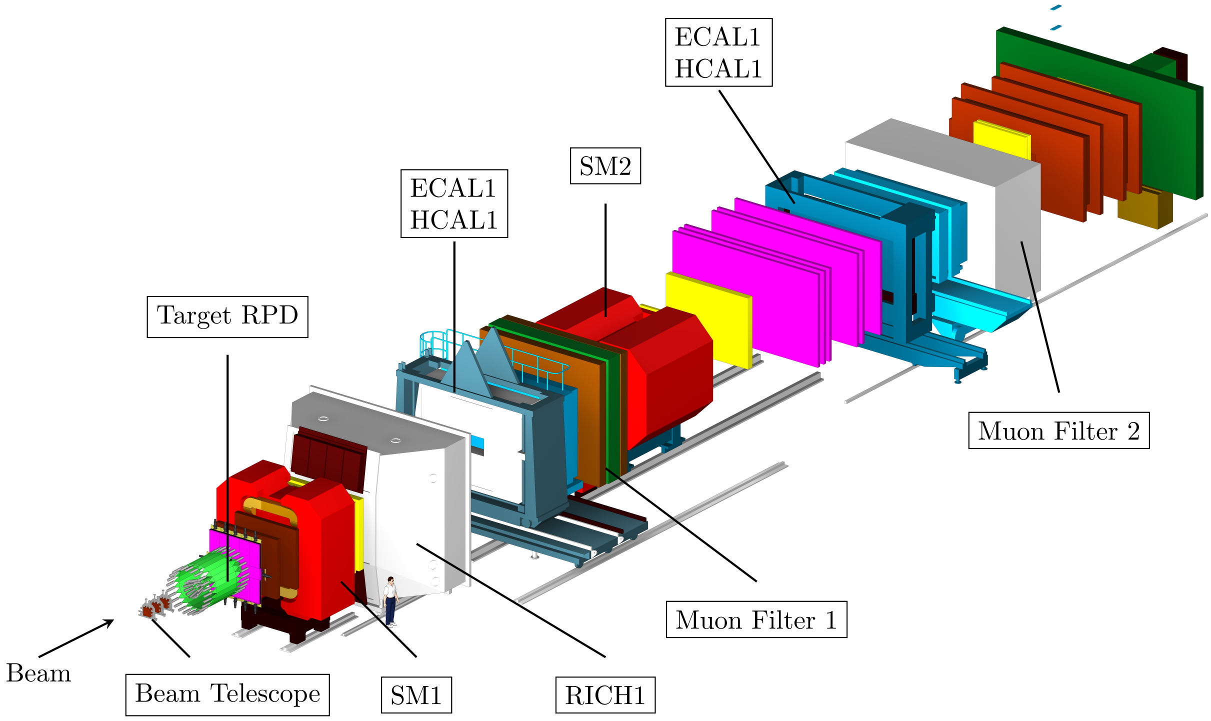

Figure 1.6: Schematic view of the COMPASS setup for the 2008 hadron-beam run.

1.2.2 Spectrometer Layout

In this section, the layout of the COMPASS experiment as of 2008, the year the data for this thesis was taken, will be described. A more detailed description of the spectrometer during the 2008 hadron run can be found in [4]. Figure 1.6 shows a schematic view of the spectrometer and its detectors. The layout can be intuitively divided into three parts: the target region, the large-angle spectrometer and the small-angle spectrometer (SAS).

Target Region

The target region consists of the target and its surrounding detectors. For the 2008 run a liquid-hydrogen target was used. The *Recoil-Proton Detector* (RPD), which is comprised of two cylindric barrels of scintillators, surrounds the target. It measures the recoil protons that are produced in diffractive reactions down to reduced four-momentum squared transfers $t' = 0.07\,(\mathrm{GeV}/c)^2$. To measure the beam trajectory, a beam telescope consisting of three silicon micro-strip detectors (Beam Telescope) is installed upstream of the target. Together with the information from two additional silicon detectors immediately downstream of the target, which measures the outgoing particles, the vertices can be reconstructed with high precision.

Large-Angle Spectrometer and Small-Angle Spectrometer

One of the requirements when designing the COMPASS experiment was to provide a wide angular acceptance while simultaneously maintaining a high tracking precision at small angles. To enable this, the detector uses a two-stage design with a weaker dipole magnet in the *Large Angle Spectrometer* (LAS) to measure low-momentum particles and a stronger magnet in the *Small Angle Spectrometer* (SAS) for high-momentum particles. Both stages are practically identical in their setup and use a multitude of tracking detectors. One difference is a *ring-imaging Cherenkov detector* (RICH), which is used for final state particle identification in the LAS.

1.2.3 Event Selection

As a first step of the analysis, the relevant data has to be filtered from the huge dataset that COMPASS provided during the 2008 hadron run. For this thesis, the same data as in [3] was used and therefore only a short summary of the event selection will be given. Cuts were applied to the data to eliminate unwanted events. The final data sample should be as pure as possible consisting of diffractively produced $\pi^-\pi^+\pi^-$ events.

The first cut was the one that selects diffractive dissociation events. For this task, a dedicated trigger system called *DT0 trigger* was installed at COMPASS, which is visualized in figure 1.7. It was a combination of three different triggers. The first trigger was a combination of the *beam counter* and the scintillating fiber *SciFi* and ensures that a single beam particle hit the target. Next in order was the *recoil-proton trigger*. In diffractive dissociation events, a slow recoil proton was expected to leave the target. The trigger required only one charged particle to pass through both rings of the RPD in a way as indicated in figure 1.8. The last component of the DT0 trigger was a combination of veto signals. The so-called *Sandwich Veto* eliminated events with particles that left the target outside of the geometrical acceptance of the spectrometer. The *Beam Killers*, two scintillating counters located downstream of SM2, discarded events that had non-interacting beam particles. Lastly, the *Veto hodoscopes* rejected beam particles with unfamiliar trajectories.

Additional cuts were derived from the event topology. It was required that there is only one primary vertex within the target, where the incoming beam and outgoing particles' trajectories intersect. There

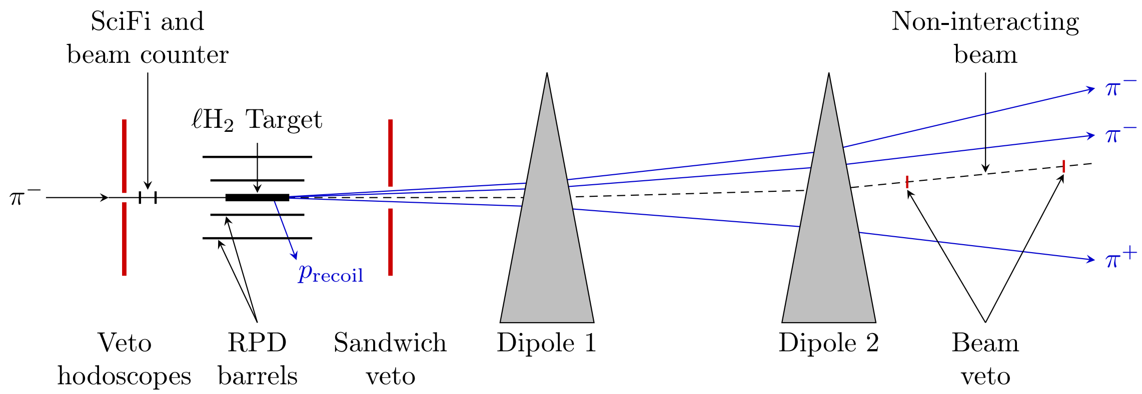

Figure 1.7: Trigger scheme of the DT0 Trigger. [5]

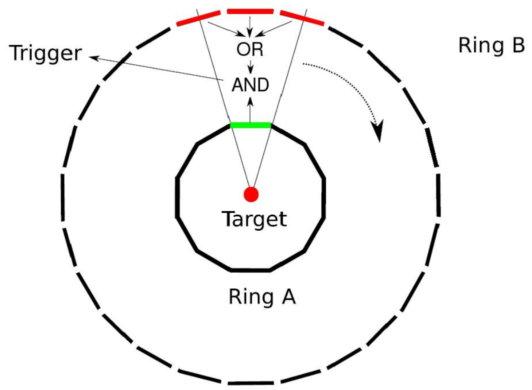

Figure 1.8: Schematic of the principle of the proton trigger. The outbound proton has to hit a segment of the inner ring (green) and one of the three adjacent segments of the outer ring (red).[6]

should be exactly three outgoing charged particles. These particles may only have a net charge of −1. To prohibit additional beam interactions outside of the event time window (a phenomenon called *pile up*), a cut was made around the trigger time (time a beam particle arrived at the beam telescope).

The next cut demanded momentum conservation. Since in the laboratory system the recoil proton and the X^- were released back-to-back, a cut was made on the relative angle $\Delta\phi$ between the two. The angle should be $\Delta\Phi = 180°$, but was limited by the resolution of the RPD. The next step was to require energy conservation. Since the energy is not measured for single beam particles, the beam energy has to be calculated from energy and momentum of the final-state particles. All events that lay outside of 2σ of the peak of the nominal beam energy were eliminated.

Next up was the suppression of central-production events (see section 1.1.5). In central production events, most of the time a fast final-state π^- and a slower $\pi^+\pi^-$ pair from the resonance decay was encountered. The kinematic variable to differentiate this process from diffractive dissociation was the rapidity y of a pion:

$$y = \frac{1}{2} \ln \frac{E + p_z}{E - p_z} \tag{1.13}$$

where E was the energy of the pion and p_z the momentum in beam direction. Another important variable was *Feynman's x*, which in the center-of-mass frame was:

$$x_F \approx \frac{2p_{z,\mathrm{com}}}{\sqrt{s}} \tag{1.14}$$

To eliminate a large part of central production events, events with a rapidity gap between the fast π^- and the $\pi^+\pi^-$ of $\Delta y > 4.5$ were removed, while the x_F of the fast pion had to be larger than 0.9.

The analysis is performed in the $m_{3\pi}$ range from 0.5 to 2.5 GeV/c^2 and for reduced four-momentum squared transfers t' between 0.1 and 1.0 (GeV/c)^2.

1.3 Structure and Goal of this Thesis

This thesis is based on diffractive-dissociation data of a 190 GeV/c π^- into the $\pi^-\pi^+\pi^-$ final state using a proton target. The data were recorded during the 2008 hadron run of the COMPASS experiment at CERN. The analysis method employed here is called *Partial Wave Analysis* (PWA) and is performed with the goal to disentangle the contributions of the different three-pion resonances to the data. To accomplish this, a physical model is constructed and fitted to the data. This model is comprised of a set of partial waves which describe the formation of different 3π intermediate states and their decay. The analysis procedure is explained in detail in the next chapter.

The PWA is inherently model dependent, meaning the results of the analysis may differ vastly depending on the employed set of partial waves. In previous analyses [3, 5], which are the starting point of this thesis, the model was selected by hand and a lot of time had to be invested to study the systematic effects of adding and removing model parameters (i.e. partial waves). The goal of this thesis is to perform a proof-of-concept study of an automatized model-selection procedure that returns a sensible model based on the given data, without introducing observer bias by hand-selecting the model. This novel procedure is introduced in chapter 3.

In Chapter 4, the results of the model-selection procedure performed on the COMPASS $\pi^-\pi^+\pi^-$ data will be presented. Since the scope of this thesis is limited to a proof-of-concept, only on subset of the existing COMPASS data is used. The extension of the analysis to the complete data set is straight forward. The last chapter will present the conclusions and an outlook.

CHAPTER 2

Partial-Wave Analysis Method

Partial-wave analysis (PWA) is an analysis method in particle physics that makes it possible to measure short-lived resonances and their properties (mass, width and quantum numbers) by using the observed kinematic distributions of the final-state particles, into which the resonances are decaying. Figure 1.3 shows the reaction

$$\pi^- + p \to \pi^-\pi^+\pi^- + p, \tag{2.1}$$

which is the main focus of this analysis. A negative beam pion interacts with a target proton via strong interaction, which results in the formation of a negatively charged, short-lived intermediate state X^-. This excited state quickly decays into a final state consisting of three charged pions $\pi^-\pi^+\pi^-$. Since the target proton stays intact the target vertex is neglected. This process is called diffractive dissociation. The main assumption of the PWA is that the intermediate state is dominated by resonances so that the production of the X^- is independent of their decay. Therefore, we can factorize the scattering amplitude into a production amplitude, which is the probability amplitude for the creation of X^-, and a decay amplitude, quantifying the dissociation of X^-. Extracting the production amplitudes will be the ultimate goal of the partial-wave analysis. For a specific decay channel, the kinematic distributions of the scattering amplitude depends on the center-of-mass energy s, the final-state invariant mass $m_{3\pi}$, the reduced squared four-momentum transfer t' and a set of additional kinematic variables τ.

At this point it is important to mention that the partial-wave decomposition, as it is performed in this thesis, is only the first part of a two-stage analysis. In this thesis, only the partial-wave decomposition, also called *mass-independent fit*, is performed. During this step, the production amplitudes are extracted in narrow bins of the final-state mass $m_{3\pi}$, but no assumptions about the 3π-resonance content are being made. To extract the resonances, one has to perform the second stage of the analysis, the *mass-dependent fit*, where the $m_{3\pi}$ dependence of the production amplitudes is fit by a resonance model. Further details on the partial-wave analysis technique can be found in [7], [5] and [3].

2.1 Parameterization of the Cross Section

We start by expressing the differential cross section for reaction 2.1 in terms of the set τ of the variables, that describe the kinematic distribution of the final-state particles:

$$\frac{d\sigma}{d\tau} = \sigma_0 \cdot \mathcal{I}(\tau) \tag{2.2}$$

Because the COMPASS detector is not optimized to detect absolute cross sections, the normalization factor σ_0 is unknown. It was mentioned in the chapter's introduction that the kinematic distributions, in addition to τ, depend on the center-of-mass energy s, squared four-momentum transfer t' and the final state invariant mass $m_{3\pi}$. Since COMPASS measures at fixed beam energy the center-of-mass energy is constant. In order to get rid of the latter two dependences the analysis is performed in narrow bins of both t' and $m_{3\pi}$. Within these bins the amplitudes are considered to be independent of $m_{3\pi}$ and t'. How the kinematic variables τ are chosen is subject of section 2.2.2. The intensity

$$\mathcal{I}(\tau) = \sum_{\epsilon=\pm1} \left| \sum_i \widetilde{\mathcal{T}}_i^\epsilon \sum_j \widetilde{\Psi}_{i,j}^\epsilon(\tau) \right|^2 + T_{\text{flat}}^2 \tag{2.3}$$

is proportional to the number of events measured by the experiment in the respective bin.

For convenience, the quantum numbers of the X^- are written in the *reflectivity basis*. In it, positive and negative values of the spin projection M are united to the absolute value of M. Additionally, a new quantum number, the *reflectivity* ε, is introduced, which can take on the values of $+1$ and -1. In the context of this thesis, it denotes the naturality [see equation (1.4)] of the exchange particle[1] between the target and the beam. A thorough explanation of the reflectivity basis is found in [5]. Therefore, the relevant quantum numbers to describe the state X^- are $J^{PC}\,M^\varepsilon$.

In the equation for the intensity, the index ϵ sums over the reflectivity, i sums over the quantum numbers $I^G J^{PC} M$ of the intermediate state X, while the index j indicates the different decay modes[2]. Since we have the same initial and final state for different intermediate states that are characterized by the i and j-indices, the sums over these indeces have to be coherent to include interference terms. The terms in the sum are the products of the production amplitudes $\widetilde{\mathcal{T}}_i^\epsilon$ and the decay amplitudes $\widetilde{\Psi}_{i,j}^\epsilon(\tau)$. The partial-wave analysis hinges on the fact that we can calculate the decay amplitudes so that the unknown production amplitudes can be estimated by a maximum likelihood fit of the $\mathcal{I}(\tau)$ to the observed τ distribution. How the decay amplitudes are calculated will be described in section 2.2. Finally, the term T_{flat}^2 is called the *flat wave*. It describes isotropic 3π background reactions, which is why it is added incoherently. In the further text, the t' dependence will be omitted to improve readability.

[1] In this reaction and energy range, pomeron exchange is dominant.
[2] As we will see in section 2.2.1, the intermediate state X does not decay directly into three pions, but rather via a single pion and a two-pion resonance. This resonance then decays into two more pions resulting in the three pion final state.

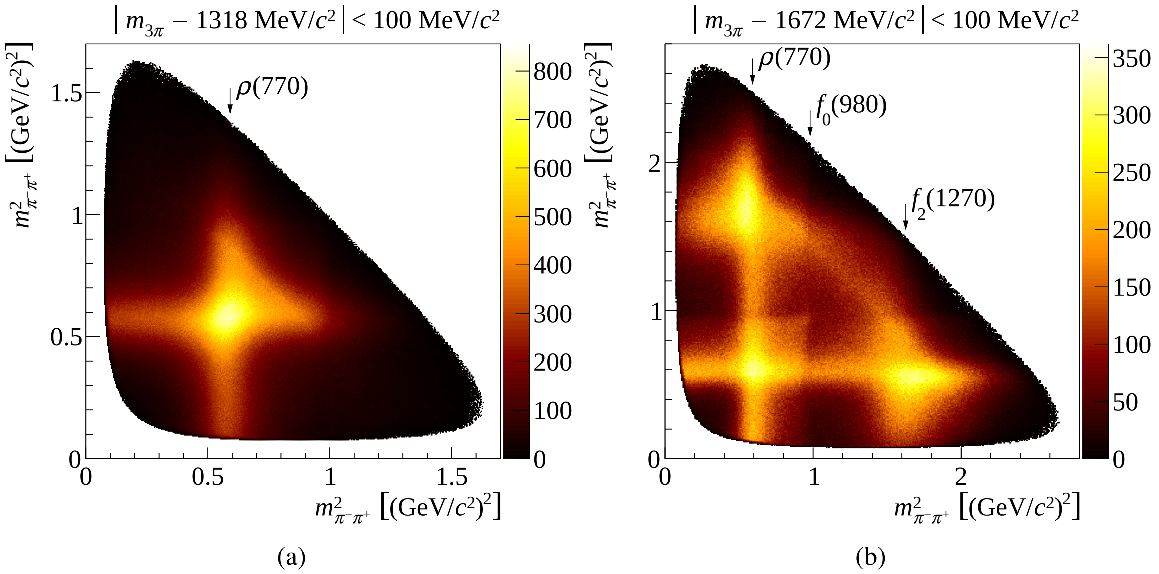

Figure 2.1: Dalitz plots of the 3π mass regions close to resonances (a) $a_1(1260)/a_2(1320)$ and (b) $\pi_2(1670)$. [5]

2.2 Decay Amplitudes

We now turn to the calculation of the decay amplitudes Ψ, which describe the decay of the intermediate state X into the 3π final state and are calculated using the isobar model.

2.2.1 The Isobar Model

Figure 2.1 shows Dalitz plots of two 3π mass ranges around $m_{3\pi} = 1318\,\mathrm{MeV}/c^2$ and $1672\,\mathrm{MeV}/c^2$. The figure illustrates, that the decay of X^- into three pions is dominated by $\pi^+\pi^-$ intermediate states, like e.g. the $\rho(770)$. The second plot shows the contribution of several two-pion resonances. Consequently, we can split up the three-body decay into two subsequent two-body decays. This approximation is called the isobar model, the intermediate two-pion resonance is called the isobar ξ. The model change can be seen by comparing figure 2.2 and figure 1.3.

Before we can calculate the decay amplitudes, we have to define the reference frames for the two two-body decays in order to choose the kinematic variables τ. Figure 2.3 shows the relevant reference frames for the decay. We start with the reference frame for the decay of the X^- intermediate state, which is the so-called *Gottfried-Jackson frame* (GF). It is a the rest frame of X^- with the beam axis serving as the z-axis z_{GJ}. The y-axis y_{GJ} is the normal to the plane spanned by the momenta of beam and recoil particle ($y_{\mathrm{GJ}} \propto p_{\mathrm{beam}} \times p_{\mathrm{recoil}}$). Finally the x-axis x_{GJ} is chosen such that the Gottfried-Jackson frame right-handed. Because it is a rest frame of X^-, the reaction products, π^- and the isobar ξ, are emitted in opposite directions, thus the decay can be described by two angles: the polar angle ϑ_{GJ} and the azimuthal Treiman-Yang angle ϕ_{TY} of the isobar.

This brings us to the system used to describe the isobar decay. For this process the helicity frame

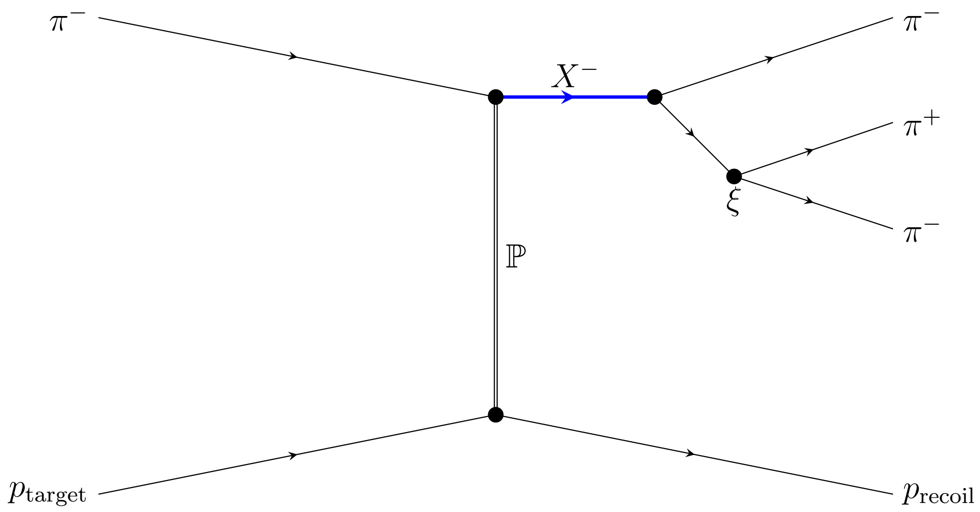

Figure 2.2: Diffractive dissociation in the picture of the isobar model. The intermediate state X^- decays into a bachelor π^- and a 2π resonance ξ called isobar. This isobar subsequently decays into π^+ and π^-.

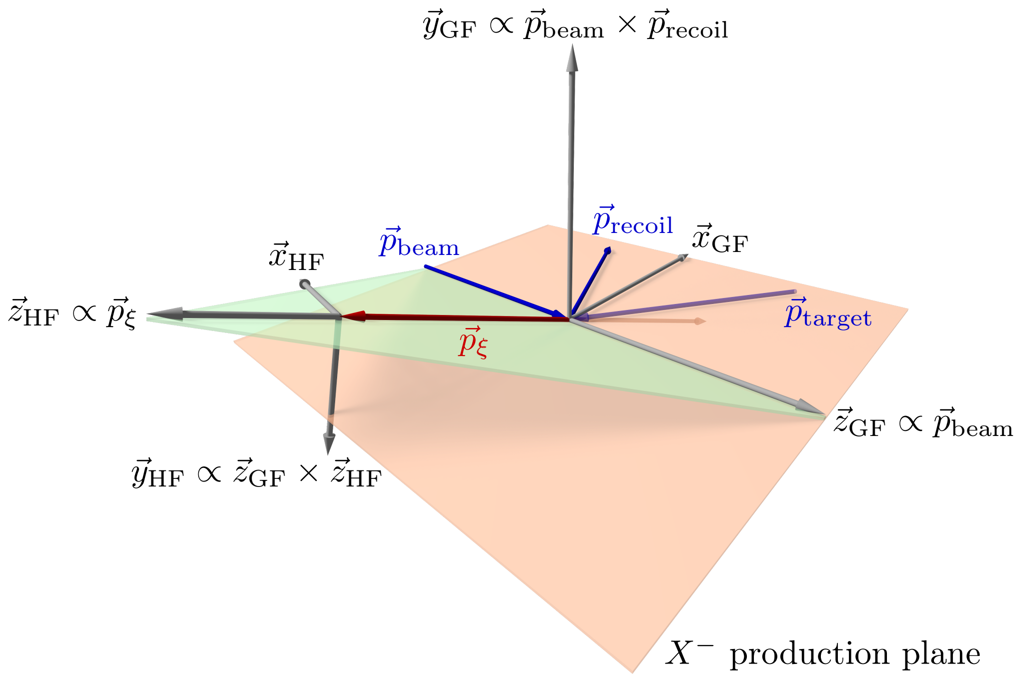

Figure 2.3: The definition of the axes of the Gottfried-Jackson (GJ) and helicity frame (HF). [7]

(HF) is used. In this reference frame the isobar is at rest. The z-axis z_{HF} is defined by the momentum vector of the isobar in the Gottfried-Jackson frame while the y-axis y_{HF} is orthogonal to the plane spanned by z_{GF} and z_{HF}. Similarly to the Gottfried-Jackson frame, the x-axis x_{HF} is defined by the right-handedness of the system. Again the decay particles – in this case two charged pions – are emitted in opposite directions and the decay is described by a polar angle ϑ_{HF} and an azimuthal angle ϕ_{HF} of the π^-.

At this point, we can define the kinematic variables τ:

$$\tau \equiv (\vartheta_{\mathrm{GJ}}, \phi_{\mathrm{TY}}, m_{\xi}, \vartheta_{\mathrm{HF}}, \phi_{\mathrm{HF}}) \tag{2.4}$$

The polar and azimuthal angles of the two reference frames and additionally the invariant mass of the isobar uniquely describe the four-vectors of the final-state pions for given $m_{3\pi}$ and t'. These five variables will be the τ we use for the partial-wave analysis of the 3π system.

2.2.2 Parameterization of the Decay Amplitudes

We begin by writing down the decay amplitude $\mathcal{A}^{\mathcal{P}}_{1,2}$ for the decay of a parent particle $\mathcal{P}$ with mass $m_{\mathcal{P}}$, spin $J_{\mathcal{P}}$ and spin projection $M_{\mathcal{P}}$ into two daughter particles 1 and 2 with masses $m_{1,2}$, spins $J_{1,2}$ and helicities $\lambda_{1,2}$:

$$\mathcal{A}^{\mathcal{P}}_{1,2}(\phi, \vartheta, m_{\mathcal{P}}, m_1, m_2) = \sum_{\lambda_1,\lambda_2} D^{J_{\mathcal{P}}}_{M_{\mathcal{P}}\,\lambda}(\phi, \vartheta, 0)\; f^{\mathcal{P}}_{1,2}(m_{\mathcal{P}}, m_1, m_2)\, \mathcal{A}_1 \mathcal{A}_2\;;\;\lambda = \lambda_2 - \lambda_1 \tag{2.5}$$

The decay amplitude is factorized into two parts – the angular dependence $D^{J_{\mathcal{P}}}_{M_{\mathcal{P}}\,\lambda}$ and the dynamic part $f^{\mathcal{P}}_{1,2}$. The amplitudes of the daughter particles $\mathcal{A}_{1,2}$ are 1, if it is stable.

The angular part is described by the Wigner D-function $D^{J}_{M\,\lambda}$ which depends on the polar coordinates ϑ and ϕ. The third angle of the function is set to 0, because the decay momenta of the daughters form a line, thus removing a degree of freedom. If the parent particle is an isobar, $M_{\mathcal{P}}$ is replaced by the helicity of the isobar $\lambda_{\mathcal{P}}$.

The dynamic part

$$f^{\mathcal{P}}_{1,2}(m_{\mathcal{P}}, m_1, m_2) = \underbrace{\sqrt{2L+1}}_{\text{normalization}}\; \underbrace{(J_1\,\lambda_1\;J_2\,{-\lambda_2}\,|\,S\;\lambda)\,(L\,0\;S\;\lambda\,|\,J_{\mathcal{P}}\,\lambda)}_{\text{Clebsch-Gordan coefficients}}\; \underbrace{\alpha^{\mathcal{P}}_{1,2}\,F_L(m_{\mathcal{P}}, m_1, m_2)\,\Delta^{\mathcal{P}}_{1,2}(m_{\mathcal{P}}, m_1, m_2)}_{\text{dynamics}}, \tag{2.6}$$

with the angular momentum L between the two daughter particles, consists of a normalization term, the Clebsch-Gordan coefficients for the spin-spin and spin-orbit coupling and dynamics. In the latter, the F_L are the Blatt-Weisskopf angular momentum barrier factors [8] in the parameterization by von Hippel and Quigg [9] while $\Delta^{\mathcal{P}}_{1,2}$ is the mass dependence of the amplitude. The complex-valued constant $\alpha^{\mathcal{P}}_{1,2}$ describes the coupling of $\mathcal{P}$ to 1 and 2 and is generally unknown.

The total decay amplitude results from a recursive application of equation (2.5):

$$\psi_{i,j}(\underbrace{\vartheta_{GJ}, \phi_{TY}, m_\xi, \vartheta_{HF}, \phi_{HF}}_{\tau}; m_{3\pi}) = \mathcal{A}^X_{\xi,\pi}(\phi_{TY}, \vartheta_{GJ}, m_{3\pi}, m_\xi; m_\pi)\, \mathcal{A}^\xi_{\pi,\pi}(\vartheta_{HF}, \phi_{HF}, m_\xi; m_\pi, m_\pi) \quad (2.7)$$

Applying equation (2.5) to the decay of the X^-, we use the fact that one decay particle is a final-state pion with helicity $\lambda = 0$, which means that the sum in equation (2.5) runs over the possible helicities of the isobar. In the dynamic part, the mass dependency $\Delta^X_{\xi,\pi}$ is set to unity, because the narrow bins in $m_{3\pi}$ allow us to assume that the amplitude is constant over an $m_{3\pi}$ bin. This $m_{3\pi}$ dependence is actually the result of the analysis, if we combine the results of multiple $m_{3\pi}$ bins. The resulting amplitude for $X^- \to \pi^- \xi^0$ and the associated dynamic part look as follows:

$$\mathcal{A}^X_{\xi,\pi}(\vartheta_{GJ}, \phi_{TY}, m_{3\pi}, m_\xi) = \sum_\lambda D^J_{M_X\,\lambda}(\phi_{TY}, \vartheta_{GJ}, 0)\, f^J_{\lambda 0}(m_{3\pi}, m_\xi, m_\pi) \quad (2.8)$$

$$f^J_{\lambda 0}(m_{3\pi}, m_\xi, m_\pi) = \sqrt{2L+1}\,(L\;0\;J_\xi\;\lambda \mid J\;\lambda)\,\alpha_X\,F_L(m_{3\pi}, m_\xi, m_\pi) \quad (2.9)$$

Moving on to the decay of the isobar, we now have two pions with helicity $\lambda = 0$ in the final state. Hence the sum in equation (2.5) disappears. Similarly the Clebsch-Gordan coefficients result to 1 in the dynamic part. The orbital angular momentum L is equal to the spin J_ξ of the isobar. The shape of the isobar mass dependence $\Delta^\xi_{\pi,\pi}$ is a property of the isobar and will be discussed in more detail in section 2.2.3. The resulting amplitude is

$$\mathcal{A}^\xi_{\pi,\pi}(\vartheta_{HF}, \phi_{HF}, m_\xi) = D^{J_\xi}_{\lambda 0}(\phi_{HF}, \vartheta_{HF}, 0)\, f^{J_\xi}_{\pi\pi}(m_\xi, m_\pi, m_\pi) \quad (2.10)$$

with the dynamic part

$$f^{J_\xi}_{\pi\pi}(m_\xi, m_\pi) = \sqrt{2J_\xi + 1}\,\alpha_\xi F_{J_\xi}(m_\xi; m_\pi, m_\pi)\,\Delta_\xi(m_\xi; m_\pi, m_\pi). \quad (2.11)$$

One last aspect we have to consider when calculating the decay amplitudes is the fact that pions are bosons and are thus indistinguishable if they carry the same charge. The decay amplitude has to be symmetric under permutations of indistinguishable pions. Since we have two negatively charged pions, to achieve the correct Bose symmetry, we have to sum up two amplitude terms, where we exchange the two π^- in the final state to account for self interference:

$$\Psi_{i,j}(\tau_{13}, \tau_{23}, m_{3\pi}) = \frac{1}{\sqrt{2}}\Big(\psi_{i,j}(\tau_{13}; m_{3\pi}) + \psi_{i,j}(\tau_{23}; m_{3\pi})\Big) \quad (2.12)$$

Here, τ_{13} and τ_{23} are the kinematic variables of the two permutations of the $\pi^+\pi^-$ system of the $\pi_1^-\pi_2^-\pi_3^+$ final state.

2.2.3 Isobar Parameterization

The previous section showed how to calculate the decay amplitudes for different X^-. One thing that was omitted was the mass dependence Δ^ξ of the isobar decay [see equation (2.11)]. Because $\Delta^\xi_{\pi\pi}$ is characteristic for each isobar we first have to determine which isobars are included in our analysis. Since there are no known $\pi^-\pi^-$ resonances, only isobars decaying to $\pi^-\pi^+$ are considered.

In this analysis, the isobars $[\pi\pi]_S$, $\rho(770)$, $f_0(980)$, $f_2(1270)$, $f_0(1500)$ and $\rho_3(1690)$ are included. The choice was motivated by the features of the Dalitz plots (see figure 2.1), the $\pi^+\pi^-$ mass spectrum (see figure 2.5) and the findings of previous analyses [3, 5].

We now have to parameterize the mass dependence of these isobars. For most isobars, a relativistic Breit-Wigner amplitude [10]

$$\Delta_{BW}(m; m_0, \Gamma_0) = \frac{m_0\,\Gamma_0}{m_0^2 - m^2 - i\,m_0\,\Gamma(m)} \tag{2.13}$$

is used, where m_0 and Γ_0 are the mass and width of the isobar, respectively. The formula for the mass-dependent width $\Gamma(m)$ varies for the isobars. The simplest case is the $f_0(1500)$, where it is constant:

$$\Gamma(m) = \Gamma_0 \tag{2.14}$$

For the $f_2(1270)$ the following Γ mass dependence is used:

$$\Gamma(m) = \Gamma_0 \frac{m_0}{m} \frac{q(m)}{q_0} \frac{F_\ell^2(q)}{F_\ell^2(q_0)} \tag{2.15}$$

In this equation, $q(m)$ is the momentum of the outgoing pions in the helicity frame (see section 2.2.1), while q_0 is the breakup momentum at the nominal mass m_0 of the resonance. The F_ℓ terms are (see section 2.2.2) the Blatt-Weisskopf angular momentum barrier factors[8].

For the $\rho(770)$ and the $\rho_3(1690)$ we use a slight variation of equation (2.15):

$$\Gamma(m) = \Gamma_0 \frac{q(m)}{q_0} \frac{F_\ell^2(q)}{F_\ell^2(q_0)} \tag{2.16}$$

This leaves the $[\pi\pi]_S$ and $f_0(980)$. They are both scalar isobars ($J^{PC} = 0^{++}$) and have overlapping intensity. The narrow $f_0(980)$ cannot be described by a Breit-Wigner amplitude, because the resonance is close to the $K\overline{K}$ threshold. As a result we use the Flatté parameterization [11]

$$\Delta_{\text{Flatté}}(m; m_0, g_{\pi\pi}, g_{K\overline{K}}) = \frac{1}{m_0^2 - m^2 - i\left(\phi_2^{\pi\pi}\,g_{\pi\pi} + \phi_2^{K\overline{K}}\,g_{K\overline{K}}\right)}, \tag{2.17}$$

which takes into account the additional coupling to the $K\overline{K}$ decay channel. In this equation the g terms are the couplings for $\pi\pi$ and $K\overline{K}$ respectively and $\phi_2 = 2q/m$ the two-body phase space for the respective decay channel with the break-up momentum q of the two daughter particles. The values for these parameters, including the mass m_0, were determined by the BES experiment [12].

Finally the $[\pi\pi]_S$ isobar is described with a modified parameterization based on the "M-solution" in [13]. The modification removes the $f_0(980)$ component of the amplitude [5], because we treat the $f_0(980)$ as a separate isobar. Figure 2.4 depicts the amplitude of the $[\pi\pi]_S$ isobar as it is used in this analysis.

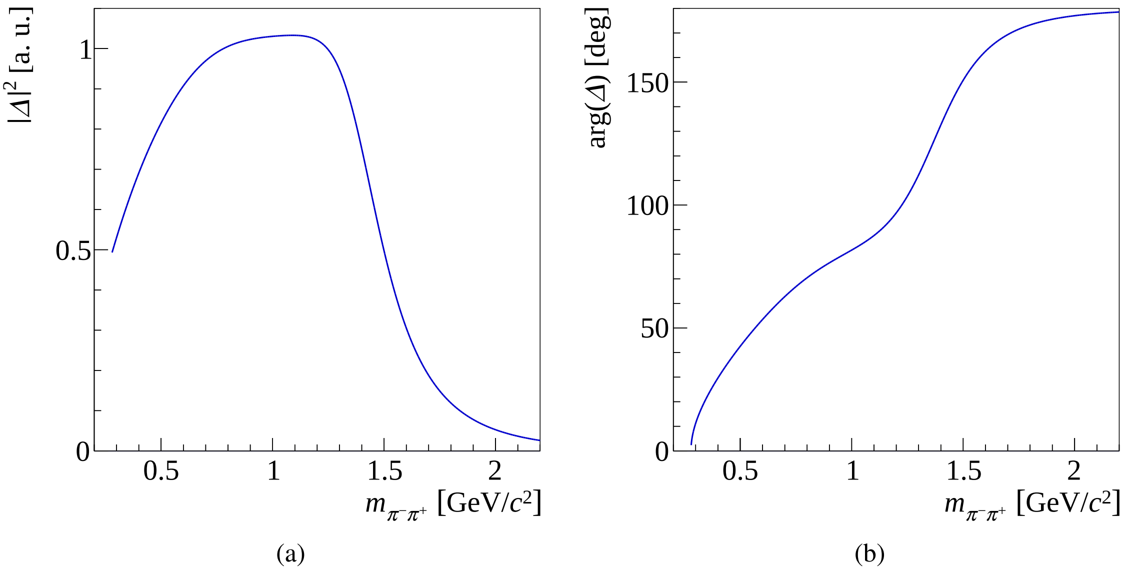

Figure 2.4: (a) Intensity and (b) phase of the $[\pi\pi]_S$ isobar as used in this analysis. [5]

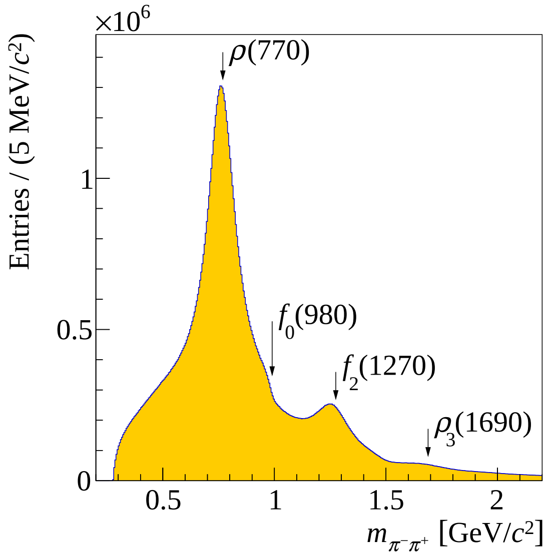

Figure 2.5: The distribution of the invariant mass of the $\pi^+\pi^-$ subsystem. [5]

Isobar	Parameterization	Parameters
$[\pi\pi]_S$	see [5]	
$\rho(770)$	Relativistic Breit-Wigner with eq. 2.16	$m_0 = 770\,\mathrm{MeV}/c^2$ $\Gamma_0 = 161\,\mathrm{MeV}/c^2$
$f_0(980)$	Flatté parameterization[12]	$m_0 = 965\,\mathrm{MeV}/c^2$ $g_{\pi\pi} = 0.165\,(\mathrm{GeV}/c^2)^2$ $g_{\pi\pi}/g_{K\overline{K}} = 4.21$
$f_2(1270)$	Relativistic Breit-Wigner with eq. 2.15	$m_0 = 1275\,\mathrm{MeV}/c^2$ $\Gamma_0 = 185\,\mathrm{MeV}/c^2$
$f_0(1500)$	Relativistic Breit-Wigner with eq. 2.14	$m_0 = 1507\,\mathrm{MeV}/c^2$ $\Gamma_0 = 109\,\mathrm{MeV}/c^2$
$\rho_3(1690)$	Relativistic Breit-Wigner with eq. 2.16	$m_0 = 1688\,\mathrm{MeV}/c^2$ $\Gamma_0 = 161\,\mathrm{MeV}/c^2$

Table 2.2: Overview of the isobar parameterizations.

The parameterizations of all isobars, including the values of the parameters used, are summarized in table 2.2.

2.3 Normalization

Because the coupling constants α_X and α_ξ appearing in equations (2.9) and (2.11) are usually unknown, they can be absorbed into the production amplitudes by the following redefenition:

$$\overline{\Psi}^{\epsilon}_{i,j}(\tau) \equiv \frac{\widetilde{\Psi}^{\epsilon}_{i,j}(\tau)}{\alpha_X\,\alpha_\xi} \tag{2.18}$$

$$\overline{\mathcal{T}}^{\epsilon}_{i,j} \equiv \widetilde{\mathcal{T}}^{\epsilon}_{i}\,\alpha_X\,\alpha_\xi \tag{2.19}$$

Since with this change the production amplitudes will not only describe the production of the intermediate state X, but also its coupling to a specific decay channel, we will call the $\overline{\mathcal{T}}$s transition amplitudes from this point on. We can now combine the indices i (quantum numbers of the intermediate state X) and j (X decay channel) into a single index α. Together with the reflectivity, the unique index α represents a partial wave:

$$\alpha = (i, j) \tag{2.20}$$

Finally, we normalize the decay amplitudes using phase-space integrals. This requires another set of substitions. For this we need to introduce the phase-space volume V_Ω and the phase-space integrals

$\mathcal{P}^{\epsilon}_{\alpha\beta}$:

$$\begin{aligned} V_{\Omega} &\equiv \int \mathrm{d}\phi_3(\tau) \\ \mathcal{P}^{\epsilon}_{\alpha\beta} &\equiv \int \mathrm{d}\phi_3(\tau)\, \overline{\Psi}^{\epsilon}_{\alpha}(\tau)\, \overline{\Psi}^{\epsilon}_{\beta}(\tau), \end{aligned} \tag{2.21}$$

where $\mathrm{d}\phi_3(\tau)$ is the differential three-body phase-space element. This forms the following normalization substitutions:

$$\begin{aligned} \Psi^{\epsilon}_{\alpha}(\tau) &\equiv \frac{\overline{\Psi}^{\epsilon}_{\alpha}(\tau)\ \sqrt{V_{\Omega}}}{\sqrt{\mathcal{P}^{\epsilon}_{\alpha\alpha}}} \\ T^{\epsilon}_{\alpha} &\equiv \overline{\mathcal{T}}^{\epsilon}_{\alpha}\ \sqrt{\mathcal{P}^{\epsilon}_{\alpha\alpha}} \\ T_{\text{flat}} &\equiv \mathcal{T}_{\text{flat}}\ \sqrt{V_{\Omega}} \end{aligned} \tag{2.22}$$

This ensures that the partial-wave intensities $\left|T^{\epsilon}_{\alpha}\right|^2$ are equal to the number of events a detector with a perfect acceptance would measure. After these substitutions the intensity reads:

$$\mathcal{I}(\tau) = \sum_{\epsilon=\pm 1} \left| \sum_{\alpha} \frac{T^{\epsilon}_{\alpha}\ \Psi^{\epsilon}_{\alpha}(\tau)}{\sqrt{V_{\Omega}}} \right|^2 + \frac{T^2_{\text{flat}}}{V_{\Omega}} \tag{2.23}$$

2.4 Extended Log-Likelihood Function

With expression 2.23 for the intensity, the probability to observe an event $\mathcal{E}$ with the kinematic coordinates $\tau_{\mathcal{E}}$ in all measured events $\mathbb{E}$ can be written as:

$$P(\mathcal{E}) = \frac{\mathcal{I}(\tau_{\mathcal{E}})}{\int d\phi_3(\tau)\mathcal{I}(\tau)\eta(\tau)}; \mathcal{E} \in \mathbb{E}, \tag{2.24}$$

The expression in the denominator is the integral over the whole available kinematic phase space of the decay, with $\eta(\tau)$ being the acceptance of the detector setup.

The next step is to use the probability in equation (2.24) to formulate an extended likelihood function

$$\mathcal{L}(T; \mathbb{E}) = \frac{e^{-\overline{N}}\overline{N}^N}{N!} \prod_{n=1}^{N} P(E_n) \tag{2.25}$$

where N is the number of measured events and $\overline{N}$ the number of expected measured events. The factor in front of the product is the Poisson probability to observe N events.

To ensure that the intensity has units of number of events we require that

$$\overline{N} = \int \mathrm{d}\phi_3(\tau)\, \mathcal{I}(\tau)\, \eta(\tau), \tag{2.26}$$

This term also appears as the denominator in equation (2.24). Inserting equation (2.23) into equation (2.26) yields

$$\begin{aligned}
\overline{N} &= \int d\phi_3(\tau) \left(\sum_{\epsilon=\pm1} \left| \sum_{\alpha} \frac{T_\alpha^\epsilon \, \Psi_\alpha^\epsilon(\tau)}{\sqrt{V_\Omega}} \right|^2 + \frac{T_{flat}^2}{V_\Omega} \right) \eta(\tau) \\
&= \int d\phi_3(\tau) \left(\sum_{\epsilon=\pm1} \sum_{\alpha,\beta} \frac{1}{V_\Omega} T_\alpha^\epsilon \, T_\beta^{\epsilon*} \, \Psi_\alpha^\epsilon(\tau) \, \Psi_\beta^{\epsilon*}(\tau) + \frac{T_{flat}^2}{V_\Omega} \right) \eta(\tau) \\
&= \sum_{\epsilon=\pm1} \sum_{\alpha,\beta} T_\alpha^\epsilon \, T_\beta^{\epsilon*} \underbrace{\frac{\int d\phi_3(\tau) \, \eta(\tau) \, \Psi_\alpha^\epsilon(\tau) \, \Psi_\beta^{\epsilon*}(\tau)}{V_\Omega}}_{\equiv \mathcal{N}_{\alpha\beta}^\epsilon} + T_{flat}^2 \underbrace{\frac{\int d\phi_3(\tau) \, \eta(\tau)}{V_\Omega}}_{\equiv \mathcal{A}}
\end{aligned} \tag{2.27}$$

with the integral matrix $\mathcal{N}_{\alpha\beta}^\epsilon$ and the total acceptance $\mathcal{A}$.

Using equation (2.27) the likelihood can be simplified to

$$\mathcal{L}(T; \mathbb{E}) = \frac{e^{-\overline{N}}}{N!} \prod_{n=1}^{N} \mathcal{I}(\tau_n). \tag{2.28}$$

For reasons of numerical stability, we will use the logarithm of the likelihood:

$$\ln \mathcal{L}(\mathcal{T}; \mathbb{E}) = \sum_{n=1}^{N} \ln \mathcal{I}(\tau_n) - \overline{N} \tag{2.29}$$

In the above expression, the term $-\ln N!$ was dropped because it is constant with respect to the transition amplitudes T and therefore does not change the shape of the likelihood. Inserting equation (2.27) into equation (2.29) results in:

$$\begin{aligned}
\ln \mathcal{L}(T; \mathbb{E}) = \sum_{n=1}^{N} \ln \left(\sum_{\epsilon=\pm1} \left| \sum_{\alpha} T_\alpha^\epsilon \, \Psi_\alpha^\epsilon(\tau_n) \right|^2 + T_{\text{flat}}^2 \right) - N \ln(V_\Omega) \\
- \sum_{\epsilon=\pm1} \sum_{\alpha,\beta} T_\alpha^\epsilon \, T_\beta^{\epsilon*} \, \mathcal{N}_{\alpha\beta}^\epsilon - T_{\text{flat}}^2 \, \mathcal{A}
\end{aligned} \tag{2.30}$$

Again, we can omit the $N \ln(V_\Omega)$-term, because it does not depend on the transition amplitudes and thus does not move the maximum of the likelihood function. The final likelihood function reads as follows:

$$\ln \mathcal{L}(T; \mathbb{E}) = \sum_{n=1}^{N} \ln \left(\sum_{\epsilon=\pm1} \left| \sum_{\alpha} T_\alpha^\epsilon \, \Psi_\alpha^\epsilon(\tau_n) \right|^2 + T_{\text{flat}}^2 \right) - \sum_{\epsilon=\pm1} \sum_{\alpha,\beta} T_\alpha^\epsilon \, T_\beta^{\epsilon*} \, \mathcal{N}_{\alpha\beta}^\epsilon - T_{\text{flat}}^2 \, \mathcal{A} \tag{2.31}$$

In the partial-wave decomposition the likelihood function is maximized with respect to the transition amplitudes. This corresponds to a fit of equation (2.23) to the measured τ distribution. The maximum-likelihood transition amplitudes are then used in a second analysis step to extract their resonance parameters [14, 15], which, however, is not within the scope of this thesis.

2.5 Uncertainties

An important part of every analysis is the estimation of the uncertainties. The systematic uncertainties of a partial-wave analysis are unfortunately hard to gauge, but one can at least estimate the statistical uncertainty of the resulting transition amplitudes.

In previous analyses, the covariance matrix was calculated numerically. However, this is computationally expensive. Since the analysis performed in this thesis uses many more free parameters than before, the computing time for the error calculation would rise to unacceptable levels. The solution is to calculate covariance matrix analytically. This has the additional advantage that the uncertainties are calculated exactly, instead of being estimated numerically.

In this thesis, statistical uncertainties are calculated using the first-order Gaussian error propagation which uses the covariance matrix of the fit parameters of the log-likelihood function [see equation (2.31)]. The covariance matrix is calculated by inverting the Hessian matrix H of the log-likelihood function, which is a square matrix of the second partial derivatives of the log-likelihood function with respect to the fit parameters:

$$\mathrm{Cov} = H^{-1} = \begin{pmatrix} \frac{\partial \ln \mathcal{L}}{\partial p_1 \, \partial p_1} & \cdots & \frac{\partial \ln \mathcal{L}}{\partial p_1 \, \partial p_{N_p}} \\ \vdots & \ddots & \vdots \\ \frac{\partial \ln \mathcal{L}}{\partial p_{N_p} \, \partial p_1} & \cdots & \frac{\partial \ln \mathcal{L}}{\partial p_{N_p} \, \partial p_{N_p}} \end{pmatrix}^{-1} \tag{2.32}$$

The variables p_i represent the N_p free parameters of the likelihood function, which are the real and imaginary parts of the transition amplitudes. The uncertainty in each parameter is defined by the square root of the respective value on the diagonal of the covariance matrix. It is important to note, that equation (2.32) is only valid if the uncertainties are Gaussian.

2.5.1 Analytical Calculation of the Hessian Matrix

The first step in deriving the Hessian matrix is, of course, to write down the gradient of the log-likelihood function. This is complicated by the fact that the free parameters, the transition amplitudes T, are complex numbers. It is simpler to regard the real and imaginary parts of the amplitudes as independent free parameters and to take the derivative of the function with respect to them. It can be shown, that the gradient of the log-likelihood function with repect to the the real and imaginary parts of the transition amplitude

$$T_\alpha^\epsilon = x_\alpha^\epsilon + \imath y_\alpha^\epsilon \tag{2.33}$$

is

$$\frac{\partial \ln \mathcal{L}}{\partial x_\alpha^\varepsilon} = \sum_{i=1}^{N} \frac{2}{A_{D_i}} \sum_{\beta}^{N_{\text{waves}}^\varepsilon} \mathfrak{Re}\left[T_\beta^\varepsilon D_{\beta\alpha,i}^\varepsilon\right] - 2 \sum_{\beta}^{N_{\text{waves}}^\varepsilon} \mathfrak{Re}\left[T_\beta^\varepsilon \mathcal{N}_{\beta\alpha}^\varepsilon\right] \tag{2.34}$$

$$\frac{\partial \ln \mathcal{L}}{\partial y_\alpha^\varepsilon} = \sum_{i=1}^{N} \frac{2}{A_{D_i}} \sum_{\beta}^{N_{\text{waves}}^\varepsilon} \mathfrak{Im}\left[T_\beta^\varepsilon D_{\beta\alpha,i}^\varepsilon\right] - 2 \sum_{\beta}^{N_{\text{waves}}^\varepsilon} \mathfrak{Im}\left[T_\beta^\varepsilon \mathcal{N}_{\beta\alpha}^\varepsilon\right] \tag{2.35}$$

with

$$\begin{aligned} D_{\alpha\beta,i}^\varepsilon &= \Psi_\alpha^\varepsilon(\tau_i)\Psi_\beta^\varepsilon(\tau_i) \\ A_{D_i} &= \sum_{\epsilon=\pm1} \sum_{\alpha,\beta}^{N_{\text{waves}}^\varepsilon} T_\alpha^\varepsilon T_\beta^{\varepsilon*} D_{\alpha\beta,i}^\varepsilon + T_{\text{flat}}^2 D_{\text{flat}.i}. \end{aligned} \tag{2.36}$$

Therefore, the second derivative with respect to the real parts of the transition amplitudes is:

$$\begin{aligned} \frac{\partial^2 \ln \mathcal{L}}{\partial x_\alpha^\varepsilon \, \partial x_{\tilde{\alpha}}^{\tilde{\varepsilon}}} &= \frac{\partial}{\partial x_{\tilde{\alpha}}^{\tilde{\varepsilon}}} \left(\sum_{i=1}^{N} \frac{2}{A_{D_i}} \sum_{\beta}^{N_{\text{waves}}^\varepsilon} \mathfrak{Re}\left[T_\beta^\varepsilon D_{\beta\alpha,i}^\varepsilon\right] - 2 \sum_{\beta}^{N_{\text{waves}}^\varepsilon} \mathfrak{Re}\left[T_\beta^\varepsilon \mathcal{N}_{\beta\alpha}^\varepsilon\right] \right) \\ &= -\sum_{i=1}^{N} \frac{4}{A_{D_i}^2} \left(\sum_{\beta}^{N_{\text{waves}}^{\tilde{\varepsilon}}} \mathfrak{Re}\left[T_\beta^{\tilde{\varepsilon}} D_{\beta\tilde{\alpha},i}^{\tilde{\varepsilon}}\right] \right) \left(\sum_{\beta}^{N_{\text{waves}}^\varepsilon} \mathfrak{Re}\left[\mathcal{T}_\beta^\varepsilon D_{\beta\alpha,i}^\varepsilon\right] \right) - 2\delta_{\varepsilon\tilde{\varepsilon}} \left(\mathfrak{Re}\left[\mathcal{N}_{\tilde{\alpha}\alpha}^\varepsilon\right] - \sum_{i=1}^{N} \frac{\mathfrak{Re}\left[D_{\tilde{\alpha}\alpha,i}^\varepsilon\right]}{A_{D_i}} \right) \end{aligned} \tag{2.37}$$

The other permutations of the second derivatives have very similar terms, where only the $\mathfrak{Re}$ and $\mathfrak{Im}$ functions change and will not be written down explicitly. A thorough derivation of the Hessian matrix of the likelihood function is found in appendix D. With the second derivatives it is possible to write down the Hessian matrix. Inverting this matrix results in the covariance matrix for the log-likelihood function [see equation (2.32)].

In addition to the increased computation speed, which the analytic calculation of the covariance matrix brings, it enables the usage of maximizers that do not have the functionality to numerically calculate the covariance matrix. Therefore, it was possible to use a maximizer that is specialized for high-dimensional functions called the Low-storage BFGS algorithm [16, 17] instead of the previously used Minuit2 library, which reduced the computing time needed for fitting even further.

2.5.2 Comparison of Uncertainties from Analytically and Numerically Calculated Covariance Matrix

To verify that the analytic calculation is implemented correctly, a comparison study is performed, which also includes the newly implemented maximizer. The study compares fit results obtained with the Minuit2 library, which calculates the uncertainties numerically, with fit results using the BFGS algorithm, where the uncertainties are calculated analytically. In detail, 30 fit attempts are performed using the known and well-understood reference wave set (see section 3.1) in one mass bin (2000–2020 MeV/c^2) using both methods. In the end, the results with the largest found likelihood for

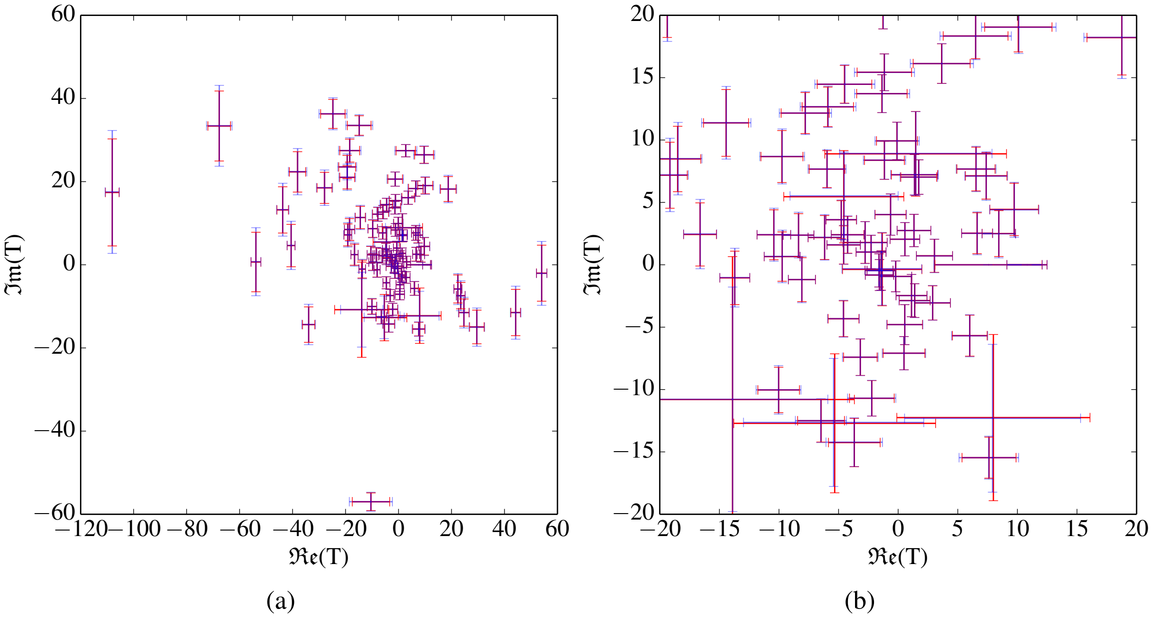

Figure 2.6: Comparison of the partial-wave amplitudes. The result in red is obtained using the Minuit2 library with a numerically calculated covariance matrix, while the blue color indicates the result of the BFGS algorithm with an analytically calculated covariance matrix. (a) shows all transition amplitudes, while (b) is a zoom into the region of smaller amplitudes.

each method are compared to another. As mentioned earlier, the numerically calculated covariance matrix is only an estimate of the real covariance matrix of the parameters of the log-likelihood function. Therefore, it cannot be expected that the analytic and numeric covariance matrix match exactly. This procedure, running several fit attempts and using only the best one, is used in real analyses as well, because the maximizer does not find the global maximum in every attempt.

Figure 2.6 presents the results of the study. The result of the Minuit2 library with the numerically calculated covariance matrix is red, whereas the BFGS result with an analytically calculated covariance matrix is blue. Each partial-wave amplitude is represented as a data point in the complex plane. The overview in figure 2.6a shows, that the results of the transition amplitudes are essentially equivalent. The red and blue data points are right on top of each other for every single transition amplitude with no visible discrepancy, even for smaller amplitudes (see figure 2.6b). Consequently, the two optimizers find the same likelihood maximum, which was the expected result.

A somewhat surprising result of this study is the deviation in the statistical uncertainties given by the two methods. Differences of the errors of up to 10% are observed. A possible explanation would be, that the numerically calculated covariance matrix is not precise. This would lead to statistical fluctuations around the real uncertainty values of the analytically calculated uncertainties. Closer inspection shows however, that the analytically calculated uncertainties are almost always larger than their numeric counterparts, which rules out this explanation. Repeating this study in multiple mass bins leads to similar results, but in some of the bins the numeric uncertainties are larger. This suggests, that the uncertainty estimates fo the two methods are somehow influenced differently by the data.

2.5.3 Study of the Likelihood Function Close to the Maximum

It is clear that the puzzling results of the uncertainty comparison in the previous section require further analysis. In this section, the region around the likelihood maximum is studied to reveal which of the two methods, numeric or analytic, better approximates the uncertainties of the parameters of the likelihood function.

Therefore, a Taylor expansion of the likelihood function around the likelihood maximum $\vec{m}$ is performed:

$$\ln \mathcal{L}(\vec{m} + \mathrm{d}\vec{m}) = \ln \mathcal{L}(\vec{m}) + \underbrace{\mathrm{d}\vec{m}^T \ \mathrm{grad}\left[\ln \mathcal{L}(\vec{x})\right]\Big|_{\vec{x}=\vec{m}}}_{=0} + \frac{1}{2}\,\mathrm{d}\vec{m}^T \ H\left[\ln \mathcal{L}(\vec{x})\right]\Big|_{\vec{x}=\vec{m}} \mathrm{d}\vec{m} \tag{2.38}$$

At the maximum, the second term vanishes. According to equation (2.32), the Hessian H of the log-likelihood function is the inverse of the covariance matrix. The eigenvectors $\vec{v}$ and eigenvalues λ of the covariance matrix are defined as follows:

$$\mathrm{Cov} \cdot \vec{v} = \lambda\, \vec{v} \tag{2.39}$$

With

$$\begin{aligned} \mathrm{Cov}^{-1} \cdot \mathrm{Cov} \cdot \vec{v} &= \lambda\, \mathrm{Cov}^{-1} \cdot \vec{v} \\ \mathrm{Cov}^{-1} \cdot \vec{v} &= \frac{1}{\lambda}\vec{v} \end{aligned} \tag{2.40}$$

it is obvious, that the Hessian and the covariance matrix have the same eigenvectors, but the eigenvalues of the Hessian are inverted.

We can now write down the Taylor expansion of the likelihood function at its maximum in the direction of a (normalized) eigenvector with the distance r to the maximum

$$\ln \mathcal{L}(\vec{m} + r\vec{v}) = \ln \mathcal{L}(\vec{m}) + \frac{r^2}{2\lambda}, \tag{2.41}$$

which describes a parabola with the curvature $\frac{1}{2\lambda}$. The standard deviation σ of a Gaussian likelihood function is defined at $r = \pm\sqrt{\lambda}$.

It is now possible to analyze the region around the maximum likelihood, by calculating the eigenvalues and eigenvectors for both, the analytic and numeric covariance matrix and overlaying the resulting parabolas on top of the actual likelihood function in a 1σ confidence interval. There are as many eigenvector/eigenvalue pairs as there are parameters of the likelihood function. Therefore, to analyze the many different plots systematically, the pairs are ordered according to increasing eigenvalues, which corresponds to increasing uncertainties.

Figure 2.7 shows 4 examples that demonstrate the behaviour of the likelihood function along the direction of the respective eigenvector. The numerically calculated Gaussian parabolas are drawn in blue, the analytic ones are red. The evaluated likelihood function values are indicated by the black data points. In figure 2.7a, the smallest eigenvalue, which corresponds to the smallest uncertainty is shown. The two approximations underestimate the error of the evaluated likelihood function. At intermediate eigenvalues (see figures 2.7b to 2.7d) the approximations are in good agreement with the evaluated likelihood function. With increasing uncertainties a trend is observed, that the Gaussian approximations deviate increasingly from the actual likelihood function (see figure 2.7e). Therefore, with increasing uncertainties, the likelihood function becomes increasingly non-Gaussian. For the largest eigenvalue in figure 2.7f, this becomes evident. The likelihood function has a trough-like shape, which the parabolas fail to reproduce. Only for this eigenvalue, a notable deviation between the numeric and analytic method is observed.

The impact on the uncertainties of the parameter values are large. Since the analysis described above was performed in the eigensystem of the covariance matrix, all uncertainties were uncorrelated. If we go back to the space of the real and imaginary parts of the transition amplitudes, the uncertainties are linear combinations of the uncertainties in the eigensystem. Therefore, the largest uncertainties in the eigensystem, which are non-Gaussian, have the largest effect on the parameter uncertainties. This also explains why the study in section 2.5.2 showed that either the numerically or analytically calculated uncertainties were larger for most parameters. Since the only notable difference between the two approximations is in the uncertainty for the largest eigenvalue, this deviation can be seen in many parameter uncertainties through linear combination.

Concluding, it is safe to say, that the Gaussian approximation for the uncertainties is not a good one. The same study in the $\pi^-\pi^0\pi^0$ final state confirmed the results. Therefore, this issue is relevant not only in the charged three-pion final state. Finding a better approximation for the uncertainties is not in the scope of this thesis and thus the Gaussian approximation will be used for the analysis in thesis. A possible solution would be to use Markov chain Monte Carlo (MCMC) methods to sample the likelihood function. This would provide the probability density function of the likelihood function in the form of a point cloud, which includes all information about the uncertainties and correlations of all parameters.

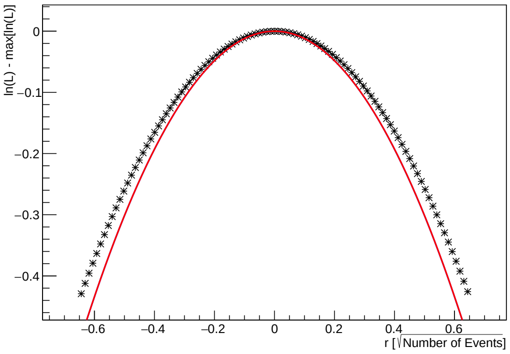

(a) Smallest (172$^{\text{th}}$ largest) eigenvalue

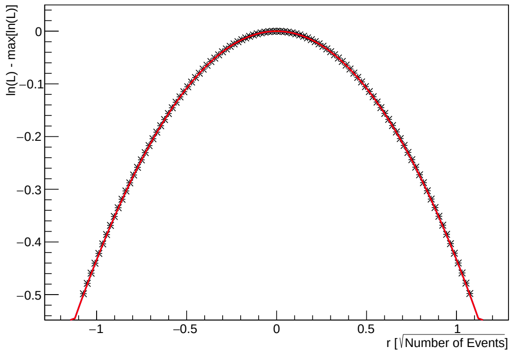

(b) 120$^{\text{th}}$ largest eigenvalue

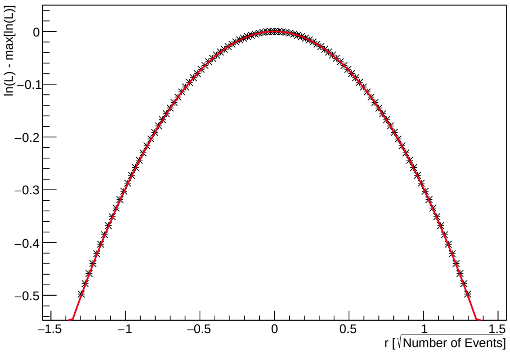

(c) 80$^{\text{th}}$ largest eigenvalue

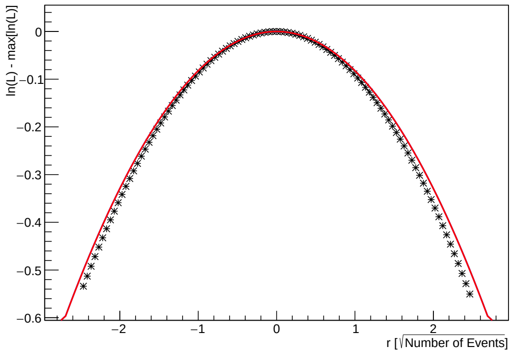

(d) 20$^{\text{th}}$ largest eigenvalue

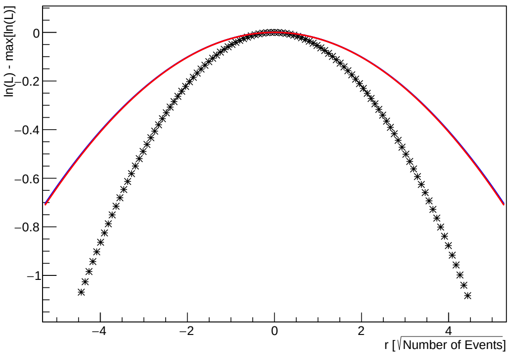

(e) 6$^{\text{th}}$ largest eigenvalue

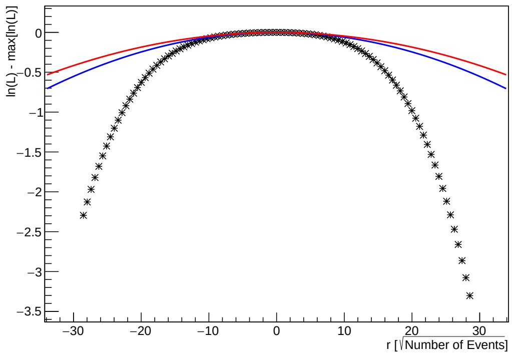

(f) largest eigenvalue

Figure 2.7: Comparison of the numeric (blue) and analytic (red) Gaussian parabolas with the values of the likelihood function (black) along the direction of the eigenvectors of the covariance matrix for increasing eigenvalues.

CHAPTER 3

Model Selection

The goal of model selection in general is to choose the model that best describes the data. This is not a trivial process, because there are typically many ways to describe the measured data and thus a large model space to choose from. The log-likelihood function used in this analysis [see equation (2.31)] includes theoretically infinite sums over the partial waves. In practice, the series of partial waves has to be truncated at some point. In this context, after maximizing the likelihood, a *model* is a collection of waves, also called *wave set*, that will describe the measured data with varying success. Therefore, the goal of model selection in this thesis is to find the wave set that best describes the data while keeping the number of free parameters to a minimum.

Until now, model selection in the three-pion channel was based on performing systematic studies that investigate changes in the maximum likelihood when waves are eliminated or added to the wave set. The inherent problem with this method is, that adding free parameters, which is basically what adding waves is, will always increase the likelihood. This may lead to a point where the model will describe statistical fluctuations of the data, which, of course, have no physical meaning. The conclusion is that the likelihood cannot be used as a quantity to determine the goodness-of-fit of a model. Another problem appears when we omit a significant wave from the wave set. Either the model will not describe parts of the data well or some of the data will be wrongfully attributed to other partial waves, which is a phenomenon called *model leakage*. The latter is considerably worse because it may easily result in wrong models. There are other effects, where waves missing from the wave set are compensated for by a combination of other waves. It is also observed that a certain subset of waves is important to describe the data, but individually they are not important.

The basis of the model-selection procedure used in this thesis is to first determine all the waves that could conceivably contribute to the measured data. This large set of waves will from now on be called the *wave pool*. Neglecting possible detector effects and assuming that the model in principle is able to describe the data, if we perform a partial-wave decomposition with the whole wave pool, no model leakage should occur. The only thing one has to worry about is the possibly too large number of free parameters. Therefore, to derive a smaller wave set that describes the data equally well, we have to eliminate those waves from the wave pool that are not essential to describe the data. The procedure described in this chapter is an elegant way to do just that, while avoiding the selection bias of the manual approach used in previous analyses.

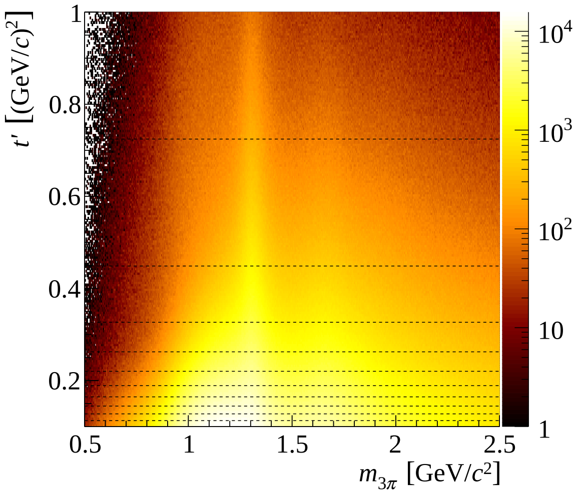

Figure 3.1: Correlation of $m_{3\pi}$ and t' in the analyzed final-state mass and reduced four-momentum transfer squared range. [5]

Bin	**Lower Boundary** [(GeV/c)^2]	**Upper Boundary** [(GeV/c)^2]
1	0.100	0.113
2	0.113	0.127
3	0.127	0.144
4	0.144	0.164
5	0.164	0.189
6	0.189	0.220
7	0.220	0.262
8	0.262	0.326
9	0.326	0.449
10	0.449	0.724
11	0.724	1.000

Table 3.1: Boundaries of the squared four-momentum transfer bins.

3.1 Reference Wave Set

Before explaining the model selection performed in this thesis, a model previously used in the three-pion channel [3, 5] is reviewed. It consists of 88 waves, of which 80 have positive and only 7 negative reflectivity. An incoherently added isotropic ("flat") wave completes the wave set. To stabilize the fit it was necessary to omit some waves in the low-mass region. They are included into the wave set only above certain $m_{3\pi}$ thresholds. This 88-wave model was derived by performing extensive systematic studies and will serve as a benchmark for the model selection throughout the thesis. From now on it will be referred to as the *reference wave set*. The complete wave set including thresholds is listed in appendix A.

3.1.1 Division in Narrow Bins of Final-State Mass and Reduced Four-Momentum Transfer Squared

As already mentioned in section 2.1, the analysis is performed in narrow bins of the invariant three-pion mass $m_{3\pi}$ and the squared four-momentum transfer t'. This is done to remove the dependence on these two variables in the transition amplitudes. Using narrow bins, we can assume $m_{3\pi}$ and t' to be constant over the range covered by the respective bin.

The analyzed mass range from 0.5 to 2.5 GeV/c^2 is divided into 100 bins with 20 MeV width. The t' bins are not equidistant. They are rather chosen such that each bin contains approximately the same number of events. The only exception is the t' range from 0.449 to 1.000 (GeV/c)^2. This range is too wide to satisfy the condition of an almost constant t'. Therefore it is split into two bins, resulting in 11 t' bins overall. Figure 3.1 shows the correlation of $m_{3\pi}$ and t' in the analyzed range with the t' bin boundary indicated by dashed horizontal lines. Table 3.1 shows the numeric values of the t' bin

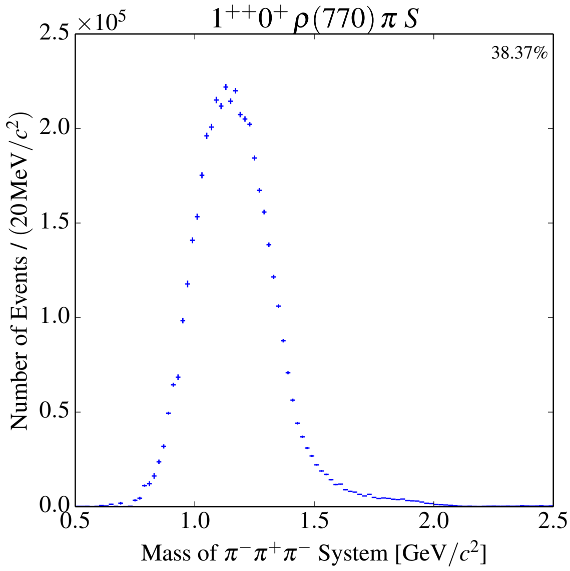

Figure 3.2: Intensity plot of the $1^{++}0^+\rho(770)\pi S$ wave, showing the $a_1(1260)$ resonance.

boundaries.

Because this thesis serves only as a proof of principle, only the lowest t' bin from 0.100 to 0.113 $(\mathrm{GeV}/c)^2$ is analyzed here. The methods and results are easily transferable to the remaining t' bins.

3.1.2 Fits with the Reference Wave Set

To get a sense for the expected outcome of the mass-independent fit in the three-pion channel, fit results with the reference wave set will be presented in this section. The data are taken from the 2008 COMPASS hadron run with the applied event selection outlined in 1.2.3.

The partial wave with the largest intensity, the $1^{++}0^+\rho(770)\pi S$ wave, is shown in figure 3.2. It contains the $a_1(1260)$ resonance. The notation of the wave names reads as follows: The first part defines the quantum numbers $J^{PC}\,M^\varepsilon$ of the X^-. The rest of the name is determined by the decay channel, starting with the isobar and followed by the bachelor pion (π). The last letter represents the orbital angular momentum between the isobar and the pion, where the letters S, P, D, etc. refer to the angular momenta $L = 0, 1, 2$, etc.

The graph in figure 3.2 shows the intensity of the wave over the analyzed mass range. The integrated intensity over the whole mass range divided by the total number of events will from now on be called the *relative intensity* of a wave and is written in the corner of the graph as an indicator for the significance of a wave.

The length of the vertical lines in figure 3.2 represent the statistical errors while the length of the horizontal lines indicate the $m_{3\pi}$ bin width. Since the $1^{++}0^+\rho(770)\pi S$ wave is stable with many events, the statistical errors are very small.

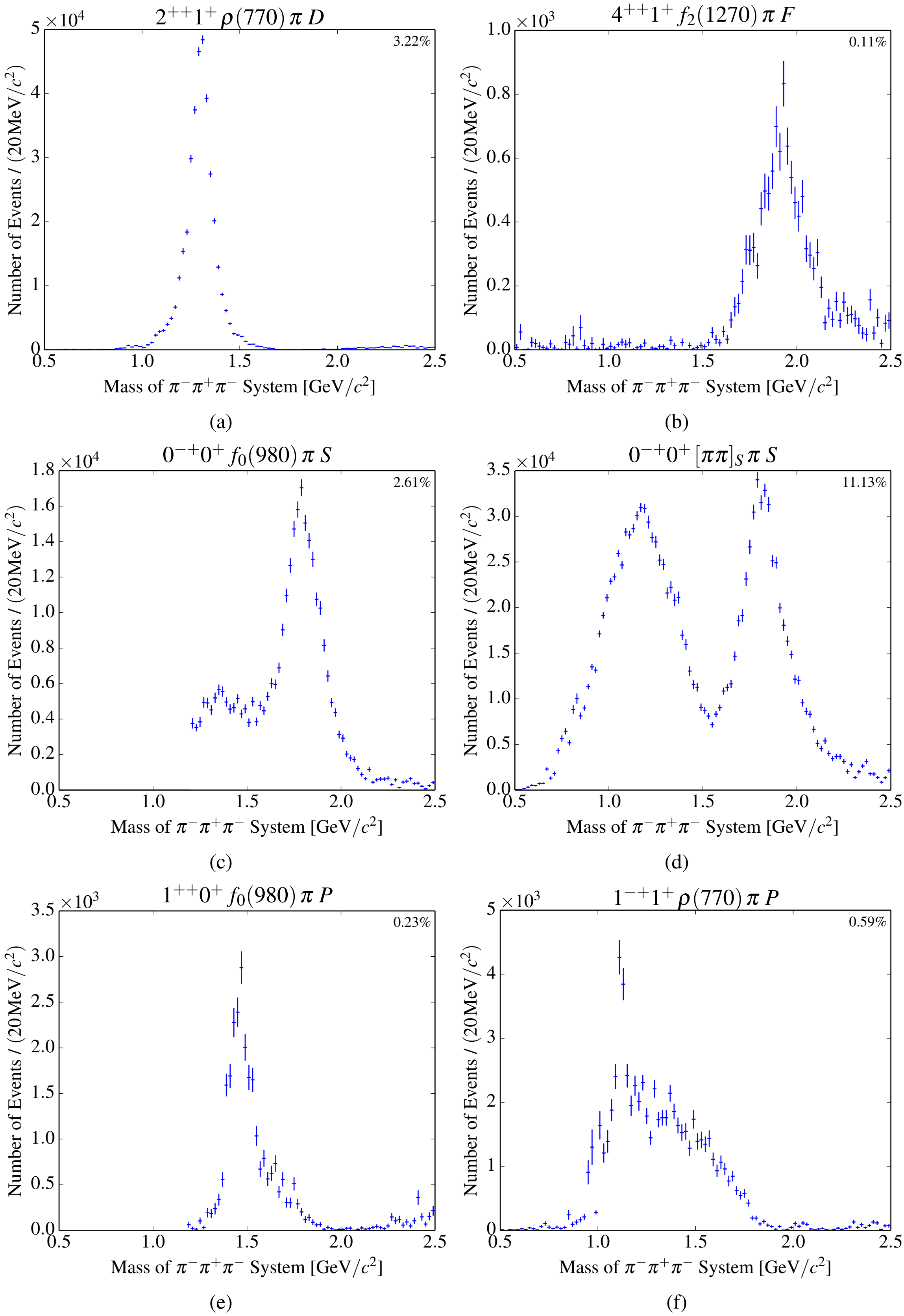

Figure 3.3: Intensity plots of waves that were well studied in previous analyses.

Figure 3.3 shows a collection of waves, that are important for this analysis for various reasons. The first row (figures 3.3a and 3.3b) are two very stable waves which in previous analyses have always been found and showed no real change in the shape of the peaks, independent of the model. The model selection is expected to produce a very similar result in these two waves. In the middle row (figures 3.3c and 3.3d), two waves with $J^{PC} = 0^{-+}$ are presented. In low to intermediate regions of $m_{3\pi}$, unphysically large destructive interference terms that result in fluctuating intensity were observed. Thresholds on certain waves (see figure 3.3c at $1.2\,\mathrm{GeV}/c^2$) had to be introduced to stabilize the fit results. Therefore, similar artifacts are also expected to appear in the low-mass region in the results of the model selection, which will require the introduction of thresholds in some waves. The lower row in figure 3.3 shows of two waves that contain resonances that have been in the scientific spotlight recently. The $1^{++}0^{+} f_0(980)\pi P$ wave in figure 3.3e contains the newly found $a_1(1420)$ resonance [5] while figure 3.3f shows the spin-exotic $1^{-+}0 + f_0(980)\pi P$ wave, the resonance content of which is discussed controversially. It will be interesting to see, whether these waves show any model dependence with in the comparison of the result from the model selection to these reference results.

3.1.3 Fit Stability

With the high dimensionality of the likelihood function, it is valid to question whether the fit always finds the global maximum of the likelihood function. For this reason, 30 fit attempts with random starting values are performed in each bin of $m_{3\pi}$.

Figure 3.4 shows the likelihood spread of the fit results for every attempt over the whole analyzed mass range. The y-axis shows the difference in likelihood of the fit results to the best likelihood value found in the respective bin of $m_{3\pi}$. If the fit were perfectly stable, the same maximum likelihood value would be found in every fit result. Aside from a few outliers, this is the case for the mass range above $1\,\mathrm{GeV}/c^2$ and one can conclude that the fit is stable in this range. The zoomed view in figure 3.4b shows that below $1\,\mathrm{GeV}/c^2$, there is more instability due to some local maxima close to the largest found maximum likelihood. This phenomenon is the reason why the reference wave set has thresholds in some waves and is discussed in depth in section 4.2.

3.2 Wave Pool

As mentioned above, the wave pool is the set of all possibly contributing waves, from which we choose the wave set. The composition of the wave pool depends on several factors, which can be divided into the partial-wave properties of the production and decay of the intermediate state X^-. On the production side we have the allowed quantum numbers $I^G\, J^{PC}\, M^{\varepsilon}$ of the X^-. As it was already derived in section 1.1.4, we will assume $I^G = 1^-$. The maximum allowed spin J and the corresponding spin-projection M are the components that determine the size of the wave pool. In this analysis, the upper limit of J is set to 6. Waves with large spin-projections are suppressed and thus the maximum M is set to 2. Each wave exists with positive and negative reflectivity. On the decay side the important parameteres for the wave-pool size are the number of isobars, which was already discussed in section 2.2.3, and the maximum angular momentum L between the isobar and the bachelor pion, which has an upper limit of 6 as well.

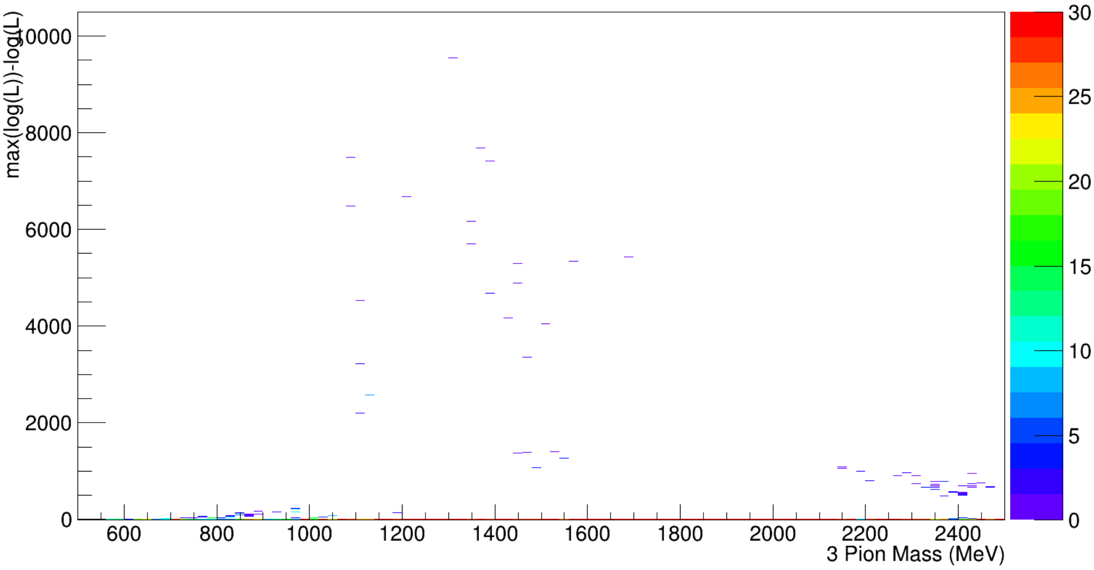

(a)

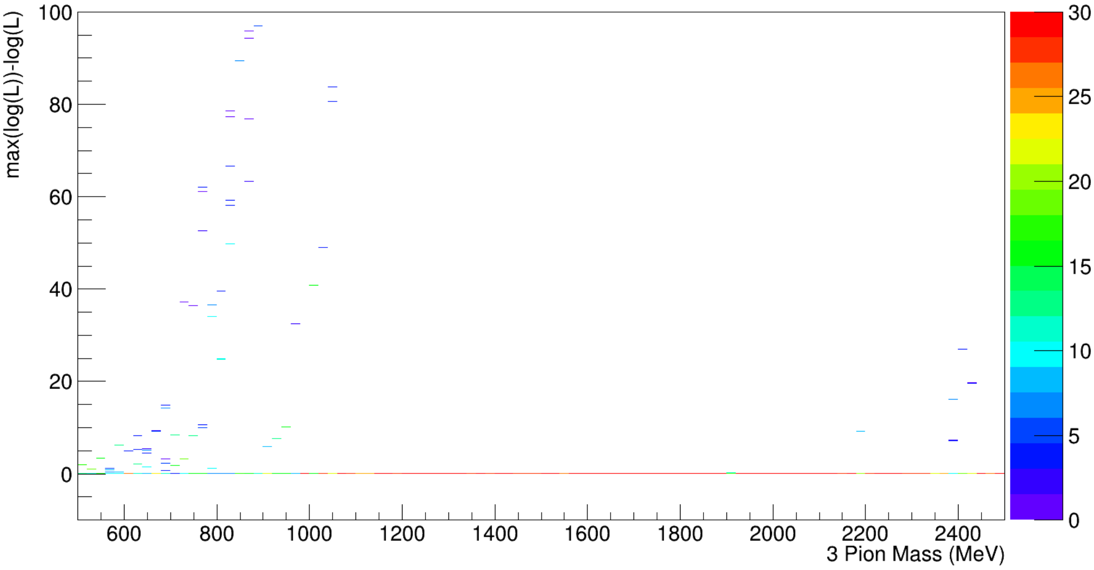

(b)

Figure 3.4: Scatter plots of the distance to the likelihood maximum for each fit attemt over the analyzed mass range. In (a) all fit attempts are shown, while (b) shows a zoomed view of the range of up to 100 likelihood difference.

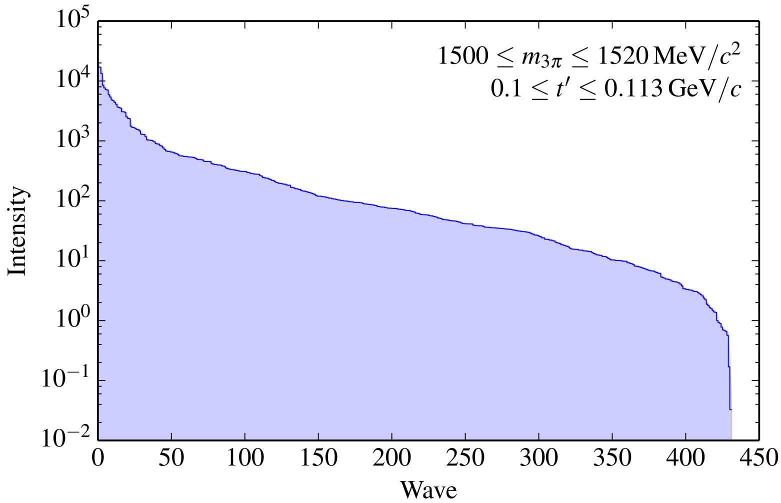

Figure 3.5: Intensity histogram of a result of a fit with the full wave pool. The waves on the x-axis are ordered by decreasing intensity.

Permuting all of the possible quantum numbers and the possible decay channels amounts to a wave pool consisting of 432 partial waves. The complete wave pool is listed in appendix B.

3.3 Partial-Wave Decomposition Using the Whole Wave Pool

The basic idea of the model selection procedure is to perform a partial-wave decomposition using the whole wave pool. The quantity that determines how important a partial wave is to describe the data, is the intensity of the wave. Therefore, we define a wave with a small intensity to be insignificant to the description of the data. This is valid only when all waves that contribute to the data are in the wave pool, which is given since every conceivably contributing wave was included.

Figure 3.5 shows an example of a result of a PWA fit with the wave pool, where the waves are ordered by intensity in decreasing order. Since not every wave from the wave pool can contribute to the total intensity, one can conclude that too many free parameters are used in this fit and therefore the wave set needs to be reduced. On the one hand, one could use a arbitrary fixed wave-set size and omit all waves after the size is reached, on the other hand one could choose an arbitrary intensity value after which a wave is deemed non-essential and remove all smaller waves from the wave set. Figure 3.5 reveals why cutting off the wave set with either method is not optimal: the intensity distribution is continuous and as a consequence it would be hard to make an argument for one cut-off point over the other. The choice would be arbitrary and would therefore result in a biased analysis.

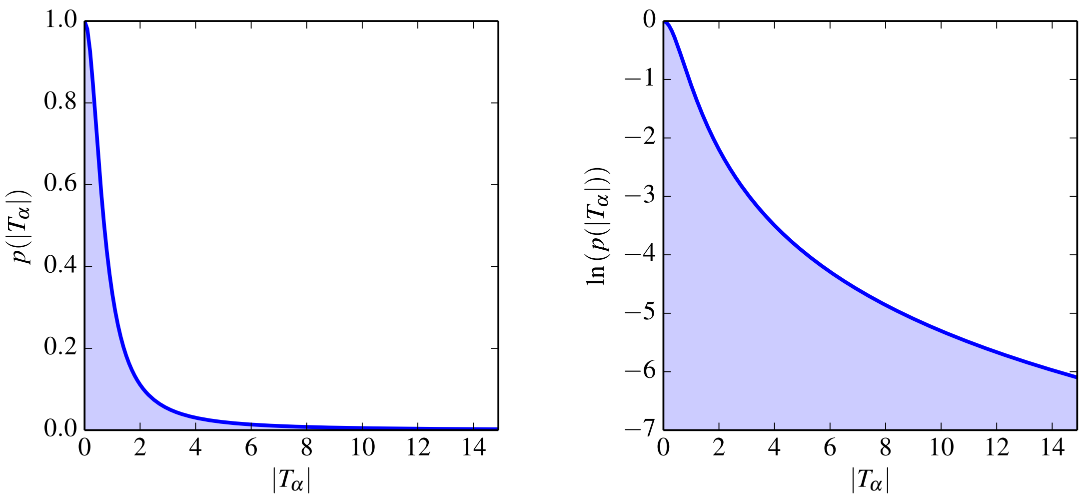

(a) (b)

Figure 3.6: The half-Cauchy prior function (a) and its logarithm (b).

3.4 Half-Cauchy Priors

From the standpoint of Bayes' theorem the analysis looks as follows:

$$P(M_k|\mathbb{E}) = \frac{P(\mathbb{E}|M_k)\,P(M_k)}{\sum_{k'} P(\mathbb{E}|M_{k'})\,P(M_{k'})} \tag{3.1}$$

Let M_k be a PWA model with k enumerating the possible sets of partial waves while $\mathbb{E}$ represents the set of measured events with their kinematic distributions.

The denominator in equation (3.1) represents the evidence, which is the probability to measure the data independent of a specific model. The evidence is difficult to calculate, because the sum over all possible models is hard to compute. But since we compare models by always using the same data, we can assume this term to be constant. The posterior probability $P(M_k|\mathbb{E})$ is therefore proportional to the product of the likelihood $P(\mathbb{E}|M_k)$ and the prior probability $P(M_k)$. The former represents the conditional probability of the model given the data, whereas the likelihood is the probability of the data given the model. Until now, the prior was assumed to be flat, $P(M_k) = \text{const}$, and in conclusion the posterior is proportional to the likelihood. If we ignore normalization, we can formulate the equation

$$\mathcal{P} = \mathcal{L}\,p \tag{3.2}$$

with the unnormalized posterior $\mathcal{P}$, the likelihood $\mathcal{L}$ and the prior p.

According to Bayes' theorem, the prior is a way to incorporate previous knowledge into the analysis. By maximizing equation (3.2) instead of the likelihood, one can include additional constraints. Applied to this analysis, this means that the best model should consist only of important waves and that insignificant waves should not be included in the model, even if they increase the likelihood. The prior should therefore prefer small intensities, which effectively eliminate the insignificant waves, without preventing high intensity waves to appear.

We write down the half-Cauchy prior function:

$$p(|T_\alpha|; w = 0.5) = \frac{1}{1 + \frac{|T_\alpha|^2}{w^2}}, \tag{3.3}$$

with the variable $|T_\alpha|$, which is the absolute value of the transition amplitude of the partial wave α, and the width of the prior w. For this analysis, w is set to 0.5. The function has the shape of a Breit-Wigner distribution, but is defined only for positive values. With this prior, the posterior probability changes to:

$$\mathcal{P}(T; \mathbb{E}) = \mathcal{L}(T; \mathbb{E}) \prod_\alpha p(|T_\alpha|) \tag{3.4}$$

$\mathcal{L}(T; \mathbb{E})$ is the likelihood as in equation (2.31). Since we used the logarithm of the likelihood function for the maximum likelihood fit, the same principle applies to the posterior probability:

$$\ln\left[\mathcal{P}(T; \mathbb{E})\right] = \ln\left[\mathcal{L}(T; \mathbb{E})\right] + \sum_\alpha \ln\left[p(|T_\alpha|)\right] \tag{3.5}$$

Figure 3.6 shows the prior function and, most importantly, the effect of the prior on a logarithmic scale. We can see that for transition amplitudes $|T_\alpha| = 0$ the log prior is also zero. Therefore, the posterior is just the likelihood. For larger transition amplitudes the prior acts as a penalty factor that lowers the posterior. Consequently, when we use this posterior function, the transition amplitudes have an incentive to be zero, in particular when they are already of the order of 10 or smaller. The long tail of the log prior ensures that high-intensity partial waves are not distorted considerably by the prior.

3.5 Selecting the Wave Set

Figure 3.7 demonstrates the effect of the prior on the fitted intensities of the partial waves. Due to its long tail, the prior has practically no effect on the waves with the highest intensities. For smaller waves, the difference to the posterior with half-Cauchy priors grows with decreasing intensity. The most important feature is a very steep drop of about 2 orders of magnitude at an intensity of about 10. This is where the half-Cauchy prior's incentive for the transition amplitudes to be zero dominates the posterior. The shape of the posterior function is changed by the half-Cauchy prior in such a way, that many small amplitudes are shifted close to zero. After the drop, the two curves are almost parallel. The reason for this behaviour lies again in the shape of the half-Cauchy prior. As can seen in figure 3.6, the prior has a maximum at $|T| = 0$. This has the effect that very small transition amplitudes are not penalized heavily and thus the transition amplitudes are not shifted to exactly zero but rather to very small values. Since all waves retain some intensity, the result of the model selection procedure, i.e. the wave set, has to be dependent of the position of the intensity drop.

Selecting the wave set is straight forward in most cases: all of the waves left of the drop, and thus all the high-intensity waves, are included in the wave set while the waves on the right side are excluded from the wave set. Figure 3.8 shows a rare case where selecting the wave set is not as clear as it

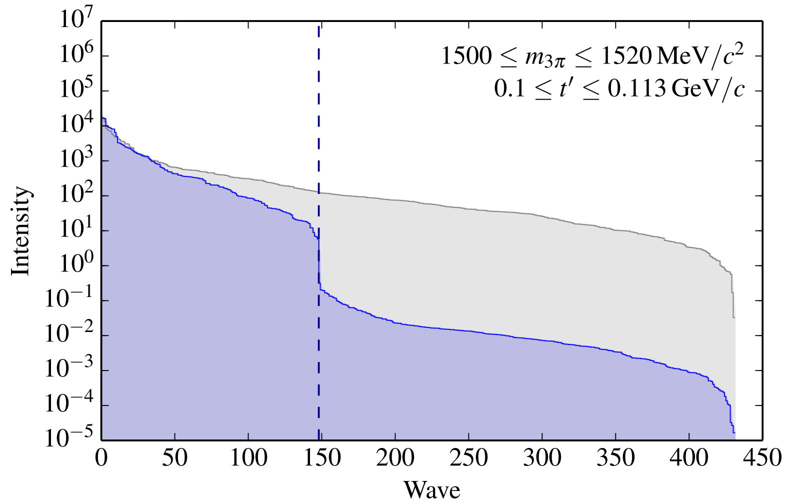

Figure 3.7: Intensity plot of a fit result with the whole wave pool, but applying the half-Cauchy prior to modify the posterior probability (blue). The waves on the x-axis are ordered by decreasing intensity. For reference, the result of a fit of the same data with the flat prior from figure 3.5 is overlaid in gray.

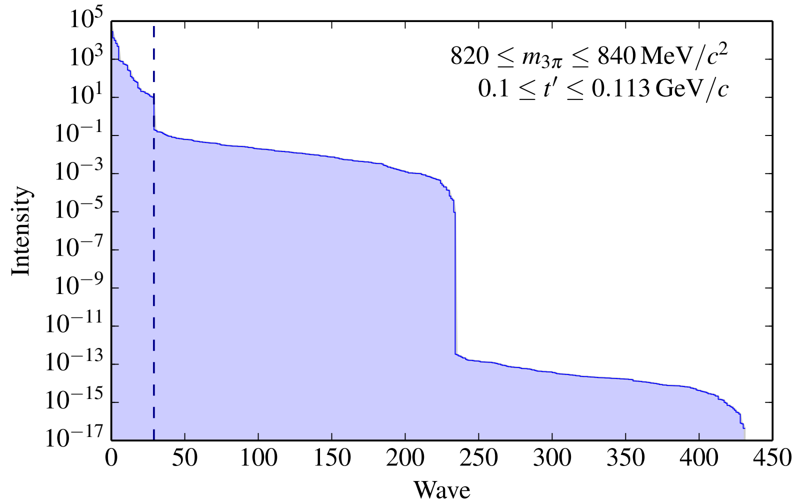

Figure 3.8: Intensity plot of a fit result with the whole wave pool, but applying the half-Cauchy prior to modify the posterior probability (blue). The biggest intensity drop in this example occurs at approximately the 230$^{\text{th}}$ wave at and intensity of about 10^{-4} events. The physically reasonable cut is at about the 30th wave at an intensity of 10 events, as indicated by the dashed line.

might appear. Due to the normalization in section 2.4 the unit of the intensity is in number of events. Obviously physical meaning can only be extracted if a wave contributes more than one event.

Therefore, the exact method of finding the correct cut-off for the wave set is by finding the biggest drop in relative intensity from one wave to the next, but only in a region between 1 and 100 events.

3.5.1 Fit Stability

This section will study the stability of the fits using the wave pool with the half-Cauchy prior and will try to answer the question, whether the fits are stable enough to consistently extract the same wave sets. Compared to the fits with the reference wave set described in section 3.1.2, the number of free parameters increases by a factor of five (88 compared to 432 waves). Additionally, the introduction of the half-Cauchy priors is expected to create many local maxima in the likelihood function. A local maximum may occur, when the prior forces a wave towards zero, making it harder for the optimizer to find the global maximum. Both factors destabilize the fit, making it necessary to use 100 instead of only 30 fit attempts. This amounts to a total of 10,000 fit attempts for the 100 mass bins.

Figure 3.9 shows likelihood scatter plots of all fit attempts over the analyzed mass range. Again, the y-axis shows the difference in likelihood of a fit result with respect to the best likelihood value found in the respective bin of $m_{3\pi}$. Compared to the almost perfect fit stability of the reference fit above $1\,\mathrm{GeV}/c^2$) (see figure 3.4), the stability of the model-selection fit is worse. In the overview in figure 3.9a, an accumulation of fit results approximately 50 units of likelihood above the best found likelihood is observed. In most attempts, the fit does not converge to the best found maximum likelihood, but to a local maximum instead. The zoomed view in figure 3.9b shows that the best likelihood value is found only once in most bins. The largest instabilities seem to be in the region around $1\,\mathrm{GeV}/c^2$ and at high masses. In these regions the accumulation is not as pronounced and the results scatter more to higher likelihood values. However, the difference to the next best fit result is often large, meaning that the found maximum is well-distinguishable.

Since the goal of these fits is only to select wave sets, it still has to be determined whether the unstable fits lead to different wave sets. To gauge the influence of the local maxima on the intensities of the partial-waves, intensity plots similar to the ones in section 3.1.2 are created, but using all fit attempts instead of just the best one in each bin. In figure 3.10 the $1^{++}0^{+}\rho(770)\pi S$ wave, which is the largest wave, is shown. The red points indicate the best fit result. Each colored bar represents the range, in which the fit results fluctuate for a certain percentile of all fit attempts. The color scale in the upper-right corner defines what color corresponds to which percentile of fit results. Therefore, the blue bars define the range, in which the best 10% of fit results fluctuate. As expected, when looking at the scatter plots in figure 3.9, the fluctuations at lower masses are bigger than at higher masses, where the results are essentially stable (at least in this wave). Since a wave enters the wave set as soon as it has non-zero intensity, one can assume that this happens consistently, when the blue bar does not touch the x-axis. For the wave in figure 3.10, this is the case at approximately $800\,\mathrm{MeV}/c^2$. This obviously only applies for this wave, which is likely one of the most stable waves in the wave pool. It still has to be confirmed for the other waves.

Figure 3.11 shows a wave with one of the smallest relative intensities ($< 0.01\%$) in the whole wave pool. Despite the small relative intensity, the red points show that the wave has non-zero intensity in the best fit attempt in a few bins and therefore enters the wave set in the respective bins. This is due to statistical fluctuations in the data. If the study were repeated, it is likely that other bins will have non-zero intensity.

A different effect is seen in figure 3.12. It should be highlighted, that this is the only plot that features a log scale on the y axis. Above $1.2\,\mathrm{GeV}/c^2$, the fit is perfectly stable, demonstrated by the small

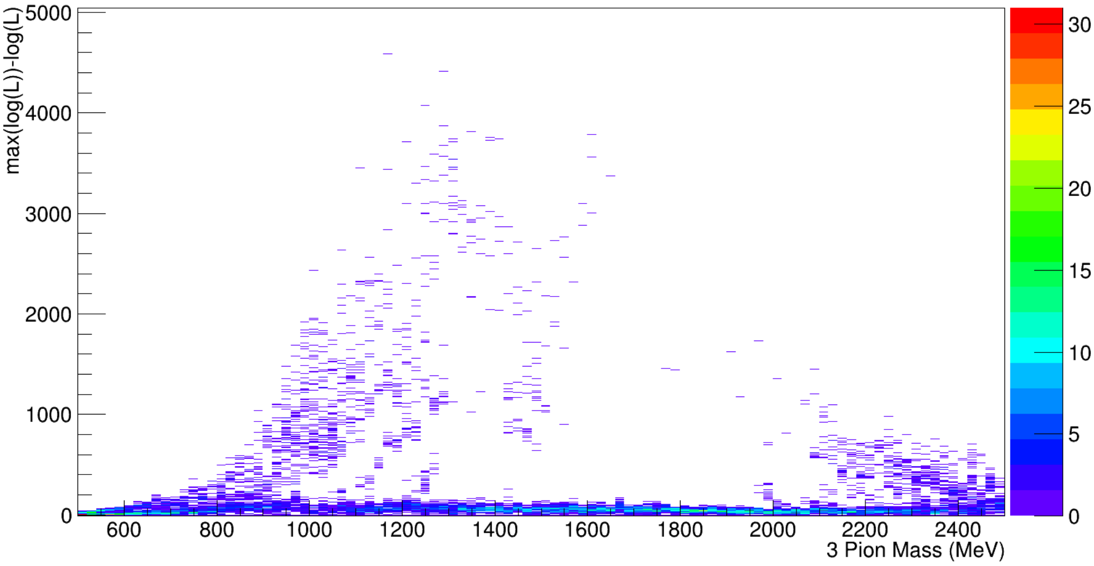

(a)

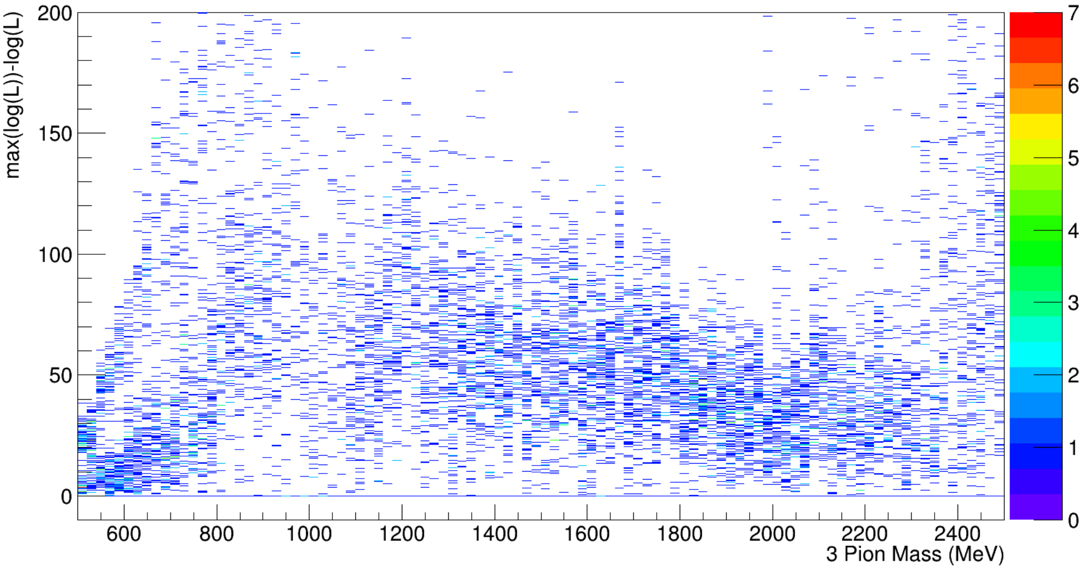

(b)

Figure 3.9: Distance to the likelihood maximum of each fit attempt with respect to the largest found likelihood over the analyzed mass range. In (a) all fit attempts are shown, while (b) shows a zoomed view with a maximum likelihood difference of 200.

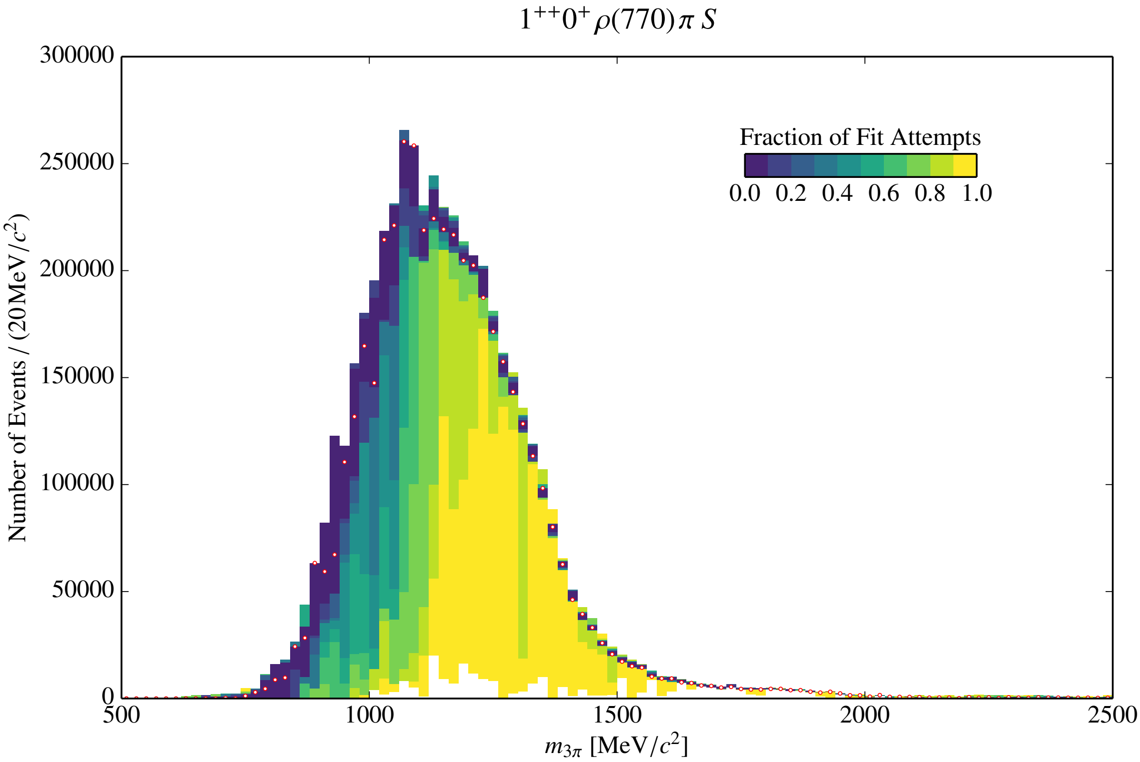

Figure 3.10: Intensity plot to study the fit stability of the largest wave. The red points indicate the best fit result. Each colored bar represents the range, in which the intensity fluctuates for a certain percentile of all fit attempts.

blue bars. Below this mass, in the region around 1 GeV/c^2, the intensity fluctuates wildly. These fluctuations have already plagued previous partial-wave analyses [3, 18] of the three-pion final state and are still not entirely resolved. The source for this behavior is assumed to be related to ambiguities between different partial waves in the model. At low $m_{3\pi}$, only the low-mass tails of isobars contribute, their shape is less distinct and thus harder to distinguish for the fit. Therefore, an unneeded additional freedom is introduced to the likelihood. The fit cannot determine a unique likelihood maximum, because two (or more) waves are so similar, that events can be attributed to both. This happens mostly with waves that have the same quantum numbers, especially in the 0^{-+} sector. The result are unphysically large fluctuations of intensity that are often magnitudes larger than the actual, physical intensity of the respective wave. When calculating the total intensity, these fluctuations cancel each other out by interfering destructively with one another. Since they tend to have large intensities, these ambiguous waves will remain in the wave set in the problematic region. An approach to exclude these waves will be presented in section 4.3.

To summarize, the fit stability of the fits using the wave pool with the half-Cauchy priors is sufficient for selecting the wave set in most cases. Although the likelihood scatter plots show that the fits do not reliably retrieve the global maximum of the likelihood function, the intensity plots reveal that this does not impact the selected wave sets in most cases. One exception to this are waves with very small intensity, which can drop in and out of the wave set, but the biggest challenge will be to manage the ambiguous waves in the low-mass region, which are not filtered out by the model selection.

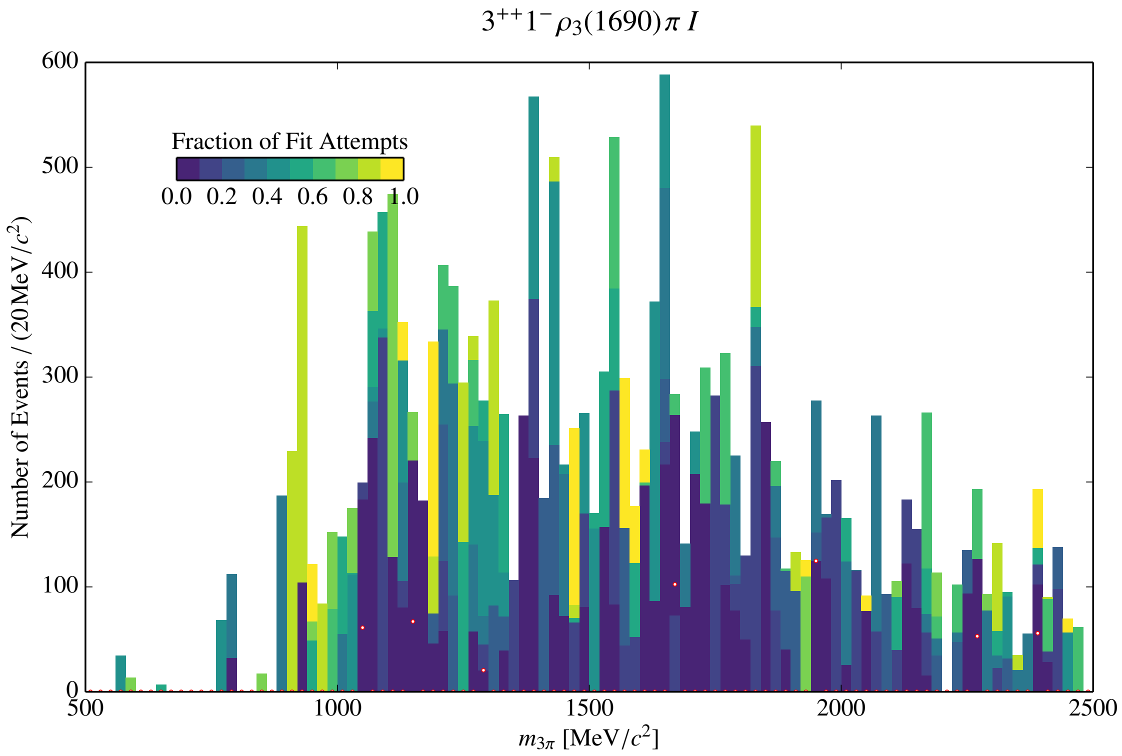

Figure 3.11: Intensity plot to study the fit stability of a small wave.

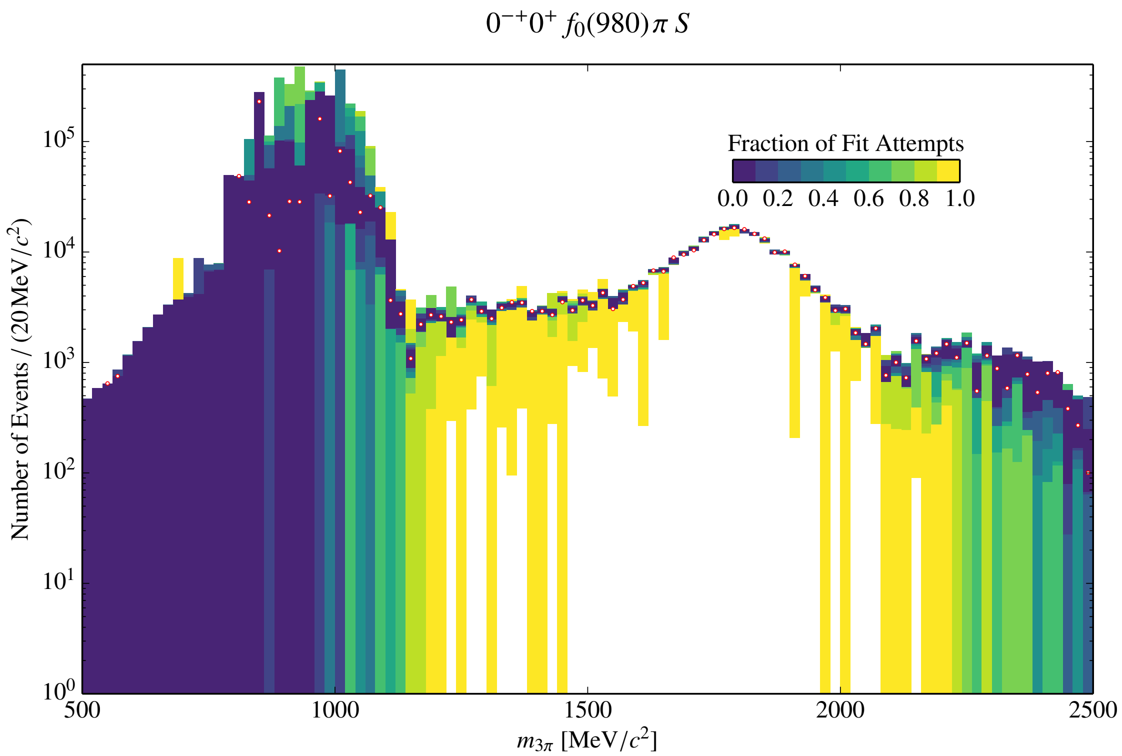

Figure 3.12: Intensity plot to study the fit stability of a wave with fluctuating intensity in the low-mass region. To show the stability of the fit above 1.2 GeV/c^2 a log scale is used for the y axis.

CHAPTER 4

Model-Selection Results

In this chapter, the model-selection procedure described in chapter 3 is applied to the data at hand. For this analysis, data from the 2008 COMPASS hadron run were used, based on the event selection described in section 1.2.3 to select diffractive dissociation events in the charged three-pion channel. The data are divided in narrow bins of the 3-pion mass $m_{3\pi}$ and reduced four-momentum transfer squared t' according to section 3.1.1.

The analysis is not done after we complete the model-selection process. Just comparing the resulting wave sets with the reference wave set is not sufficient, since altering the wave set slightly can have large effects on the fit results. Therefore, to inspect the effects of the different models, the wave sets from the model selection procedure have to be fitted to the data. These fit results, from now on referred to as *final fits*, can then be compared to the reference fits. This is done by comparing the intensity and the phase differences of the transition amplitude of every partial wave. For an agreement between the compared models, only the general shapes of the intensity and phase difference have to be matched. For an exact comparison the analysis has too large systematics and, as we learned in section 2.5, the approximation of the statistical uncertainty is not precise as well.

In the analysis, the model-selection wave sets are fitted to the data in 30 fit attempts in every $m_{3\pi}$ bin. The fit result is very stable. The outcome of the fit stability study is equivalent to the one presented in section 3.1.3 and is therefore not be written down explicitly.

Since the model selection procedure is executed independently in every bin of $m_{3\pi}$ and t', it results in different wave sets for each bin. Therefore, the size of the model-selection wave sets is studied in the first section. Next, the intensity and phase plots of final and reference fits of several selected waves are compared. The final analysis goal of this thesis will be to unify the different wave sets of the kinematic bins into one continuous wave set that can be used over the whole analyzed final-state mass range.

To verify the validity of the model-selection procedure, a study using Monte Carlo data should be performed. This was not within the scope of this thesis, but was successfully performed in the $\pi^-\pi^+\pi^-\pi^+\pi^-$ final state [7]. Because the $\pi^-\pi^+\pi^-$ final state is well explored from previous analyses [3, 5, 14, 15], the model-selection procedure can also be verified by comparison with these well-established results.

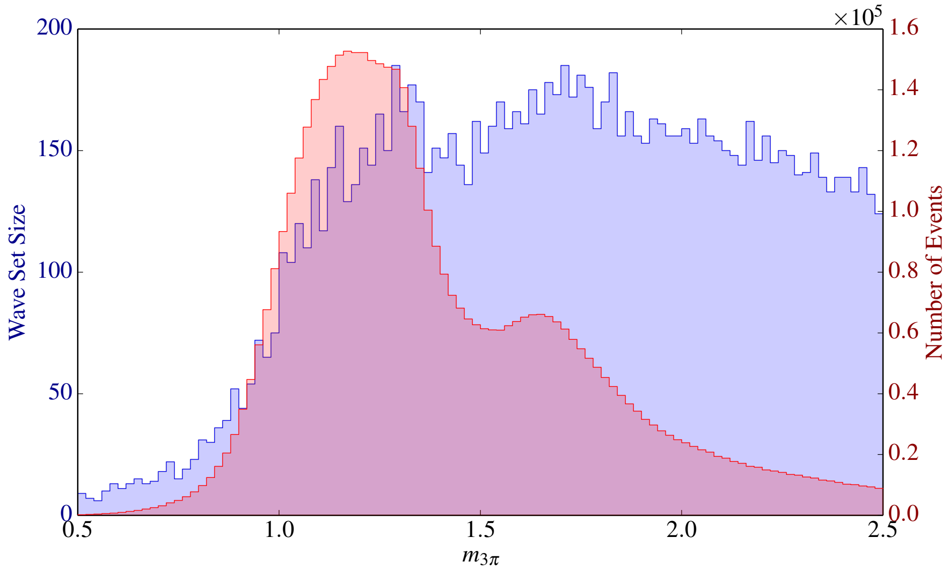

Figure 4.1: Wave set size (blue) and number of events (red) plotted for every mass bin in the lowest t' bin (from 0.100 to 0.113 $(\mathrm{GeV}/c)^2$.

4.1 Wave Set Size

The focus of this section will be the first step of the analysis — the fits with the whole wave pool and the half-Cauchy prior. Since we do the model selection procedure independently in each of the 100 $m_{3\pi}$ bins (using only the lowest t' bin), the resulting wave sets differ in each mass bin. Figure 4.1 shows that the wave set size varies between approximately 10 and 180 waves. This range is larger than that of the reference wave set, where the thresholds cause the wave set to vary between around 60 and 88 waves. Up to about 1.3 GeV/c^2 the wave-set size loosely follows the number of events. This is expected because with larger data samples smaller waves can be resolved and thus enter the wave set. Applying the same reasoning to high masses, one would expect the wave-set size to decrease, but this is not the case. The probable explanation for the wave sets staying larger than anticipated is the expected contribution of background processes[1] at higher masses influencing high-spin waves.

4.2 Comparison of Selected Waves

The main part of the analysis is to compare the transition amplitudes of partial waves obtained from reference and final fits. One would expect the most significant waves[2] to behave similarly, assuming that the analysis method works and that the reference wave set is reasonable. Deviations due to the different wave sets are to appear mostly in the smaller, low-intensity waves. Important aspects that have to be tracked are if there are waves from the reference wave set that become insignificant in the final fits and if there is notable intensity redistribution between waves. This will tell us something

[1] e.g. central production or Deck effect[2]
[2] In this context the significance of a wave is measured by its intensity.

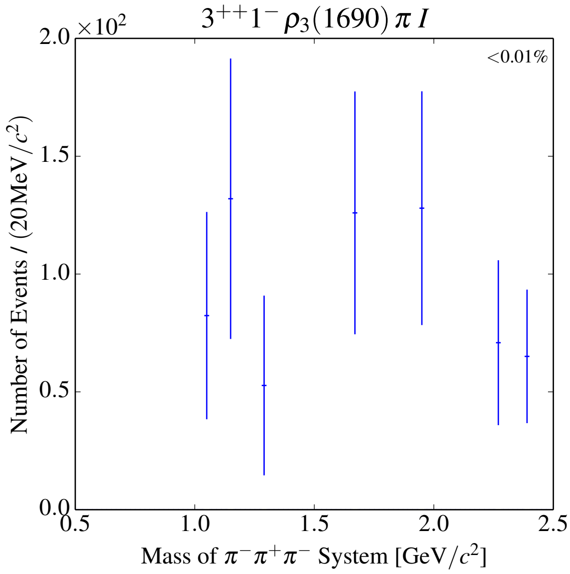

Figure 4.2: Intensity plot of an unstable wave obtained by executing the model selection on data in every mass bin. The wave is part of the model in only 7 of 100 mass bins.

about the systematic effect of the models on waves. The goal is to inspect if the fit results of the two methods are compatible – especially in significant waves – and analyze the reasons for eventual differences.

At this point, the expectations of the final fits have to be discussed. Since the model selection procedure selects different wave sets for every bin while removing insignificant waves, some waves will move in and out of the selected wave sets. Because continuity over multiple bins is not rewarded in the model selection, many waves will show discontinuous behaviour. This is highlighted by the fact, that every wave from the wave pool (which consists of 432 waves) is part of the selected wave set in one of the 100 bins of $m_{3\pi}$. Not a single wave from the pool is eliminated completely. This is a direct result of the chosen model selection procedure and is to be expected. An example for one of these partial waves is shown in figure 4.2.

By implication, this strengthens the argument, if continuous structures appear in the intensity of partial waves over a large mass range, that the wave is firmly part of the model. It is important to mention, that systematic errors far outweigh the statistical errors in the fit results. Therefore, compatibility between the reference and final fits is assumed when the general shape of the intensity and phase curve is conserved.

When comparing reference with final fits, the behavior of the partial wave amplitudes can be classified in four categories:

- *similar waves*, that share all important features over the whole mass range in the intensity and phase of the transition amplitudes
- *waves with differences*, where the behavior of the amplitudes has distinctly different features

Wave Name	Relative Intensity	Appearance
$1^{++}0^{+}\,\rho(770)\,\pi\,S$	24.20 %	Figure 4.3
$1^{-+}1^{+}\,\rho(770)\,\pi\,P$	0.44 %	Figure 4.4a
$2^{++}1^{+}\,\rho(770)\,\pi\,D$	2.00 %	Figure 4.4b
$2^{++}2^{+}\,\rho(770)\,\pi\,D$	0.05 %	Figure 4.4c
$2^{++}1^{+}\,f_2(1270)\,\pi\,P$	0.13 %	Figure 4.4d
$2^{-+}0^{+}\,f_2(1270)\,\pi\,S$	3.40 %	Figure 4.5a
$2^{-+}0^{+}\,f_2(1270)\,\pi\,D$	0.41 %	Figure 4.5b
$2^{-+}0^{+}\,\rho(770)\,\pi\,F$	0.96 %	Figure 4.5c
$2^{-+}1^{+}\,f_2(1270)\,\pi\,S$	0.21 %	Figure 4.5d
$4^{++}1^{+}\,f_2(1270)\,\pi\,F$	0.05 %	Figure 4.6a
$4^{++}1^{+}\,\rho(770)\,\pi\,G$	0.26 %	Figure 4.6b
$0^{-+}0^{+}\,f_0(980)\,\pi\,S$	6.48 %	Figure 4.7a
$0^{-+}0^{+}\,[\pi\pi]_S\,\pi\,S$	18.00 %	Figure 4.7b
$2^{++}0^{-}\,\rho(770)\,\pi\,D$	0.04 %	Figure 4.8a
$2^{++}0^{-}\,f_2(1270)\,\pi\,P$	0.02 %	Figure 4.8b
$2^{++}2^{+}\,f_2(1270)\,\pi\,P$	>0.01 %	Figure 4.8c
$3^{++}0^{+}\,\rho_3(1690)\,\pi\,I$	>0.01 %	Figure 4.8d
$1^{++}1^{+}\,f_2(1270)\,\pi\,F$	0.04 %	Figure 4.9a
$4^{-+}0^{+}\,\rho(770)\,\pi\,H$	0.06 %	Figure 4.9b
$5^{++}1^{+}\,\rho(770)\,\pi\,G$	0.14 %	Figure 4.9c
$5^{++}1^{+}\,\rho(770)\,\pi\,I$	0.02 %	Figure 4.9c
flat	0.14%	Figure 4.10

Table 4.1: Overview of the waves presented in this section with their relative intensity.

- *zero waves*, where the partial waves were included in the reference wave set, but are removed by the model selection procedure in most $m_{3\pi}$ bins

- *newly found waves*, that have continuous intensities in the final fits, but are not included in the reference wave set

Table 4.1 shows the notable waves that are presented in this thesis with their relative intensity (calculated with the final fits) and where they appear in the text.

4.2.1 Similar Waves

The majority of the waves show very similar behavior in both their intensity and phases. This section will cover a selection of such waves. For later analysis, the waves that exhibit resonant behavior are most important. From the $m_{3\pi}$ dependence of their intensity and phase plots one can extract the masses and widths of resonances. The phase motion of a wave can have implications on the physics

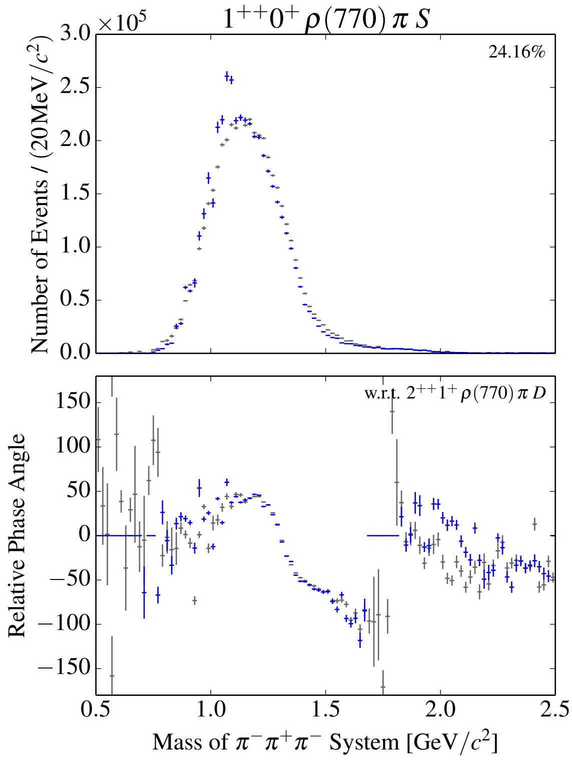

Figure 4.3: $1^{++}0^{+}\,\rho(770)\,\pi\;S$ wave with the largest relative intensity.

behind the intensity curve. For example, a phase motion in the mass range of an intensity peak usually implies resonant behavior. Because we have to rely on a reference wave to show the phase motion, optimally this reference wave should have a constant phase, so that the resulting relative phase curve is caused by the phase motion of the examined wave and not the reference wave. A resonance should result in a 180 degree phase motion, but in practice this is hard to achieve. Usually, the reference wave does not retain a constant phase throughout the relevant mass region, or the examined wave contains more than one resonance. This makes the phase motion information an important input for the subsequent analysis, the mass-dependent fit, which has been performed in previous theses [14, 15] for several partial waves using the reference wave set. Most of the waves that are used to extract resonance parameters will be discussed in this thesis.

The wave with the, by far, highest intensity is the $1^{++}0^{+}\,\rho(770)\,\pi\;S$. It is shown in figure 4.3, which contains two plots. Both plots share the same $m_{3\pi}$ axis. The top graph shows the intensity distribution. The bottom one shows the phase motion of the partial-wave amplitude with respect to the reference wave. In this case, the $2^{++}1^{+}\,\rho(770)\,\pi\;D$ wave (see figure 4.4b) was used to generate said plot. In all figures the blue color will correspond to fits with the model selection wave sets, while the gray color indicates fits with the reference wave set. The relative intensity in the top right corner is calculated with the final fit.

The intensity maximum corresponds to the $a_1(1260)$ resonance. Since it has non-vanishing intensity over almost the whole analyzed mass spectrum, it is used as reference wave for the following phase angle plots, unless mentioned otherwise. Both fit results show the same general shape in both the intensity as well as the relative phase angle. The bump in intensity at 1.1 GeV/c^2 can probably be attributed to model instability in the the low mass region (details in next section about different waves).

Figure 4.4 shows the spin-exotic $1^{-+}1^{+}\rho(770)\pi S$ wave (figure 4.4a) and three waves (figures 4.4b-d) in the $J^{PC} = 2^{++}$ sector that show the $a_2(1320)$ resonance. For all waves, the phases, as well as intensities for both methods match well, except for two data points in figure 4.4c, which show deviations from the reference wave set.

Figure 4.5 shows waves in the $J^{PC} = 2^{-+}$ sector. The peaks in figures 4.5a, 4.5c and 4.5d can be identified as the resonance $\pi_2(1670)$ and the intensity maximum in figure 4.5b wave as the $\pi_2(1880)$. All plots show good agreement between the two different analysis methods. In the intensity plots in figures 4.5b and 4.5c a smaller intensity in the high mass region with the model selection method is notable. These reduced tails of the resonances are a notable difference to the reference fits. In the same region, the phase motion is flat with the model selection procedure, instead of going back down with the reference wave set. Another interesting effect of the model selection procedure can be observed best in the phase angle diagrams. In the majority of the low-mass bins, the phase angle is zero, meaning that the respective wave is not part of the wave set. The intensity in these bins was low enough for the half-Cauchy prior to eliminate the wave, effectively introducing a threshold on that wave.

A similar picture is seen in the $J^{PC} = 4^{++}$ sector. Both waves in figure 4.6 have a peak attributed to the $a_4(2040)$. Again, the fit results between the model selection and the reference wave set are in good agreement. The only notable difference is in the high-mass tail in figure 4.6a, where the intensity with the model selection method is a bit reduced. Again, in the low mass region the waves are left out of the wave set in most bins.

4.2.2 Waves with Differences

In figure 4.7 we see two examples of waves with notable differences in their behavior with the different models. The discrepancies occur almost exclusively in regions that are thresholded in the reference wave set (below 1 GeV/c^2 in figure 4.7a below approximately 1.5 GeV/c^2 in figure 4.7b) and can best be seen in the top plots of each column. These unphysically large fluctuations are attributed to destructive interference between ambiguous waves (see section 3.5.1). The intensities of the two 0^{-+} waves with the two methods are still in good agreement above the kinematic threshold. This shows that the problems are located only in lower mass bins in figure 4.7.

Taming the fluctuations is not a trivial task and was thus far handled by applying thresholds to certain waves, effectively eliminating them from the wave set in the low-mass region, where they should be small. This removes the additional freedom in the likelihood caused by the ambiguity and stabilizes the fit results. In the reference wave set, this is done for the $0^{-+}0^{+} f_0(980)\,\pi\,S$ wave in figure 4.7a and leads to the sudden disappearance of the gray data points at 1.2 GeV/c^2. Since this phenomenon is caused by interference with other waves, setting a threshold for one wave may cause other problematic waves to stabilize. This explains why figure 4.7b does not need a threshold in the reference wave set.

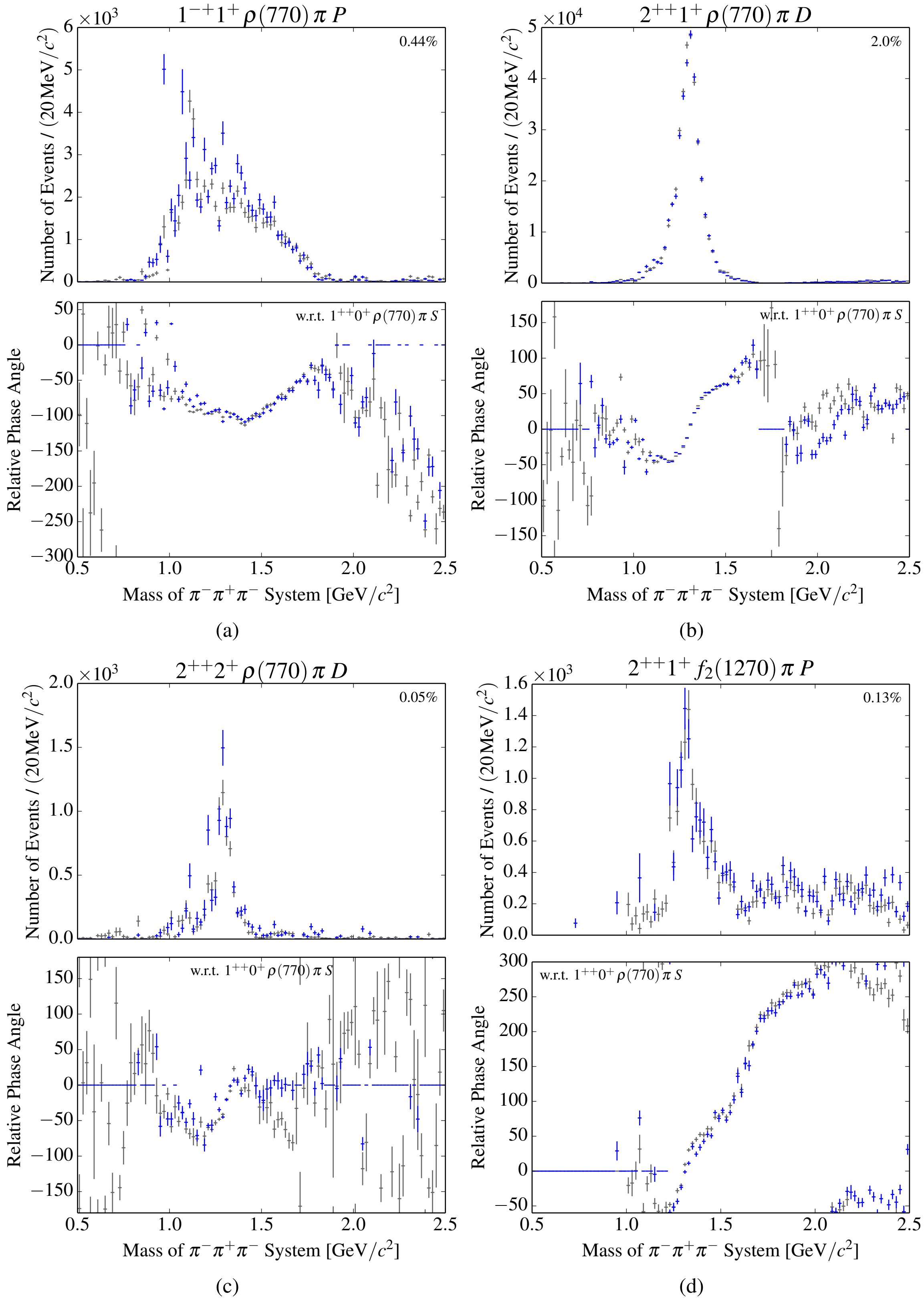

Figure 4.4: The spin-exotic $1^{-+}1^{+}\,\rho(770)\,\pi\;P$ wave (a) and three waves with $J^{PC} = 2^{++}$ (b-d).

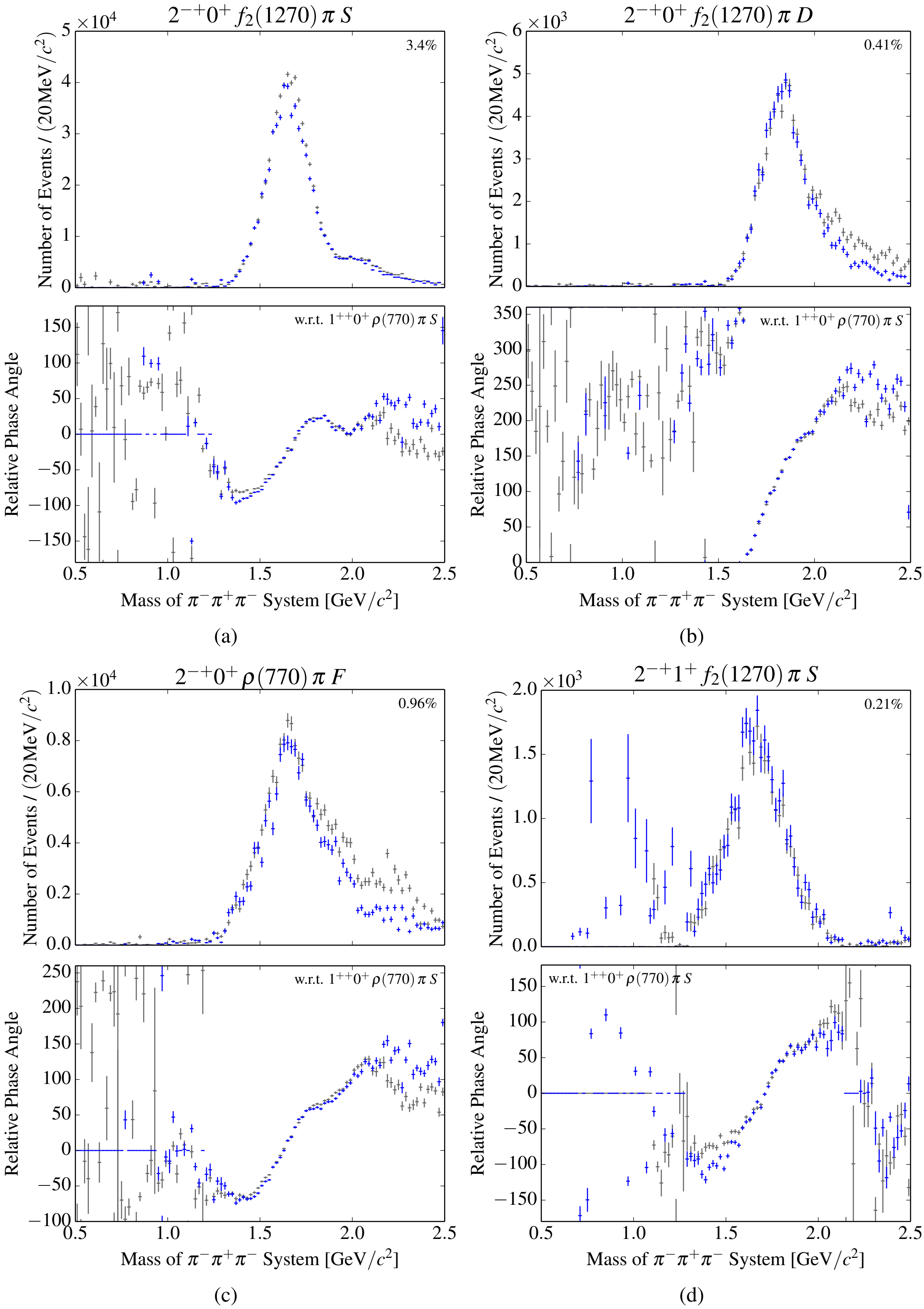

Figure 4.5: Four waves with $J^{PC} = 2^{-+}$.

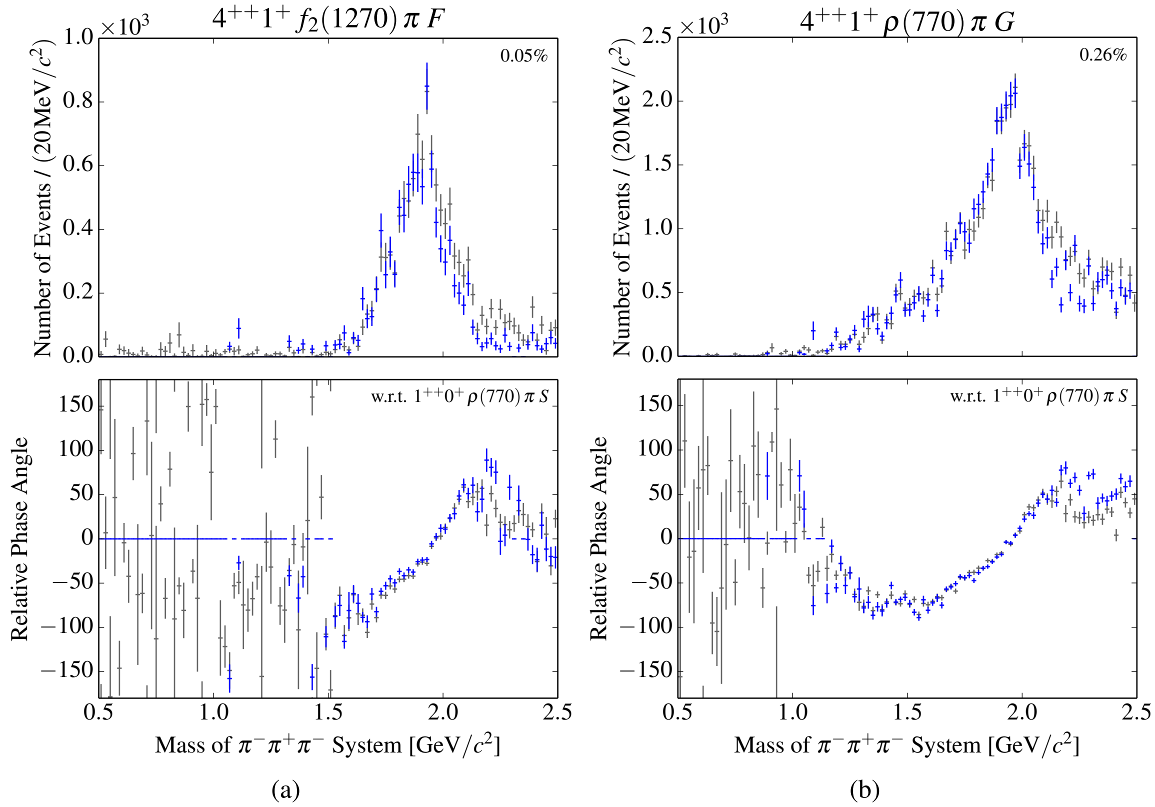

Figure 4.6: Two waves with $J^{PC} = 4^{++}$.

This section shows where the method to have an analysis that is as bias-free as possible seems to be limited, because continuity is not required. It is apparent, that the introduction of thresholds is unavoidable in the charged three-pion channel. This is the main motivation to implement a continuity requirement and introduce thresholds in a later analysis step (see section 4.3).

4.2.3 Zero Waves

One goal for using the model selection procedure is to examine, whether the reference wave set is the optimal model choice or at least close to it. An optimal wave set should not contain partial waves with vanishing intensities. This section will cover waves that are removed by the model selection procedure, but are included in the reference wave set.

Since the model selection procedure uses all waves of the wave pool at least once accross the analyzed mass range, strictly speaking no wave is completely eliminated from the overall wave set (see figure 3.11). But when the intensity of a wave resulting from the final fits shows no continuity in any part of the mass range, but shows continuity in the reference fits, it can be said with confidence that this wave is model dependent and has to be examined with care. Therefore, the waves that are discussed in this section are the waves, that have intensity over a large mass range in the reference fits, but lose all structure in the final fits. The most probable cause for the structures in the reference

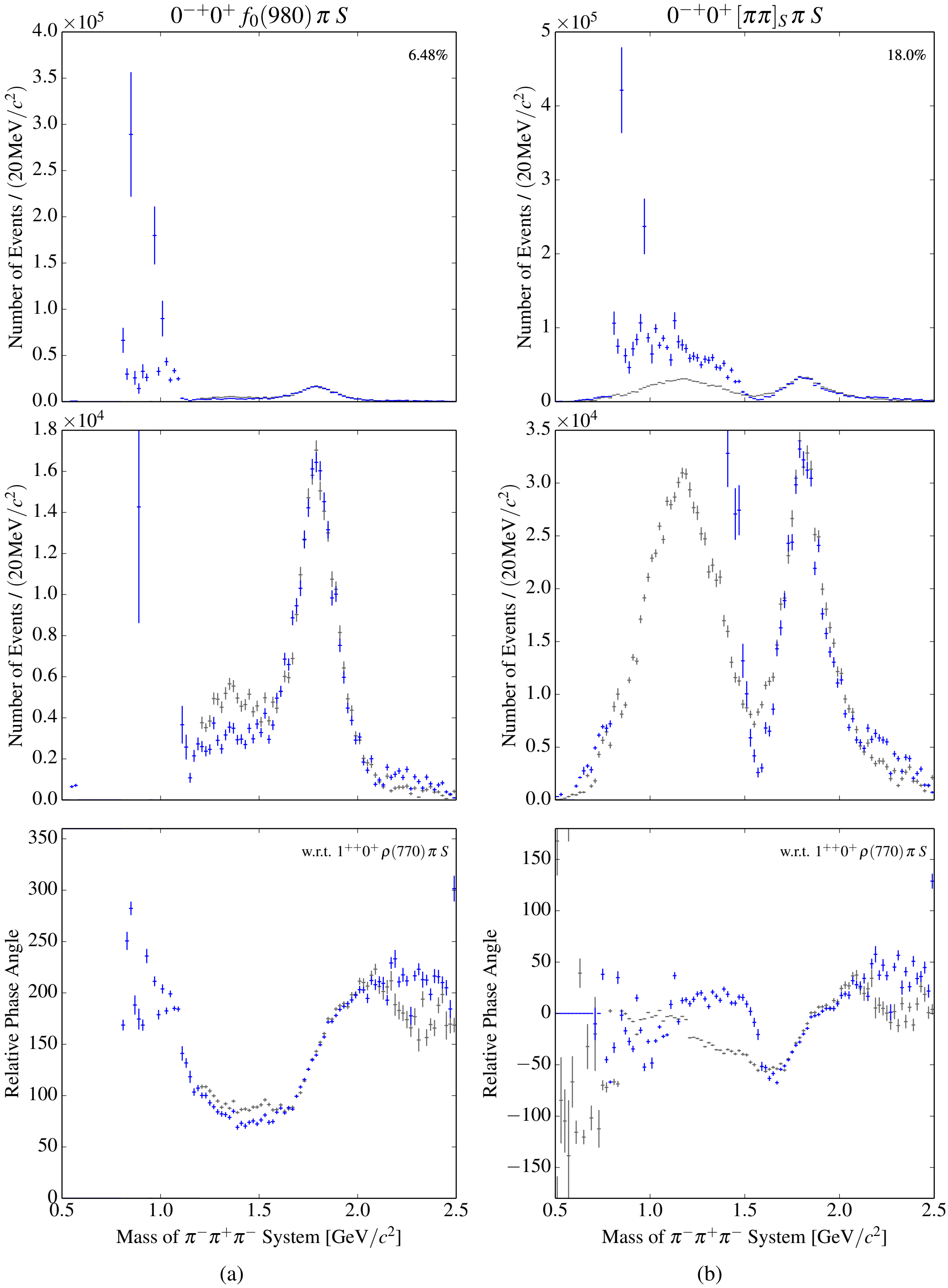

Figure 4.7: Two waves with $J^{PC} = 0^{-+}$ with discrepancies between the reference and final fits. The plots in the middle row are zoomed versions of the intensity plots in the top row.

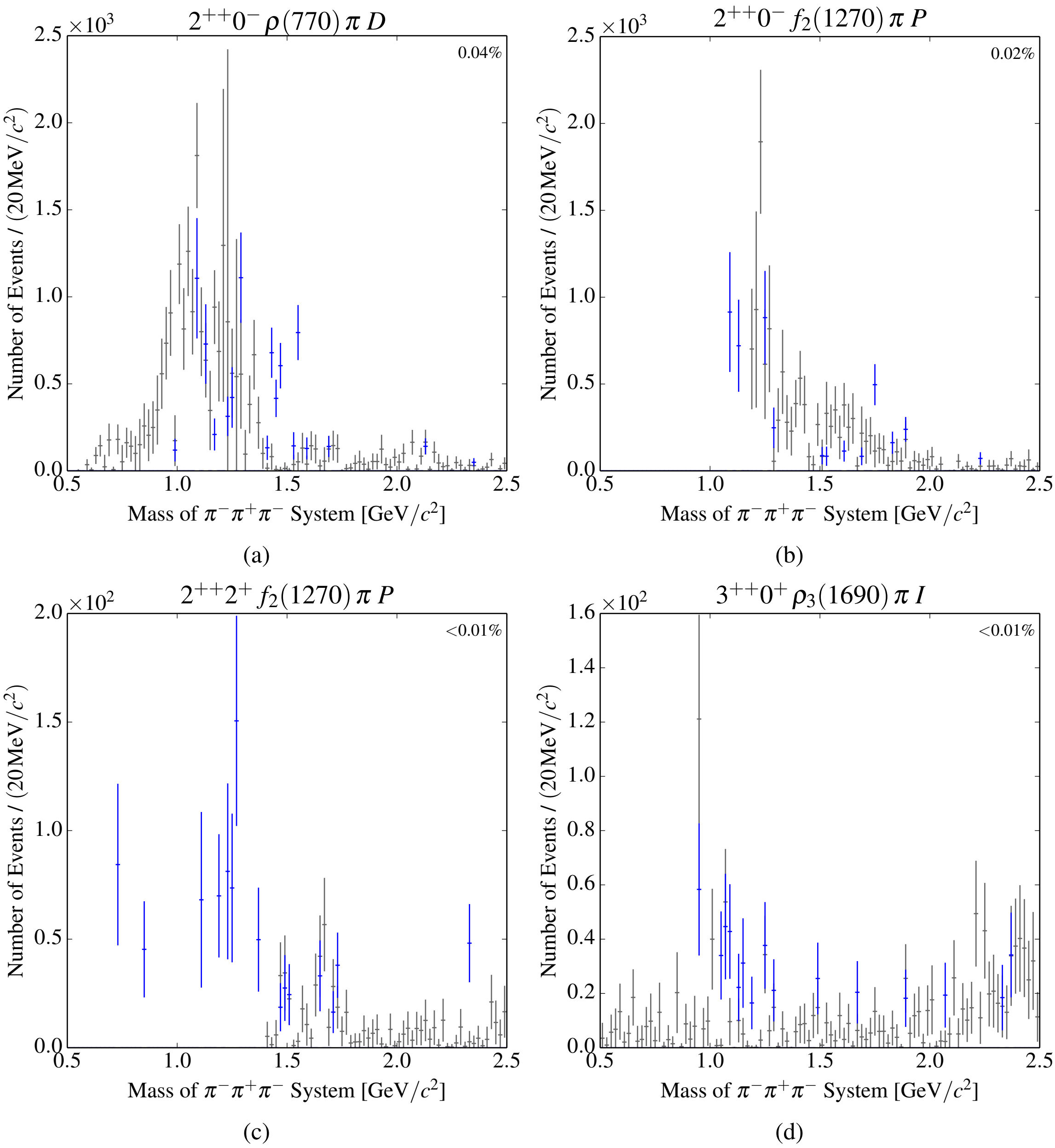

Figure 4.8: Examples for waves, that show intensity over a wide mass range in the reference fits, but lose these structures in the fits with the applied model-selection procedure.

fits is model leakage and non-resonant contributions.

Figure 4.8 shows four example waves, with negative and positive reflectivity, that demonstrate this behavior. The first thing that needs to be noted is that all of these waves have a very small relative intensity and thus do not contribute much to the total intensity. If this were not the case, the validity of either the model selection procedure or the reference wave set would need to be questioned. In figure 4.8 the blue data points appear sparsely over the whole mass range. In these plots only 10 to 20 data points out of 100 are present. Additionally, most points have large errors, making some of them compatible with zero. Some more zero waves are listed in table 4.3.

4.2.4 Newly Found Waves

The goal of using a large and systematically constructed wave pool was to study, whether some waves were overlooked in the hand-selected reference wave set. These waves should then be added in order to get an improved wave set. The results show, that, indeed, there are several waves, which were not included in the reference wave set that show continuous intensity and phase behavior. The classification of when a wave shows structure is of course subjective, but the number of newly found waves is of the order of ten, four of which are presented in figure 4.9.

The probably most noteworthy newly found wave is the $1^{++}1^{+} f_2(1270)\pi F$ wave shown in figure 4.9a. Despite its smallness of only 0.04% of the total intensity, one can identify a peak structure in the intensity plot at approximately $2.2\,\mathrm{GeV}/c^2$. Additionally, there is a clear phase motion in that region, which might hint at a resonance. Most of these newly found waves have high spin, which is not surprising, since the low-spin region was already well explored in the reference wave set. It is probable that most of the high-spin waves that entered the wave pool were never considered. This demonstrates the advantage of the model selection procedure. The high-spin waves are candidates for the Deck effect (see section 1.1.5), which is predicted to contribute at higher spins. Figures 4.9c and 4.9d show two $5^{++}1^{+}$ waves, the former with $L = 4$ and the latter with $L = 6$. Even though the signals are small, the plots show similar behavior in both, intensity and the phase. Additional newly found waves can be found in table 4.5.

4.3 Finding a Combined Wave Set

The results of the final fits are promising, but as mentioned in the beginning of section 4.2, there are many unstable waves that drop in and out of the wave set seemingly at random. This is best illustrated by comparing the incoherent isotropic (“flat”) wave of the final and the reference fits (see figure 4.10). Especially above $1\,\mathrm{GeV}/c^2$, there is almost no intensity in the final fit compared to the reference fit, because the fit has the freedom to choose from the whole wave pool.

The goal of this section is to combine the knowledge from the results of the final fit (large destructive interference in the low-mass region, zero waves and newly found waves) to create a new wave set, that is continuous in $m_{3\pi}$. From here on such a wave set will be called *combined wave set*. It should resemble the reference wave set, where we have basically one wave set for all bins with some waves

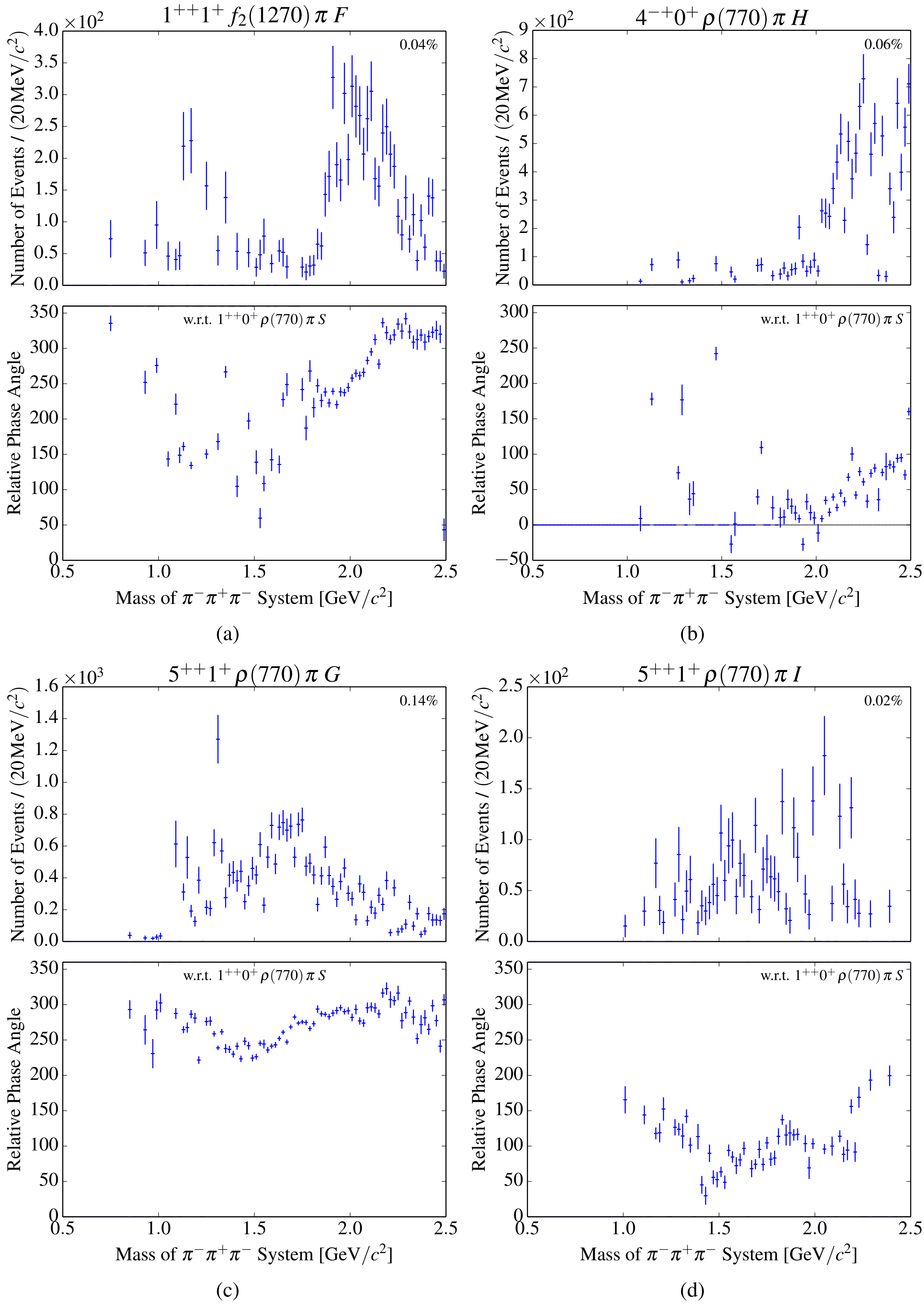

Figure 4.9: Four examples of newly found waves by the model selection procedure.

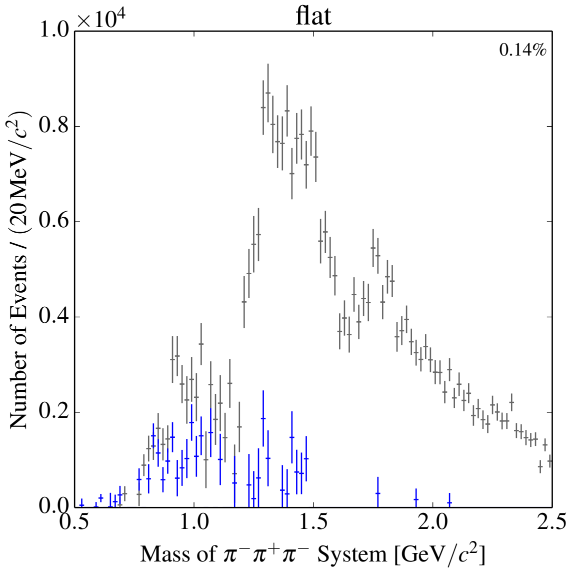

Figure 4.10: Intensity plot of the incoherent isotropic wave in the final fits (blue) and the reference fits (gray).

omitted below certain $m_{3\pi}$ thresholds. This raises the question how to select such a combined wave set. Having the results of the final fits would make it rather simple to hand select, but, since the premise of this thesis is to require the least human intervention possible, an algorithmic approach is used.

The basic idea to create the combined wave set is to select those waves, that have continuous intensity in the final fits. Since the model selection procedure does not demand continuity of waves in neighbouring bins, a strong argument can be made that a wave is required by the data, when it is found over a wide continuous mass range. This is certainly not the optimal approach[3], but as a proof of concept it shall suffice. To quantify the continuity of a wave, the biggest number of consecutive bins with non-zero intensity is used. The minimum number of connected bins to show structure was chosen to be 10. This is almost[4] the only user input of the analysis. 10 bins correspond to 10% of the analyzed mass range and are about the smallest number expected to potentially reveal peak-like structures. All waves that accomplish this criteria are accepted in the combined wave set. If a wave does not have intensity in 10 consecutive bins anywhere in the analyzed mass range it is left out of the combined wave set.

[3] Other arguments, like relative intensity or degree of intensity fluctuation are completely left out.
[4] Some thresholds had to be entered manually, more on that later.

$2^{-+}2^{+}\ f_2(1270)\,\pi\ S$	$2^{++}2^{+}\ f_2(1270)\,\pi\ P$	$2^{++}1^{+}\ \rho_3(1690)\,\pi\ D$	$3^{++}0^{+}\ \rho_3(1690)\,\pi\ I$
$4^{++}2^{+}\ \rho(770)\,\pi\ G$	$4^{++}2^{+}\ f_2(1270)\,\pi\ F$	$5^{++}0^{+}\ [\pi\pi]_S\ \pi\ H$	$5^{++}0^{+}\ f_2(1270)\,\pi\ H$
$5^{++}0^{+}\ \rho_3(1690)\,\pi\ D$	$1^{-+}0^{-}\ \rho(770)\,\pi\ P$	$1^{-+}1^{-}\ \rho(770)\,\pi\ P$	$1^{++}1^{-}\ \rho(770)\,\pi\ S$
$2^{++}0^{-}\ f_2(1270)\,\pi\ P$	$2^{++}0^{-}\ \rho(770)\,\pi\ D$	$2^{-+}1^{-}\ f_2(1270)\,\pi\ S$	$2^{++}1^{-}\ f_2(1270)\,\pi\ P$

Table 4.3: List of zero waves that are part of the reference wave set, but not of the combined wave set.

$0^{-+}0^{+}\ \rho_3(1690)\,\pi\ F$	$1^{++}1^{+}\ f_2(1270)\,\pi\ F$	$1^{-+}1^{+}\ f_2(1270)\,\pi\ D$	$1^{++}0^{+}\ f_0(1500)\,\pi\ P$
$1^{++}1^{+}\ f_0(1500)\,\pi\ P$	$2^{-+}0^{+}\ f_0(1500)\,\pi\ D$	$2^{-+}0^{+}\ \rho_3(1690)\,\pi\ F$	$2^{-+}1^{+}\ f_0(980)\,\pi\ D$
$2^{-+}1^{+}\ f_2(1270)\,\pi\ G$	$2^{++}1^{+}\ f_2(1270)\,\pi\ F$	$3^{-+}1^{+}\ f_2(1270)\,\pi\ G$	$3^{++}0^{+}\ \rho_3(1690)\,\pi\ D$
$3^{++}1^{+}\ f_0(980)\,\pi\ F$	$3^{++}1^{+}\ f_2(1270)\,\pi\ F$	$3^{++}1^{+}\ f_0(1500)\,\pi\ F$	$4^{-+}0^{+}\ \rho_3(1690)\,\pi\ P$
$4^{-+}0^{+}\ f_0(980)\,\pi\ G$	$4^{-+}0^{+}\ f_0(1500)\,\pi\ G$	$4^{-+}0^{+}\ f_2(1270)\,\pi\ I$	$4^{-+}0^{+}\ \rho(770)\,\pi\ H$
$4^{-+}1^{+}\ [\pi\pi]_S\ \pi\ G$	$4^{-+}1^{+}\ f_2(1270)\,\pi\ I$	$4^{-+}1^{+}\ \rho(770)\,\pi\ H$	$4^{-+}1^{+}\ \rho_3(1690)\,\pi\ P$
$4^{-+}1^{+}\ f_0(1500)\,\pi\ G$	$5^{++}1^{+}\ f_0(1500)\,\pi\ H$	$5^{++}0^{+}\ f_0(1500)\,\pi\ H$	$5^{++}0^{+}\ \rho_3(1690)\,\pi\ G$
$5^{++}1^{+}\ \rho(770)\,\pi\ G$	$5^{++}1^{+}\ \rho(770)\,\pi\ I$	$5^{++}1^{+}\ f_2(1270)\,\pi\ H$	$5^{++}1^{+}\ f_0(980)\,\pi\ H$
$5^{++}0^{+}\ \rho(770)\,\pi\ I$	$5^{++}1^{+}\ \rho_3(1690)\,\pi\ D$	$6^{-+}1^{+}\ f_0(1500)\,\pi\ I$	$6^{-+}1^{+}\ f_2(1270)\,\pi\ G$
$6^{-+}0^{+}\ f_0(1500)\,\pi\ I$	$1^{++}1^{-}\ [\pi\pi]_S\ \pi\ P$	$2^{++}1^{-}\ \rho(770)\,\pi\ D$	$2^{-+}1^{-}\ [\pi\pi]_S\ \pi\ D$
$3^{++}1^{-}\ \rho_3(1690)\,\pi\ S$	$3^{++}1^{-}\ f_2(1270)\,\pi\ P$	$4^{++}1^{-}\ \rho(770)\,\pi\ G$	$4^{-+}1^{-}\ [\pi\pi]_S\ \pi\ G$
$5^{++}1^{-}\ \rho(770)\,\pi\ I$	$6^{++}1^{-}\ \rho(770)\,\pi\ I$		

Table 4.5: List of newly found waves that are part of the combined wave set, but not of the reference wave set.

Performing this selection changes the wave set from 88 waves in the reference wave set to now 118 in the combined wave set. Table 4.3 lists the 16 waves that are not part of the combined wave set, even though they were in the reference wave set. Interestingly, all seven waves with negative reflectivity fall into this category. Conversely, this means that 72 of the 88 waves in the reference wave set were found by the model selection procedure and the subsequent filtering by continuity. Additionally, 46 new waves (see table 4.5) were found using this method. The complete wave set is listed in appendix C.

It was already mentioned when the reference wave set was introduced in section 3.1, that some waves have to be thresholded, because otherwise the fit results would exhibit unphysically large destructive interference at low masses. Obviously, the same is true for the combined wave set. Therefore, a rule to threshold critical waves has to be found. Since we used the continuity argument for creating the combined wave set, the thresholds can be derived in a similar manner. Let us assume, that an important wave can be identified by having intensity in ten consecutive bins. Conversely this means, that bins below the continuous region are not as important to describe the data. Therefore, the threshold for each wave is set at the 3π mass, which marks the low-mass border of the consecutive region. If a wave has multiple regions with 10 consecutive bins of non-zero intensity, the threshold will be imposed on the lowest-mass region, as to not eliminate regions with continuous intensity.

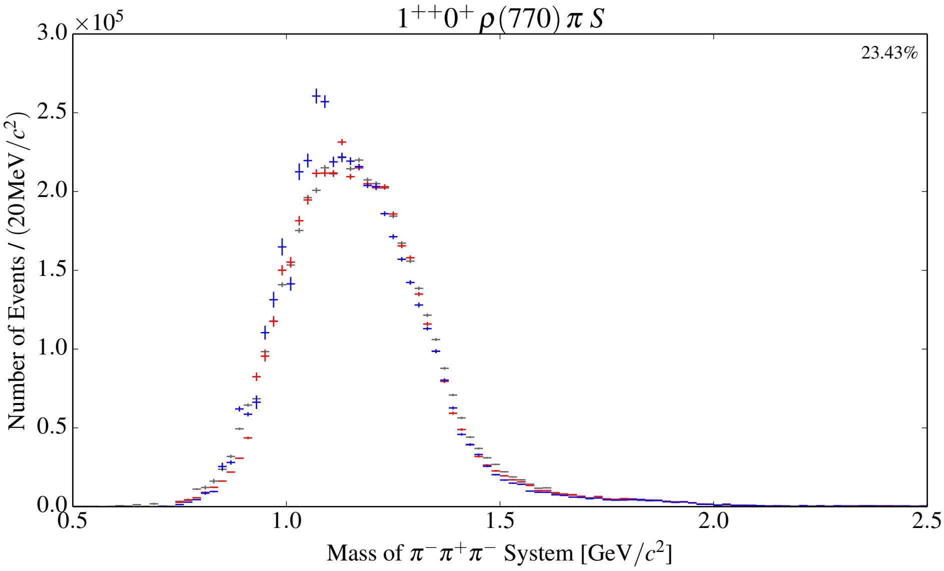

Figure 4.11: Intensity plot of the $1^{++}0^{+}\rho(770)\pi S$ wave, showing the $a_1(1260)$ resonance. The fits with the combined wave set are added in red. Final fits are indicated in blue, while the reference fits are gray.

Additionally, the thresholds from the reference wave set are applied to the combined wave set, overwriting the algorithmically found ones. This was done, because in some difficult regions (see figure 4.7a) this simple algorithm does not work well[5]. Since the thresholds from the reference wave set were worked out very thoroughly, they fix the few waves the algorithm had problems with.

4.4 Fits with the Combined Wave Set

Using the combined wave set another fit is performed. As with the reference and final fit, 30 fit attempts are used. The conclusion of the fit-stability analysis in section 3.1.3 applies to this fit as well. First off, it will be examined how the combined wave set behaves in the important waves with more or less known resonance content that are discussed in the introduction of the reference wave set in section 3.1.2. Next some of the newly found waves are analyzed.

The wave with the largest intensity, the $1^{++}0^{+}\,\rho(770)\,\pi\,S$ wave, is shown in figure 4.11. The gray points mark the reference fit while the blue points represent the final fit. The red data points indicate the fit results with the combined wave set. The relative intensity of each wave is calculated based on the fits with the combined wave set. The peak-like structure at 1.1 GeV/c^2 observed in the final fit vanishes in the fit with the combined wave set, which exhibits a much smoother intensity distribution much closer to that of the reference fit.

Figure 4.12 shows four waves that already had similar behaviour with the final fit compared to the reference fit. In the fits with the combined wave set, not much has changed. A notable observation is, that in these four waves the automatic thresholding of the waves seems to work as intended.

[5] The algorithm fails, when the destructive interference takes place in 10 consecutive bins.

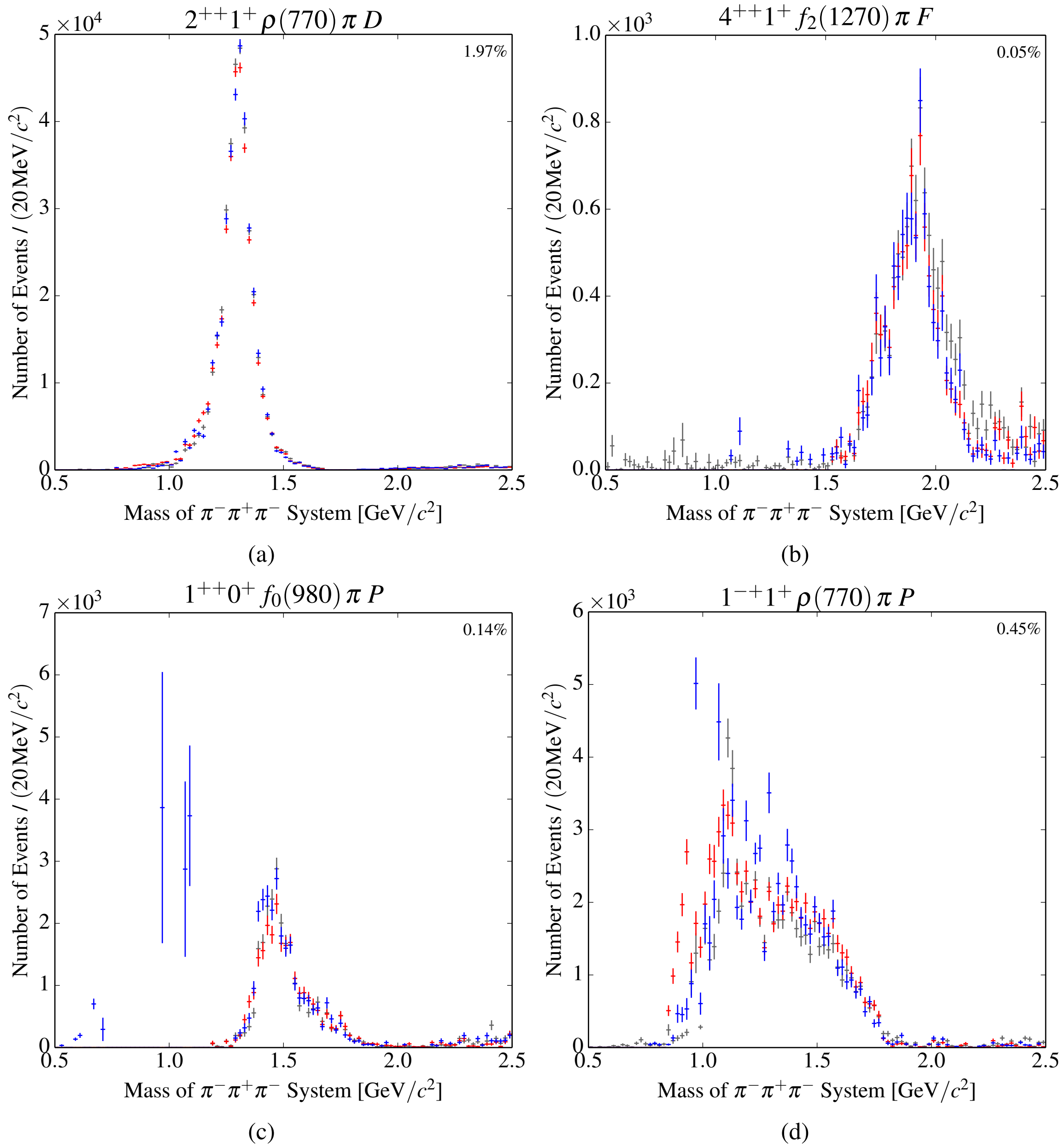

Figure 4.12: Intensity plots for four waves that were well studied in previous analyses.

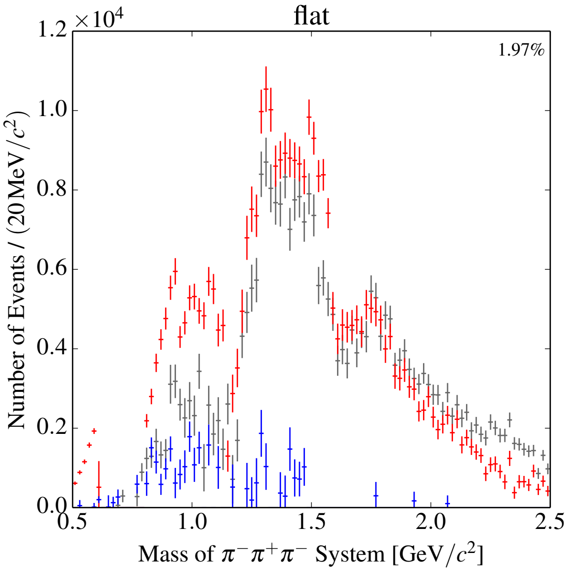

Figure 4.13: Intensity of the incoherent isotropic wave.

Especially in figures 4.12b and 4.12c, some fluctuations below threshold are removed. In figure 4.12d, an artificial structure in intensity is observed below $1\,\mathrm{GeV}/c^2$ with the combined wave set. This behaviour is probably caused by the low-mass fluctuations, which cannot completely be diminished with the threshold algorithm.

Figure 4.14 highlights the improvement in the low-mass region caused by the introduction of thresholds. It shows two 0^{-+} waves, that exhibit large differences of the final fit compared to the reference fit. In figure 4.14a, the fluctuations below $1.2\,\mathrm{GeV}/c^2$ are removed by imposing a threshold on the wave. Figure 4.14b is a more interesting case. Since there is intensity over almost the whole analyzed mass range, the wave is practically not thresholded[6]. But through the interplay with all other waves in interference, the fluctuations below $1.5\,\mathrm{GeV}/c^2$ vanish in the fits with the combined wave set and are now much closer to the reference fits. However, we have only limited indirect proof, that the observed behaviour is physically correct.

In addition to the established waves that are part of the reference wave set, the combined wave set yields some newly found waves. In figure 4.15, the effect of using the combined wave set in the four waves that were presented in figure 4.9 is shown. As we can see, the results remain largely unchanged. While the automated thresholds work very well in figures 4.15a and 4.15b, removing single bins of non-zero intensity in lower masses, they could probably be moved to lower masses in figures 4.15c and 4.15d. Nevertheless, the results of the fit with the combined wave set emphasizes the findings of the final fit, in that these new waves are stable with changing models and are needed to describe the data.

Finally, the intensity of the incoherent isotropic wave is shown in figure 4.13. With the combined wave set, the freedom of the fit is more restricted than with the final fit and therefore the fit result resembles more that of the reference fit. Interestingly, there is more intensity in the low-mass region,

[6] The required ten consecutive bins with intensity start at approximately $0.6\,\mathrm{GeV}/c^2$

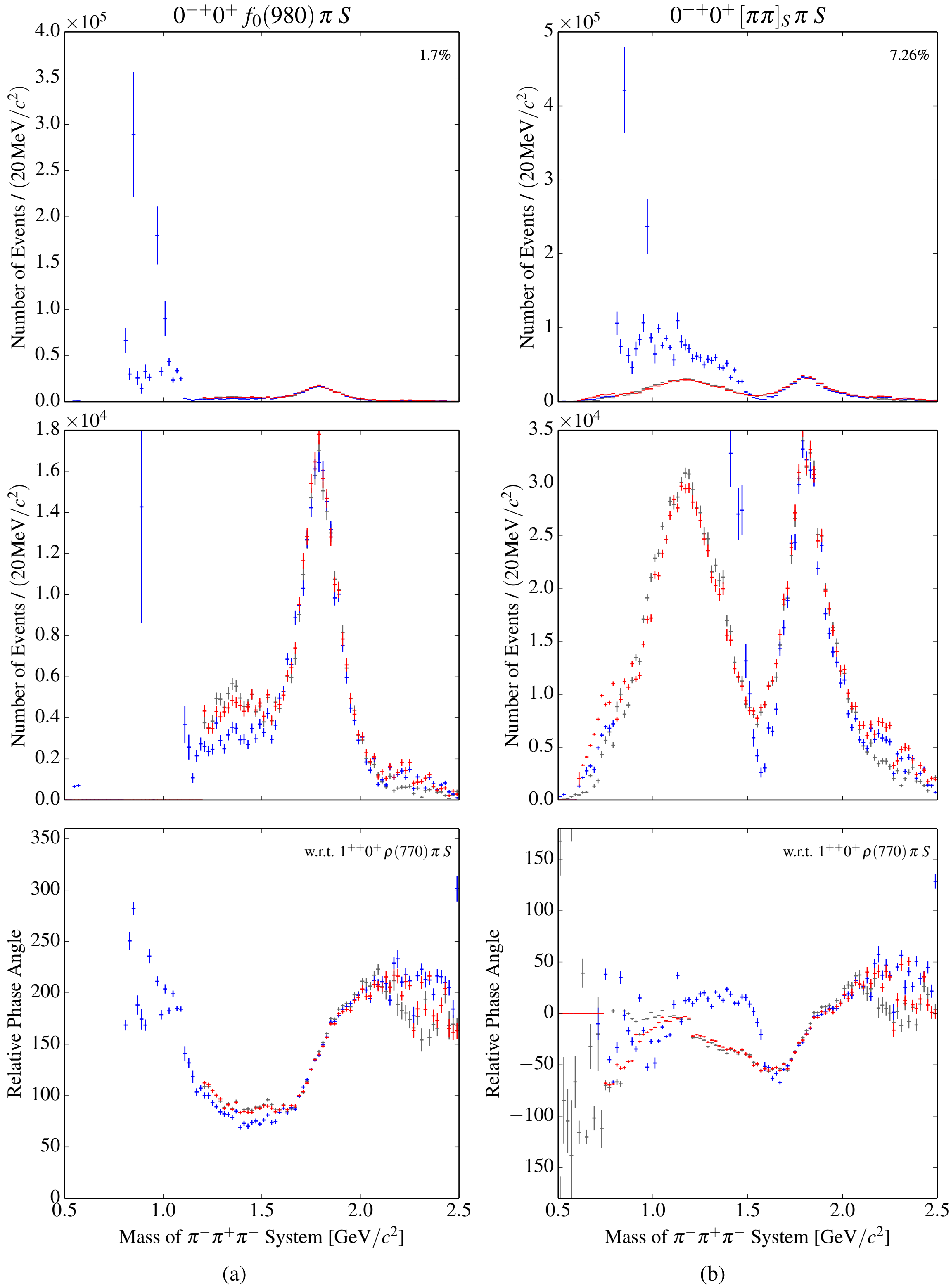

Figure 4.14: The two 0^{-+} waves. The plots in the middle row are zoomed versions of the intensity plots in the top row.

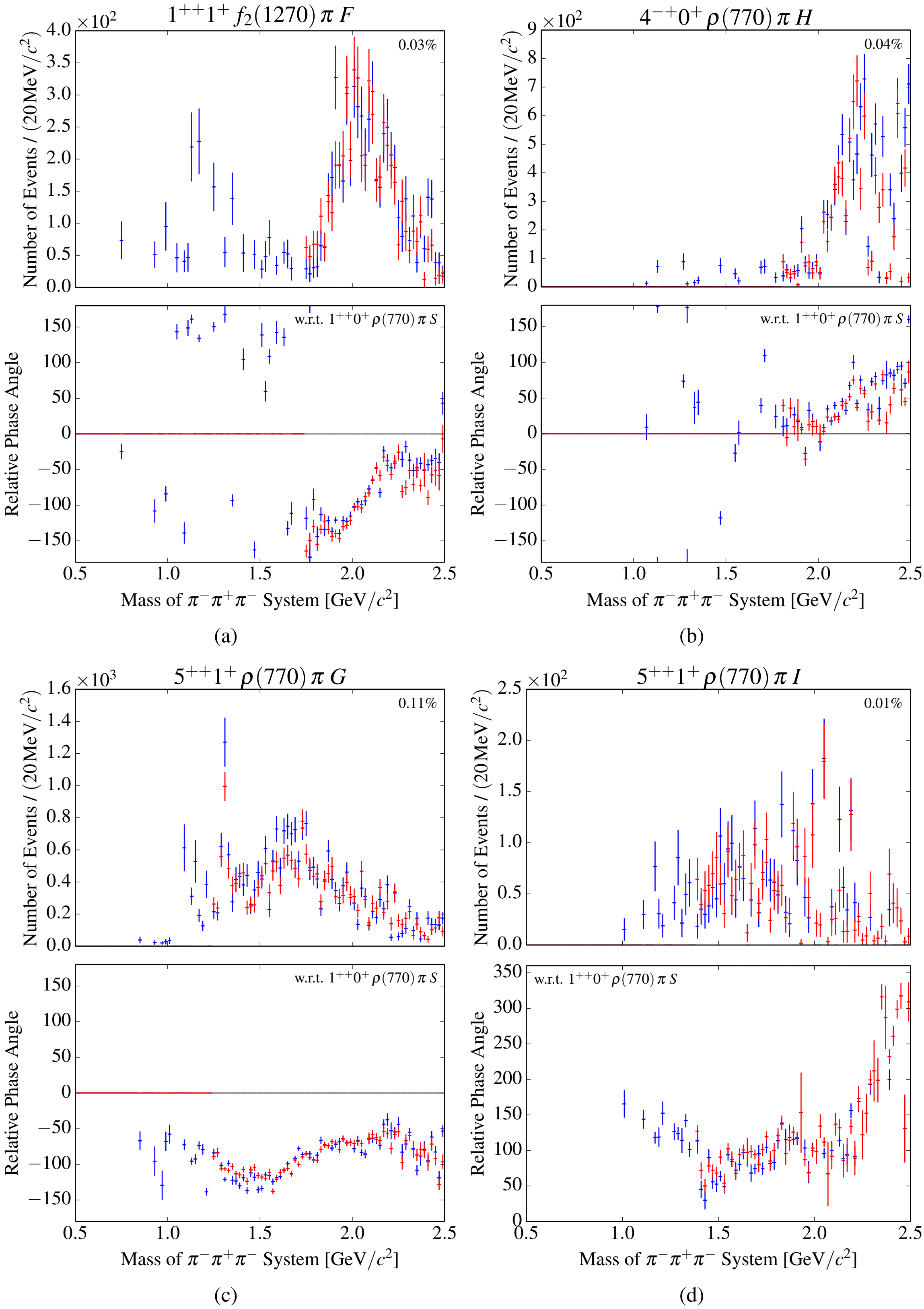

Figure 4.15: Four examples of newly found waves by the model selection procedure.

while in the high-mass region less intensity is observed for the combined wave set than for the reference wave set. The increased intensity in the low-mass region is likely explained by the threshold algorithm, which tends to implement higher thresholds than needed, leading to very small wave sets at low masses. At high masses some of the newly found high-spin waves take up some intensity that was part of the incoherent isotropic wave in the reference fit.

CHAPTER 5

Conclusions and Outlook

Past partial-wave analyses of the charged three-pion channel have used complicated and extensive systematic studies to find a stable wave set that describes the data well. The goal of this analysis was to determine if it were possible to retrieve a wave set suitable to the data based on an algorithm, without the effort of hand-selecting it, therefore removing the observer bias. This algorithm can also be used to assess the validity of the reference wave set used in previous analyses of this channel [3, 5]. As these studies only serve as a proof-of-concept, the analysis was limited to the lowest t' bin.

Before discussing the conclusions of the model selection, this thesis revealed that the approximation of Gaussianity close to the likelihood maximum is poor. A method that better approximates the uncertainties of the fit parameters has to be found. A possible solution would be to use Markov chain Monte Carlo methods to approximate the probability density function of the likelihood function. This would provide the information needed to calculate the uncertainties and correlations of fit parameters.

In order to achieve the set goals of this thesis, a new model-selection procedure was studied. It is based on a large wave set called wave pool, which contains possible quantum numbers of resonances and their decay modes for this reaction up to conservatively chosen cut-off parameters. Since the wave pool includes all conceivably contributing waves, not much prior knowledge is needed to construct it. The procedure fits the wave pool to the data, while forcing small waves to have no intensity by implementing a half-Cauchy prior function, thus eliminating unneeded waves. The fits of the wave pool were performed independently in each bin of final-state mass and based on their result a different wave set was found for each mass bin.

These new wave sets were then fit to the data to produce the first set of results. Because the model selection did not include a continuity constraint, the wave sets were different in each bin and some fluctuations from one bin to the next were observed. Still, the shapes of both, intensity distributions and phase differences of all important waves were reasonably reproduced compared to fits with the reference wave set. Additionally, some new waves, that have never been investigated previously, showed structures. In turn, some low-intensity waves from the reference wave set could not be confirmed in the results of the model selection. A caveat of the model-selection procedure is that it produces fluctuations in the form of unphysically large destructive interference in the lower parts of the mass spectrum, deviating from the reference fits. These problems were observed in previous analyses as well, and were resolved by including certain waves to the wave set only above an $m_{3\pi}$ threshold.

Since having a different wave set in every bin was unphysical, the goal of the second part of the analysis was to create a combined wave set that, apart from thresholds, is continuous in mass. It should be able to replicate the structures from the model-selection results, while simultaneously removing the artifacts caused by the differences of the wave sets in each bin. This analysis step applies physical constraints similar to those used when hand-picking the wave set. Continuity in the intensity distribution was used as an indicator that a wave actually is required by the data, because continuity was not explicitly required by the model selection, but was rather the product of it. Therefore, the condition for a wave to be accepted into the combined wave set was to have non-zero intensity in at least ten consecutive bins.

By enforcing this simple rule a wave set of 118 waves was formed. It included 72 of the 88 waves from the reference wave set. The 16 waves that were not found included all seven waves of the reference wave set with negative reflectivity. For those the model selection found better alternatives. Since the negative-reflectivity sector was not well explored in previous analyses, this was not a surprising result and should be studied in more detail in the future. Furthermore, 46 additional waves, which were not in the reference wave set, were found in the combined wave set, some of which seem to have interesting features. Most of them are high-spin waves, which indicates that the low-spin waves have been thoroughly explored in the selection of the reference wave set.

Due to the unphysically large destructive interference effects in the low-mass region of many waves, a way to threshold critical waves had to be implemented. Since doing this by hand was not an option, a rule to threshold each wave had to be constructed. The threshold for each wave was set below the bin that marked the start of the first ten consecutive bins with non-zero intensity in that wave. This ensured that the important features of the waves were still present in the fits with the combined wave set, while the low-mass region was stabilized as well. Naturally, this automatic approach is not perfect, but as a proof-of-concept it worked sufficiently well for most waves. The few thresholds that were implemented in the reference wave set were transferred to the combined wave set. This was done particularly to fix the $0^{-+}0^{+} f_0(980)\pi S$ wave, which was the only wave that showed continuous intensity (thus fulfilling the ten consecutive bins requirement), even though its erratic intensity behaviour was obviously unphysical. Through interference, this one wave caused several other waves to fluctuate.

Overall, with this systematic approach to model selection the observer bias of previous analyses could be largely removed. The reference wave set used in [3, 5] could be validated, since the features of all important waves could be reproduced with this new model selection method. The differences that were found have no impact on the other waves, since they are small in relative intensity. However, the waves that were discovered by the model selection procedure that are not part of the reference wave set are worth investigating. This is true particularly for the $1^{++}1^{+} f_2(1270)\pi F$ wave, which features a notable peak around $2.2\,\mathrm{GeV}/c^2$ with a clear phase motion in that same region. This would be an interesting candidate to analyze in different bins of t' and maybe even a resonance-model fit could be performed.

Improvements to the analysis procedure have been discussed, but were not in the scope of this thesis. The first obvious step would be to verify the method using Monte-Carlo data. This has already been realized with success in the $\pi^-\pi^+\pi^-\pi^+\pi^-$ final state [7], but should be repeated in the $\pi^-\pi^+\pi^-$ channel. The analysis should also be extended to the full t' range. The biggest challenge in the 3π channel were the fluctuations in the low-mass region, which may be tamed by introducing a second prior that penalizes unphysically large interferences between waves. Another facet that would be worth examining is the effect of the prior width [see equation (3.3)] on the model selection. In this thesis, this parameter was set to $w = 0.5$ based on a simple study in the charged five-pion channel [19], but an in-depth study is advised. The algorithm used to select the combined wave set as well as the method to choose thresholds for waves are very simple. Additional criteria could further improve the results.

A long term goal would be to create an algorithm that performs model selection fully automated. One could also expand the analysis to other, unfamiliar final states (i.e. $\pi^-\eta\eta$), where it could facilitate the model selection immensely. It has already been applied to the $\pi^-\pi^+\pi^-\pi^+\pi^-$ final state [7].

APPENDIX A

Partial Waves of the 88 Wave Set

$J^{PC}\,M^{\varepsilon}$	Isobar	L	Threshold [MeV/c^2]	$J^{PC}\,M^{\varepsilon}$	Isobar	L	Threshold [MeV/c^2]
$0^{-+}0^{+}$	$[\pi\pi]_S$	S	–	$0^{-+}0^{+}$	$\rho(770)$	P	–
$0^{-+}0^{+}$	$f_0(1500)$	S	1700	$0^{-+}0^{+}$	$f_0(980)$	S	1200
$0^{-+}0^{+}$	$f_2(1270)$	D	–				
$1^{++}0^{+}$	$[\pi\pi]_S$	P	–	$1^{++}0^{+}$	$\rho(770)$	D	–
$1^{++}0^{+}$	$\rho(770)$	S	–	$1^{++}0^{+}$	$\rho_3(1690)$	D	–
$1^{++}0^{+}$	$\rho_3(1690)$	G	–	$1^{++}0^{+}$	$f_0(980)$	P	1180
$1^{++}0^{+}$	$f_2(1270)$	F	–	$1^{++}0^{+}$	$f_2(1270)$	P	1220
$1^{++}1^{+}$	$[\pi\pi]_S$	P	1100	$1^{++}1^{+}$	$\rho(770)$	D	–
$1^{++}1^{+}$	$\rho(770)$	S	–	$1^{++}1^{+}$	$f_0(980)$	P	1140
$1^{++}1^{+}$	$f_2(1270)$	P	–				
$1^{-+}1^{+}$	$\rho(770)$	P	–				
$2^{++}1^{+}$	$\rho(770)$	D	–	$2^{++}1^{+}$	$\rho_3(1690)$	D	800
$2^{++}1^{+}$	$f_2(1270)$	P	1000	$2^{++}2^{+}$	$\rho(770)$	D	–
$2^{++}2^{+}$	$f_2(1270)$	P	1400				
$2^{-+}0^{+}$	$[\pi\pi]_S$	D	–	$2^{-+}0^{+}$	$\rho(770)$	F	–
$2^{-+}0^{+}$	$\rho(770)$	P	–	$2^{-+}0^{+}$	$\rho_3(1690)$	P	1000
$2^{-+}0^{+}$	$f_0(980)$	D	1160	$2^{-+}0^{+}$	$f_2(1270)$	D	–
$2^{-+}0^{+}$	$f_2(1270)$	G	–	$2^{-+}0^{+}$	$f_2(1270)$	S	–
$2^{-+}1^{+}$	$[\pi\pi]_S$	D	–	$2^{-+}1^{+}$	$\rho(770)$	F	–
$2^{-+}1^{+}$	$\rho(770)$	P	–	$2^{-+}1^{+}$	$\rho_3(1690)$	P	1300
$2^{-+}1^{+}$	$f_2(1270)$	D	–	$2^{-+}1^{+}$	$f_2(1270)$	S	1100
$2^{-+}2^{+}$	$\rho(770)$	P	–	$2^{-+}2^{+}$	$f_2(1270)$	D	–
$2^{-+}2^{+}$	$f_2(1270)$	S	–				
$3^{++}0^{+}$	$[\pi\pi]_S$	F	–	$3^{++}0^{+}$	$\rho(770)$	D	–
$3^{++}0^{+}$	$\rho(770)$	G	–	$3^{++}0^{+}$	$\rho_3(1690)$	I	–
$3^{++}0^{+}$	$\rho_3(1690)$	S	1380	$3^{++}0^{+}$	$f_2(1270)$	P	960
$3^{++}1^{+}$	$[\pi\pi]_S$	F	–	$3^{++}1^{+}$	$\rho(770)$	D	–
$3^{++}1^{+}$	$\rho(770)$	G	–	$3^{++}1^{+}$	$\rho_3(1690)$	S	1380

$J^{PC}\ M^{\varepsilon}$	**Isobar**	**L**	**Threshold** [MeV/c^2]	$J^{PC}\ M^{\varepsilon}$	**Isobar**	**L**	**Threshold** [MeV/c^2]
$3^{++}1^{+}$	$f_2(1270)$	P	1140				
$3^{-+}1^{+}$	$\rho(770)$	F	–	$3^{-+}1^{+}$	$f_2(1270)$	D	1340
$4^{++}1^{+}$	$\rho(770)$	G	–	$4^{++}1^{+}$	$\rho_3(1690)$	D	1700
$4^{++}1^{+}$	$f_2(1270)$	F	–	$4^{++}2^{+}$	$\rho(770)$	G	–
$4^{++}2^{+}$	$f_2(1270)$	F	–				
$4^{-+}0^{+}$	$[\pi\pi]_S$	G	1400	$4^{-+}0^{+}$	$\rho(770)$	F	–
$4^{-+}0^{+}$	$f_2(1270)$	D	–	$4^{-+}0^{+}$	$f_2(1270)$	G	1600
$4^{-+}1^{+}$	$\rho(770)$	F	–	$4^{-+}1^{+}$	$f_2(1270)$	D	–
$5^{++}0^{+}$	$[\pi\pi]_S$	H	–	$5^{++}0^{+}$	$\rho(770)$	G	–
$5^{++}0^{+}$	$\rho_3(1690)$	D	1360	$5^{++}0^{+}$	$f_2(1270)$	F	980
$5^{++}0^{+}$	$f_2(1270)$	H	–	$5^{++}1^{+}$	$[\pi\pi]_S$	H	–
$5^{++}1^{+}$	$f_2(1270)$	F	–				
$6^{++}1^{+}$	$\rho(770)$	I	–	$6^{++}1^{+}$	$f_2(1270)$	H	–
$6^{-+}0^{+}$	$[\pi\pi]_S$	I	–	$6^{-+}0^{+}$	$\rho(770)$	H	–
$6^{-+}0^{+}$	$\rho_3(1690)$	F	–	$6^{-+}0^{+}$	$f_2(1270)$	G	–
$6^{-+}1^{+}$	$[\pi\pi]_S$	I	–	$6^{-+}1^{+}$	$\rho(770)$	H	–
$1^{++}1^{-}$	$\rho(770)$	S	–				
$1^{-+}0^{-}$	$\rho(770)$	P	–	$1^{-+}1^{-}$	$\rho(770)$	P	–
$2^{++}0^{-}$	$\rho(770)$	D	–	$2^{++}0^{-}$	$f_2(1270)$	P	1180
$2^{++}1^{-}$	$f_2(1270)$	P	1300				
$2^{-+}1^{-}$	$f_2(1270)$	S	–				

APPENDIX B

Partial Waves of the Wave Pool

$J^{PC}\ M^{\varepsilon}$	Isobar	L	$J^{PC}\ M^{\varepsilon}$	Isobar	L
$0^{-+}0^{+}$	$[\pi\pi]_S$	S	$0^{-+}0^{+}$	$\rho(770)$	P
$0^{-+}0^{+}$	$\rho_3(1690)$	F	$0^{-+}0^{+}$	$f_0(1500)$	S
$0^{-+}0^{+}$	$f_0(980)$	S	$0^{-+}0^{+}$	$f_2(1270)$	D
$1^{++}0^{+}$	$[\pi\pi]_S$	P	$1^{++}0^{+}$	$\rho(770)$	D
$1^{++}0^{+}$	$\rho(770)$	S	$1^{++}0^{+}$	$\rho_3(1690)$	D
$1^{++}0^{+}$	$\rho_3(1690)$	G	$1^{++}0^{+}$	$f_0(1500)$	P
$1^{++}0^{+}$	$f_0(980)$	P	$1^{++}0^{+}$	$f_2(1270)$	F
$1^{++}0^{+}$	$f_2(1270)$	P	$1^{++}1^{+}$	$[\pi\pi]_S$	P
$1^{++}1^{+}$	$\rho(770)$	D	$1^{++}1^{+}$	$\rho(770)$	S
$1^{++}1^{+}$	$\rho_3(1690)$	D	$1^{++}1^{+}$	$\rho_3(1690)$	G
$1^{++}1^{+}$	$f_0(1500)$	P	$1^{++}1^{+}$	$f_0(980)$	P
$1^{++}1^{+}$	$f_2(1270)$	F	$1^{++}1^{+}$	$f_2(1270)$	P
$1^{-+}1^{+}$	$\rho(770)$	P	$1^{-+}1^{+}$	$\rho_3(1690)$	F
$1^{-+}1^{+}$	$f_2(1270)$	D			
$2^{++}1^{+}$	$\rho(770)$	D	$2^{++}1^{+}$	$\rho_3(1690)$	D
$2^{++}1^{+}$	$\rho_3(1690)$	G	$2^{++}1^{+}$	$f_2(1270)$	F
$2^{++}1^{+}$	$f_2(1270)$	P	$2^{++}2^{+}$	$\rho(770)$	D
$2^{++}2^{+}$	$\rho_3(1690)$	D	$2^{++}2^{+}$	$\rho_3(1690)$	G
$2^{++}2^{+}$	$f_2(1270)$	F	$2^{++}2^{+}$	$f_2(1270)$	P
$2^{-+}0^{+}$	$[\pi\pi]_S$	D	$2^{-+}0^{+}$	$\rho(770)$	F
$2^{-+}0^{+}$	$\rho(770)$	P	$2^{-+}0^{+}$	$\rho_3(1690)$	F
$2^{-+}0^{+}$	$\rho_3(1690)$	H	$2^{-+}0^{+}$	$\rho_3(1690)$	P
$2^{-+}0^{+}$	$f_0(1500)$	D	$2^{-+}0^{+}$	$f_0(980)$	D
$2^{-+}0^{+}$	$f_2(1270)$	D	$2^{-+}0^{+}$	$f_2(1270)$	G
$2^{-+}0^{+}$	$f_2(1270)$	S	$2^{-+}1^{+}$	$[\pi\pi]_S$	D
$2^{-+}1^{+}$	$\rho(770)$	F	$2^{-+}1^{+}$	$\rho(770)$	P
$2^{-+}1^{+}$	$\rho_3(1690)$	F	$2^{-+}1^{+}$	$\rho_3(1690)$	H
$2^{-+}1^{+}$	$\rho_3(1690)$	P	$2^{-+}1^{+}$	$f_0(1500)$	D
$2^{-+}1^{+}$	$f_0(980)$	D	$2^{-+}1^{+}$	$f_2(1270)$	D
$2^{-+}1^{+}$	$f_2(1270)$	G	$2^{-+}1^{+}$	$f_2(1270)$	S

$J^{PC}\,M^{\varepsilon}$	Isobar	L	$J^{PC}\,M^{\varepsilon}$	Isobar	L
$2^{-+}2^{+}$	$[\pi\pi]_S$	D	$2^{-+}2^{+}$	$\rho(770)$	F
$2^{-+}2^{+}$	$\rho(770)$	P	$2^{-+}2^{+}$	$\rho_3(1690)$	F
$2^{-+}2^{+}$	$\rho_3(1690)$	H	$2^{-+}2^{+}$	$\rho_3(1690)$	P
$2^{-+}2^{+}$	$f_0(1500)$	D	$2^{-+}2^{+}$	$f_0(980)$	D
$2^{-+}2^{+}$	$f_2(1270)$	D	$2^{-+}2^{+}$	$f_2(1270)$	G
$2^{-+}2^{+}$	$f_2(1270)$	S			
$3^{++}0^{+}$	$[\pi\pi]_S$	F	$3^{++}0^{+}$	$\rho(770)$	D
$3^{++}0^{+}$	$\rho(770)$	G	$3^{++}0^{+}$	$\rho_3(1690)$	D
$3^{++}0^{+}$	$\rho_3(1690)$	G	$3^{++}0^{+}$	$\rho_3(1690)$	I
$3^{++}0^{+}$	$\rho_3(1690)$	S	$3^{++}0^{+}$	$f_0(1500)$	F
$3^{++}0^{+}$	$f_0(980)$	F	$3^{++}0^{+}$	$f_2(1270)$	F
$3^{++}0^{+}$	$f_2(1270)$	H	$3^{++}0^{+}$	$f_2(1270)$	P
$3^{++}1^{+}$	$[\pi\pi]_S$	F	$3^{++}1^{+}$	$\rho(770)$	D
$3^{++}1^{+}$	$\rho(770)$	G	$3^{++}1^{+}$	$\rho_3(1690)$	D
$3^{++}1^{+}$	$\rho_3(1690)$	G	$3^{++}1^{+}$	$\rho_3(1690)$	I
$3^{++}1^{+}$	$\rho_3(1690)$	S	$3^{++}1^{+}$	$f_0(1500)$	F
$3^{++}1^{+}$	$f_0(980)$	F	$3^{++}1^{+}$	$f_2(1270)$	F
$3^{++}1^{+}$	$f_2(1270)$	H	$3^{++}1^{+}$	$f_2(1270)$	P
$3^{++}2^{+}$	$[\pi\pi]_S$	F	$3^{++}2^{+}$	$\rho(770)$	D
$3^{++}2^{+}$	$\rho(770)$	G	$3^{++}2^{+}$	$\rho_3(1690)$	D
$3^{++}2^{+}$	$\rho_3(1690)$	G	$3^{++}2^{+}$	$\rho_3(1690)$	I
$3^{++}2^{+}$	$\rho_3(1690)$	S	$3^{++}2^{+}$	$f_0(1500)$	F
$3^{++}2^{+}$	$f_0(980)$	F	$3^{++}2^{+}$	$f_2(1270)$	F
$3^{++}2^{+}$	$f_2(1270)$	H	$3^{++}2^{+}$	$f_2(1270)$	P
$3^{-+}1^{+}$	$\rho(770)$	F	$3^{-+}1^{+}$	$\rho_3(1690)$	F
$3^{-+}1^{+}$	$\rho_3(1690)$	H	$3^{-+}1^{+}$	$\rho_3(1690)$	P
$3^{-+}1^{+}$	$f_2(1270)$	D	$3^{-+}1^{+}$	$f_2(1270)$	G
$3^{-+}2^{+}$	$\rho(770)$	F	$3^{-+}2^{+}$	$\rho_3(1690)$	F
$3^{-+}2^{+}$	$\rho_3(1690)$	H	$3^{-+}2^{+}$	$\rho_3(1690)$	P
$3^{-+}2^{+}$	$f_2(1270)$	D	$3^{-+}2^{+}$	$f_2(1270)$	G
$4^{++}1^{+}$	$\rho(770)$	G	$4^{++}1^{+}$	$\rho_3(1690)$	D
$4^{++}1^{+}$	$\rho_3(1690)$	G	$4^{++}1^{+}$	$\rho_3(1690)$	I
$4^{++}1^{+}$	$f_2(1270)$	F	$4^{++}1^{+}$	$f_2(1270)$	H
$4^{++}2^{+}$	$\rho(770)$	G	$4^{++}2^{+}$	$\rho_3(1690)$	D
$4^{++}2^{+}$	$\rho_3(1690)$	G	$4^{++}2^{+}$	$\rho_3(1690)$	I
$4^{++}2^{+}$	$f_2(1270)$	F	$4^{++}2^{+}$	$f_2(1270)$	H
$4^{-+}0^{+}$	$[\pi\pi]_S$	G	$4^{-+}0^{+}$	$\rho(770)$	F
$4^{-+}0^{+}$	$\rho(770)$	H	$4^{-+}0^{+}$	$\rho_3(1690)$	F
$4^{-+}0^{+}$	$\rho_3(1690)$	H	$4^{-+}0^{+}$	$\rho_3(1690)$	P
$4^{-+}0^{+}$	$f_0(1500)$	G	$4^{-+}0^{+}$	$f_0(980)$	G
$4^{-+}0^{+}$	$f_2(1270)$	D	$4^{-+}0^{+}$	$f_2(1270)$	G
$4^{-+}0^{+}$	$f_2(1270)$	I	$4^{-+}1^{+}$	$[\pi\pi]_S$	G
$4^{-+}1^{+}$	$\rho(770)$	F	$4^{-+}1^{+}$	$\rho(770)$	H

J^{PC} M^{ε}	Isobar	L	J^{PC} M^{ε}	Isobar	L
$4^{-+}1^{+}$	$\rho_3(1690)$	F	$4^{-+}1^{+}$	$\rho_3(1690)$	H
$4^{-+}1^{+}$	$\rho_3(1690)$	P	$4^{-+}1^{+}$	$f_0(1500)$	G
$4^{-+}1^{+}$	$f_0(980)$	G	$4^{-+}1^{+}$	$f_2(1270)$	D
$4^{-+}1^{+}$	$f_2(1270)$	G	$4^{-+}1^{+}$	$f_2(1270)$	I
$4^{-+}2^{+}$	$[\pi\pi]_S$	G	$4^{-+}2^{+}$	$\rho(770)$	F
$4^{-+}2^{+}$	$\rho(770)$	H	$4^{-+}2^{+}$	$\rho_3(1690)$	F
$4^{-+}2^{+}$	$\rho_3(1690)$	H	$4^{-+}2^{+}$	$\rho_3(1690)$	P
$4^{-+}2^{+}$	$f_0(1500)$	G	$4^{-+}2^{+}$	$f_0(980)$	G
$4^{-+}2^{+}$	$f_2(1270)$	D	$4^{-+}2^{+}$	$f_2(1270)$	G
$4^{-+}2^{+}$	$f_2(1270)$	I			
$5^{++}0^{+}$	$[\pi\pi]_S$	H	$5^{++}0^{+}$	$\rho(770)$	G
$5^{++}0^{+}$	$\rho(770)$	I	$5^{++}0^{+}$	$\rho_3(1690)$	D
$5^{++}0^{+}$	$\rho_3(1690)$	G	$5^{++}0^{+}$	$\rho_3(1690)$	I
$5^{++}0^{+}$	$f_0(1500)$	H	$5^{++}0^{+}$	$f_0(980)$	H
$5^{++}0^{+}$	$f_2(1270)$	F	$5^{++}0^{+}$	$f_2(1270)$	H
$5^{++}1^{+}$	$[\pi\pi]_S$	H	$5^{++}1^{+}$	$\rho(770)$	G
$5^{++}1^{+}$	$\rho(770)$	I	$5^{++}1^{+}$	$\rho_3(1690)$	D
$5^{++}1^{+}$	$\rho_3(1690)$	G	$5^{++}1^{+}$	$\rho_3(1690)$	I
$5^{++}1^{+}$	$f_0(1500)$	H	$5^{++}1^{+}$	$f_0(980)$	H
$5^{++}1^{+}$	$f_2(1270)$	F	$5^{++}1^{+}$	$f_2(1270)$	H
$5^{++}2^{+}$	$[\pi\pi]_S$	H	$5^{++}2^{+}$	$\rho(770)$	G
$5^{++}2^{+}$	$\rho(770)$	I	$5^{++}2^{+}$	$\rho_3(1690)$	D
$5^{++}2^{+}$	$\rho_3(1690)$	G	$5^{++}2^{+}$	$\rho_3(1690)$	I
$5^{++}2^{+}$	$f_0(1500)$	H	$5^{++}2^{+}$	$f_0(980)$	H
$5^{++}2^{+}$	$f_2(1270)$	F	$5^{++}2^{+}$	$f_2(1270)$	H
$5^{-+}1^{+}$	$\rho(770)$	H	$5^{-+}1^{+}$	$\rho_3(1690)$	F
$5^{-+}1^{+}$	$\rho_3(1690)$	H	$5^{-+}1^{+}$	$f_2(1270)$	G
$5^{-+}1^{+}$	$f_2(1270)$	I	$5^{-+}2^{+}$	$\rho(770)$	H
$5^{-+}2^{+}$	$\rho_3(1690)$	F	$5^{-+}2^{+}$	$\rho_3(1690)$	H
$5^{-+}2^{+}$	$f_2(1270)$	G	$5^{-+}2^{+}$	$f_2(1270)$	I
$6^{++}1^{+}$	$\rho(770)$	I	$6^{++}1^{+}$	$\rho_3(1690)$	G
$6^{++}1^{+}$	$\rho_3(1690)$	I	$6^{++}1^{+}$	$f_2(1270)$	H
$6^{++}2^{+}$	$\rho(770)$	I	$6^{++}2^{+}$	$\rho_3(1690)$	G
$6^{++}2^{+}$	$\rho_3(1690)$	I	$6^{++}2^{+}$	$f_2(1270)$	H
$6^{-+}0^{+}$	$[\pi\pi]_S$	I	$6^{-+}0^{+}$	$\rho(770)$	H
$6^{-+}0^{+}$	$\rho_3(1690)$	F	$6^{-+}0^{+}$	$\rho_3(1690)$	H
$6^{-+}0^{+}$	$f_0(1500)$	I	$6^{-+}0^{+}$	$f_0(980)$	I
$6^{-+}0^{+}$	$f_2(1270)$	G	$6^{-+}0^{+}$	$f_2(1270)$	I
$6^{-+}1^{+}$	$[\pi\pi]_S$	I	$6^{-+}1^{+}$	$\rho(770)$	H
$6^{-+}1^{+}$	$\rho_3(1690)$	F	$6^{-+}1^{+}$	$\rho_3(1690)$	H
$6^{-+}1^{+}$	$f_0(1500)$	I	$6^{-+}1^{+}$	$f_0(980)$	I
$6^{-+}1^{+}$	$f_2(1270)$	G	$6^{-+}1^{+}$	$f_2(1270)$	I
$6^{-+}2^{+}$	$[\pi\pi]_S$	I	$6^{-+}2^{+}$	$\rho(770)$	H

$J^{PC}\ M^{\varepsilon}$	Isobar	L	$J^{PC}\ M^{\varepsilon}$	Isobar	L
$6^{-+}2^{+}$	$\rho_3(1690)$	F	$6^{-+}2^{+}$	$\rho_3(1690)$	H
$6^{-+}2^{+}$	$f_0(1500)$	I	$6^{-+}2^{+}$	$f_0(980)$	I
$6^{-+}2^{+}$	$f_2(1270)$	G	$6^{-+}2^{+}$	$f_2(1270)$	I
$1^{++}1^{-}$	$[\pi\pi]_S$	P	$1^{++}1^{-}$	$\rho(770)$	D
$1^{++}1^{-}$	$\rho(770)$	S	$1^{++}1^{-}$	$\rho_3(1690)$	D
$1^{++}1^{-}$	$\rho_3(1690)$	G	$1^{++}1^{-}$	$f_0(1500)$	P
$1^{++}1^{-}$	$f_0(980)$	P	$1^{++}1^{-}$	$f_2(1270)$	F
$1^{++}1^{-}$	$f_2(1270)$	P			
$1^{-+}0^{-}$	$\rho(770)$	P	$1^{-+}0^{-}$	$\rho_3(1690)$	F
$1^{-+}0^{-}$	$f_2(1270)$	D	$1^{-+}1^{-}$	$\rho(770)$	P
$1^{-+}1^{-}$	$\rho_3(1690)$	F	$1^{-+}1^{-}$	$f_2(1270)$	D
$2^{++}0^{-}$	$\rho(770)$	D	$2^{++}0^{-}$	$\rho_3(1690)$	D
$2^{++}0^{-}$	$\rho_3(1690)$	G	$2^{++}0^{-}$	$f_2(1270)$	F
$2^{++}0^{-}$	$f_2(1270)$	P	$2^{++}1^{-}$	$\rho(770)$	D
$2^{++}1^{-}$	$\rho_3(1690)$	D	$2^{++}1^{-}$	$\rho_3(1690)$	G
$2^{++}1^{-}$	$f_2(1270)$	F	$2^{++}1^{-}$	$f_2(1270)$	P
$2^{++}2^{-}$	$\rho(770)$	D	$2^{++}2^{-}$	$\rho_3(1690)$	D
$2^{++}2^{-}$	$\rho_3(1690)$	G	$2^{++}2^{-}$	$f_2(1270)$	F
$2^{++}2^{-}$	$f_2(1270)$	P			
$2^{-+}1^{-}$	$[\pi\pi]_S$	D	$2^{-+}1^{-}$	$\rho(770)$	F
$2^{-+}1^{-}$	$\rho(770)$	P	$2^{-+}1^{-}$	$\rho_3(1690)$	F
$2^{-+}1^{-}$	$\rho_3(1690)$	H	$2^{-+}1^{-}$	$\rho_3(1690)$	P
$2^{-+}1^{-}$	$f_0(1500)$	D	$2^{-+}1^{-}$	$f_0(980)$	D
$2^{-+}1^{-}$	$f_2(1270)$	D	$2^{-+}1^{-}$	$f_2(1270)$	G
$2^{-+}1^{-}$	$f_2(1270)$	S	$2^{-+}2^{-}$	$[\pi\pi]_S$	D
$2^{-+}2^{-}$	$\rho(770)$	F	$2^{-+}2^{-}$	$\rho(770)$	P
$2^{-+}2^{-}$	$\rho_3(1690)$	F	$2^{-+}2^{-}$	$\rho_3(1690)$	H
$2^{-+}2^{-}$	$\rho_3(1690)$	P	$2^{-+}2^{-}$	$f_0(1500)$	D
$2^{-+}2^{-}$	$f_0(980)$	D	$2^{-+}2^{-}$	$f_2(1270)$	D
$2^{-+}2^{-}$	$f_2(1270)$	G	$2^{-+}2^{-}$	$f_2(1270)$	S
$3^{++}1^{-}$	$[\pi\pi]_S$	F	$3^{++}1^{-}$	$\rho(770)$	D
$3^{++}1^{-}$	$\rho(770)$	G	$3^{++}1^{-}$	$\rho_3(1690)$	D
$3^{++}1^{-}$	$\rho_3(1690)$	G	$3^{++}1^{-}$	$\rho_3(1690)$	I
$3^{++}1^{-}$	$\rho_3(1690)$	S	$3^{++}1^{-}$	$f_0(1500)$	F
$3^{++}1^{-}$	$f_0(980)$	F	$3^{++}1^{-}$	$f_2(1270)$	F
$3^{++}1^{-}$	$f_2(1270)$	H	$3^{++}1^{-}$	$f_2(1270)$	P
$3^{++}2^{-}$	$[\pi\pi]_S$	F	$3^{++}2^{-}$	$\rho(770)$	D
$3^{++}2^{-}$	$\rho(770)$	G	$3^{++}2^{-}$	$\rho_3(1690)$	D
$3^{++}2^{-}$	$\rho_3(1690)$	G	$3^{++}2^{-}$	$\rho_3(1690)$	I
$3^{++}2^{-}$	$\rho_3(1690)$	S	$3^{++}2^{-}$	$f_0(1500)$	F
$3^{++}2^{-}$	$f_0(980)$	F	$3^{++}2^{-}$	$f_2(1270)$	F
$3^{++}2^{-}$	$f_2(1270)$	H	$3^{++}2^{-}$	$f_2(1270)$	P

$J^{PC}\,M^{\varepsilon}$	Isobar	L	$J^{PC}\,M^{\varepsilon}$	Isobar	L
$3^{-+}0^{-}$	$\rho(770)$	F	$3^{-+}0^{-}$	$\rho_3(1690)$	F
$3^{-+}0^{-}$	$\rho_3(1690)$	H	$3^{-+}0^{-}$	$\rho_3(1690)$	P
$3^{-+}0^{-}$	$f_2(1270)$	D	$3^{-+}0^{-}$	$f_2(1270)$	G
$3^{-+}1^{-}$	$\rho(770)$	F	$3^{-+}1^{-}$	$\rho_3(1690)$	F
$3^{-+}1^{-}$	$\rho_3(1690)$	H	$3^{-+}1^{-}$	$\rho_3(1690)$	P
$3^{-+}1^{-}$	$f_2(1270)$	D	$3^{-+}1^{-}$	$f_2(1270)$	G
$3^{-+}2^{-}$	$\rho(770)$	F	$3^{-+}2^{-}$	$\rho_3(1690)$	F
$3^{-+}2^{-}$	$\rho_3(1690)$	H	$3^{-+}2^{-}$	$\rho_3(1690)$	P
$3^{-+}2^{-}$	$f_2(1270)$	D	$3^{-+}2^{-}$	$f_2(1270)$	G
$4^{++}0^{-}$	$\rho(770)$	G	$4^{++}0^{-}$	$\rho_3(1690)$	D
$4^{++}0^{-}$	$\rho_3(1690)$	G	$4^{++}0^{-}$	$\rho_3(1690)$	I
$4^{++}0^{-}$	$f_2(1270)$	F	$4^{++}0^{-}$	$f_2(1270)$	H
$4^{++}1^{-}$	$\rho(770)$	G	$4^{++}1^{-}$	$\rho_3(1690)$	D
$4^{++}1^{-}$	$\rho_3(1690)$	G	$4^{++}1^{-}$	$\rho_3(1690)$	I
$4^{++}1^{-}$	$f_2(1270)$	F	$4^{++}1^{-}$	$f_2(1270)$	H
$4^{++}2^{-}$	$\rho(770)$	G	$4^{++}2^{-}$	$\rho_3(1690)$	D
$4^{++}2^{-}$	$\rho_3(1690)$	G	$4^{++}2^{-}$	$\rho_3(1690)$	I
$4^{++}2^{-}$	$f_2(1270)$	F	$4^{++}2^{-}$	$f_2(1270)$	H
$4^{-+}1^{-}$	$[\pi\pi]_S$	G	$4^{-+}1^{-}$	$\rho(770)$	F
$4^{-+}1^{-}$	$\rho(770)$	H	$4^{-+}1^{-}$	$\rho_3(1690)$	F
$4^{-+}1^{-}$	$\rho_3(1690)$	H	$4^{-+}1^{-}$	$\rho_3(1690)$	P
$4^{-+}1^{-}$	$f_0(1500)$	G	$4^{-+}1^{-}$	$f_0(980)$	G
$4^{-+}1^{-}$	$f_2(1270)$	D	$4^{-+}1^{-}$	$f_2(1270)$	G
$4^{-+}1^{-}$	$f_2(1270)$	I	$4^{-+}2^{-}$	$[\pi\pi]_S$	G
$4^{-+}2^{-}$	$\rho(770)$	F	$4^{-+}2^{-}$	$\rho(770)$	H
$4^{-+}2^{-}$	$\rho_3(1690)$	F	$4^{-+}2^{-}$	$\rho_3(1690)$	H
$4^{-+}2^{-}$	$\rho_3(1690)$	P	$4^{-+}2^{-}$	$f_0(1500)$	G
$4^{-+}2^{-}$	$f_0(980)$	G	$4^{-+}2^{-}$	$f_2(1270)$	D
$4^{-+}2^{-}$	$f_2(1270)$	G	$4^{-+}2^{-}$	$f_2(1270)$	I
$5^{++}1^{-}$	$[\pi\pi]_S$	H	$5^{++}1^{-}$	$\rho(770)$	G
$5^{++}1^{-}$	$\rho(770)$	I	$5^{++}1^{-}$	$\rho_3(1690)$	D
$5^{++}1^{-}$	$\rho_3(1690)$	G	$5^{++}1^{-}$	$\rho_3(1690)$	I
$5^{++}1^{-}$	$f_0(1500)$	H	$5^{++}1^{-}$	$f_0(980)$	H
$5^{++}1^{-}$	$f_2(1270)$	F	$5^{++}1^{-}$	$f_2(1270)$	H
$5^{++}2^{-}$	$[\pi\pi]_S$	H	$5^{++}2^{-}$	$\rho(770)$	G
$5^{++}2^{-}$	$\rho(770)$	I	$5^{++}2^{-}$	$\rho_3(1690)$	D
$5^{++}2^{-}$	$\rho_3(1690)$	G	$5^{++}2^{-}$	$\rho_3(1690)$	I
$5^{++}2^{-}$	$f_0(1500)$	H	$5^{++}2^{-}$	$f_0(980)$	H
$5^{++}2^{-}$	$f_2(1270)$	F	$5^{++}2^{-}$	$f_2(1270)$	H
$5^{-+}0^{-}$	$\rho(770)$	H	$5^{-+}0^{-}$	$\rho_3(1690)$	F
$5^{-+}0^{-}$	$\rho_3(1690)$	H	$5^{-+}0^{-}$	$f_2(1270)$	G
$5^{-+}0^{-}$	$f_2(1270)$	I	$5^{-+}1^{-}$	$\rho(770)$	H
$5^{-+}1^{-}$	$\rho_3(1690)$	F	$5^{-+}1^{-}$	$\rho_3(1690)$	H

$J^{PC}\, M^{\varepsilon}$	Isobar	L	$J^{PC}\, M^{\varepsilon}$	Isobar	L
$5^{-+}1^{-}$	$f_2(1270)$	G	$5^{-+}1^{-}$	$f_2(1270)$	I
$5^{-+}2^{-}$	$\rho(770)$	H	$5^{-+}2^{-}$	$\rho_3(1690)$	F
$5^{-+}2^{-}$	$\rho_3(1690)$	H	$5^{-+}2^{-}$	$f_2(1270)$	G
$5^{-+}2^{-}$	$f_2(1270)$	I			
$6^{++}0^{-}$	$\rho(770)$	I	$6^{++}0^{-}$	$\rho_3(1690)$	G
$6^{++}0^{-}$	$\rho_3(1690)$	I	$6^{++}0^{-}$	$f_2(1270)$	H
$6^{++}1^{-}$	$\rho(770)$	I	$6^{++}1^{-}$	$\rho_3(1690)$	G
$6^{++}1^{-}$	$\rho_3(1690)$	I	$6^{++}1^{-}$	$f_2(1270)$	H
$6^{++}2^{-}$	$\rho(770)$	I	$6^{++}2^{-}$	$\rho_3(1690)$	G
$6^{++}2^{-}$	$\rho_3(1690)$	I	$6^{++}2^{-}$	$f_2(1270)$	H
$6^{-+}1^{-}$	$[\pi\pi]_S$	I	$6^{-+}1^{-}$	$\rho(770)$	H
$6^{-+}1^{-}$	$\rho_3(1690)$	F	$6^{-+}1^{-}$	$\rho_3(1690)$	H
$6^{-+}1^{-}$	$f_0(1500)$	I	$6^{-+}1^{-}$	$f_0(980)$	I
$6^{-+}1^{-}$	$f_2(1270)$	G	$6^{-+}1^{-}$	$f_2(1270)$	I
$6^{-+}2^{-}$	$[\pi\pi]_S$	I	$6^{-+}2^{-}$	$\rho(770)$	H
$6^{-+}2^{-}$	$\rho_3(1690)$	F	$6^{-+}2^{-}$	$\rho_3(1690)$	H
$6^{-+}2^{-}$	$f_0(1500)$	I	$6^{-+}2^{-}$	$f_0(980)$	I
$6^{-+}2^{-}$	$f_2(1270)$	G	$6^{-+}2^{-}$	$f_2(1270)$	I

APPENDIX C

Partial Waves of the Combined Wave Set

$J^{PC}\,M^{\varepsilon}$	Isobar	L	Threshold [MeV/c^2]	$J^{PC}\,M^{\varepsilon}$	Isobar	L	Threshold [MeV/c^2]
$0^{-+}0^{+}$	$[\pi\pi]_S$	S	600	$0^{-+}0^{+}$	$\rho(770)$	P	860
$0^{-+}0^{+}$	$\rho_3(1690)$	F	1980	$0^{-+}0^{+}$	$f_0(1500)$	S	1700
$0^{-+}0^{+}$	$f_0(980)$	S	1200	$0^{-+}0^{+}$	$f_2(1270)$	D	1300
$1^{++}0^{+}$	$[\pi\pi]_S$	P	900	$1^{++}0^{+}$	$\rho(770)$	D	840
$1^{++}0^{+}$	$\rho(770)$	S	740	$1^{++}0^{+}$	$\rho_3(1690)$	D	1020
$1^{++}0^{+}$	$\rho_3(1690)$	G	1020	$1^{++}0^{+}$	$f_0(1500)$	P	920
$1^{++}0^{+}$	$f_0(980)$	P	1180	$1^{++}0^{+}$	$f_2(1270)$	F	1020
$1^{++}0^{+}$	$f_2(1270)$	P	1220	$1^{++}1^{+}$	$[\pi\pi]_S$	P	1100
$1^{++}1^{+}$	$\rho(770)$	D	1020	$1^{++}1^{+}$	$\rho(770)$	S	940
$1^{++}1^{+}$	$f_0(1500)$	P	1020	$1^{++}1^{+}$	$f_0(980)$	P	1140
$1^{++}1^{+}$	$f_2(1270)$	F	1740	$1^{++}1^{+}$	$f_2(1270)$	P	1260
$1^{-+}1^{+}$	$\rho(770)$	P	840	$1^{-+}1^{+}$	$f_2(1270)$	D	1980
$2^{++}1^{+}$	$\rho(770)$	D	760	$2^{++}1^{+}$	$f_2(1270)$	F	1740
$2^{++}1^{+}$	$f_2(1270)$	P	1000	$2^{++}2^{+}$	$\rho(770)$	D	1040
$2^{-+}0^{+}$	$[\pi\pi]_S$	D	1200	$2^{-+}0^{+}$	$\rho(770)$	F	1200
$2^{-+}0^{+}$	$\rho(770)$	P	800	$2^{-+}0^{+}$	$\rho_3(1690)$	F	1600
$2^{-+}0^{+}$	$\rho_3(1690)$	P	1000	$2^{-+}0^{+}$	$f_0(1500)$	D	1180
$2^{-+}0^{+}$	$f_0(980)$	D	1160	$2^{-+}0^{+}$	$f_2(1270)$	D	1540
$2^{-+}0^{+}$	$f_2(1270)$	G	1740	$2^{-+}0^{+}$	$f_2(1270)$	S	1240
$2^{-+}1^{+}$	$[\pi\pi]_S$	D	1640	$2^{-+}1^{+}$	$\rho(770)$	F	1100
$2^{-+}1^{+}$	$\rho(770)$	P	760	$2^{-+}1^{+}$	$\rho_3(1690)$	P	1300
$2^{-+}1^{+}$	$f_0(980)$	D	1320	$2^{-+}1^{+}$	$f_2(1270)$	D	1560
$2^{-+}1^{+}$	$f_2(1270)$	G	1800	$2^{-+}1^{+}$	$f_2(1270)$	S	1100
$2^{-+}2^{+}$	$\rho(770)$	P	1540	$2^{-+}2^{+}$	$f_2(1270)$	D	1580
$3^{++}0^{+}$	$[\pi\pi]_S$	F	1820	$3^{++}0^{+}$	$\rho(770)$	D	920
$3^{++}0^{+}$	$\rho(770)$	G	940	$3^{++}0^{+}$	$\rho_3(1690)$	D	1680
$3^{++}0^{+}$	$\rho_3(1690)$	S	1380	$3^{++}0^{+}$	$f_2(1270)$	P	960
$3^{++}1^{+}$	$[\pi\pi]_S$	F	1500	$3^{++}1^{+}$	$\rho(770)$	D	1060

J^{PC} M^{ε}	Isobar	L	Threshold [MeV/c^2]	J^{PC} M^{ε}	Isobar	L	Threshold [MeV/c^2]
$3^{++}1^{+}$	$\rho(770)$	G	1200	$3^{++}1^{+}$	$\rho_3(1690)$	S	1380
$3^{++}1^{+}$	$f_0(1500)$	F	2260	$3^{++}1^{+}$	$f_0(980)$	F	1900
$3^{++}1^{+}$	$f_2(1270)$	F	2120	$3^{++}1^{+}$	$f_2(1270)$	P	1140
$3^{-+}1^{+}$	$\rho(770)$	F	1280	$3^{-+}1^{+}$	$f_2(1270)$	D	1340
$3^{-+}1^{+}$	$f_2(1270)$	G	1700				
$4^{++}1^{+}$	$\rho(770)$	G	1140	$4^{++}1^{+}$	$\rho_3(1690)$	D	1700
$4^{++}1^{+}$	$f_2(1270)$	F	1520				
$4^{-+}0^{+}$	$[\pi\pi]_S$	G	1400	$4^{-+}0^{+}$	$\rho(770)$	F	900
$4^{-+}0^{+}$	$\rho(770)$	H	1800	$4^{-+}0^{+}$	$\rho_3(1690)$	P	1780
$4^{-+}0^{+}$	$f_0(1500)$	G	1780	$4^{-+}0^{+}$	$f_0(980)$	G	1820
$4^{-+}0^{+}$	$f_2(1270)$	D	1500	$4^{-+}0^{+}$	$f_2(1270)$	G	1600
$4^{-+}0^{+}$	$f_2(1270)$	I	2280	$4^{-+}1^{+}$	$[\pi\pi]_S$	G	1500
$4^{-+}1^{+}$	$\rho(770)$	F	860	$4^{-+}1^{+}$	$\rho(770)$	H	1780
$4^{-+}1^{+}$	$\rho_3(1690)$	P	1720	$4^{-+}1^{+}$	$f_0(1500)$	G	1440
$4^{-+}1^{+}$	$f_2(1270)$	D	1340	$4^{-+}1^{+}$	$f_2(1270)$	I	2120
$5^{++}0^{+}$	$\rho(770)$	G	1100	$5^{++}0^{+}$	$\rho(770)$	I	1680
$5^{++}0^{+}$	$\rho_3(1690)$	G	1780	$5^{++}0^{+}$	$f_0(1500)$	H	1400
$5^{++}0^{+}$	$f_2(1270)$	F	980	$5^{++}1^{+}$	$[\pi\pi]_S$	H	1540
$5^{++}1^{+}$	$\rho(770)$	G	1240	$5^{++}1^{+}$	$\rho(770)$	I	1380
$5^{++}1^{+}$	$\rho_3(1690)$	D	2140	$5^{++}1^{+}$	$f_0(1500)$	H	1300
$5^{++}1^{+}$	$f_0(980)$	H	1800	$5^{++}1^{+}$	$f_2(1270)$	F	1520
$5^{++}1^{+}$	$f_2(1270)$	H	2019				
$6^{++}1^{+}$	$\rho(770)$	I	1820	$6^{++}1^{+}$	$f_2(1270)$	H	2040
$6^{-+}0^{+}$	$[\pi\pi]_S$	I	1360	$6^{-+}0^{+}$	$\rho(770)$	H	1260
$6^{-+}0^{+}$	$\rho_3(1690)$	F	2019	$6^{-+}0^{+}$	$f_0(1500)$	I	1660
$6^{-+}0^{+}$	$f_2(1270)$	G	1760	$6^{-+}1^{+}$	$[\pi\pi]_S$	I	1980
$6^{-+}1^{+}$	$\rho(770)$	H	1280	$6^{-+}1^{+}$	$f_0(1500)$	I	1720
$6^{-+}1^{+}$	$f_2(1270)$	G	1660				
$1^{++}1^{-}$	$[\pi\pi]_S$	P	2100				
$2^{++}1^{-}$	$\rho(770)$	D	1140				
$2^{-+}1^{-}$	$[\pi\pi]_S$	D	1580				
$3^{++}1^{-}$	$\rho_3(1690)$	S	1740	$3^{++}1^{-}$	$f_2(1270)$	P	1580
$4^{++}1^{-}$	$\rho(770)$	G	2060				
$4^{-+}1^{-}$	$[\pi\pi]_S$	G	2160				
$5^{++}1^{-}$	$\rho(770)$	I	1960				
$6^{++}1^{-}$	$\rho(770)$	I	2000				

APPENDIX D

Derivation of the Hessian Matrix of the Likelihood Function

D.1 Gradient of the Likelihood Function

In order to calculate the first partial derivatives of the log-likelihood function equation (2.31) with respect to its arguments T^{ε}_{α} it is advantageous to expand the absolute squares terms:

$$\ln \mathcal{L} = \sum_{i=1}^{N} \ln \left[\sum_{\varepsilon=\pm 1} \sum_{\alpha,\beta}^{N^{\varepsilon}_{\text{waves}}} T^{\varepsilon}_{\alpha} T^{\varepsilon *}_{\beta} \underbrace{\Psi^{\varepsilon}_{\alpha}(\tau_i)\, \Psi^{\varepsilon *}_{\beta}(\tau_i)}_{\equiv D^{\varepsilon}_{\alpha\beta,i}} + T^2_{\text{flat}} \right] - \left[\sum_{\varepsilon=\pm 1} \sum_{\alpha,\beta}^{N^{\varepsilon}_{\text{waves}}} T^{\varepsilon}_{\alpha} T^{\varepsilon *}_{\beta} \mathcal{N}^{\epsilon}_{\alpha\beta} + T^2_{\text{flat}} \mathcal{A} \right] \quad \text{(D.1)}$$

where the $D^{\varepsilon}_{\alpha\beta,i}$ stand just for some complex numbers calculated from the decay amplitudes for every event.

In equation (D.1) we have two terms of the form

$$A_z \equiv \sum_{\varepsilon=\pm 1} \sum_{\alpha,\beta}^{N^{\varepsilon}_{\text{waves}}} T^{\varepsilon}_{\alpha} T^{\varepsilon *}_{\beta} z^{\varepsilon}_{\alpha\beta} + T^2_{\text{flat}} z_{\text{flat}} \quad \text{(D.2)}$$

The gradient of the likelihood function contains two kinds of elements: partial derivatives with respect to the real and the imaginary parts of the $\left\{T^{\varepsilon}_{\alpha}\right\}$. Defining

$$T^{\varepsilon}_{\alpha} \equiv x^{\varepsilon}_{\alpha} + \imath y^{\varepsilon}_{\alpha} \qquad \text{and} \qquad z^{\varepsilon}_{\alpha\beta} \equiv u^{\varepsilon}_{\alpha\beta} + \imath v^{\varepsilon}_{\alpha\beta} \quad \text{(D.3)}$$

with all x, y, u, and v being real numbers, we can calculate the derivative of A_z with respect to the real part of $T^{\tilde{\varepsilon}}_{\tilde{\alpha}}$ is

$$\frac{\partial A_z}{\partial x^{\tilde{\varepsilon}}_{\tilde{\alpha}}} = \frac{\partial}{\partial x^{\tilde{\varepsilon}}_{\tilde{\alpha}}}\left(\sum_{\varepsilon=\pm1}\sum_{\alpha,\beta}^{N^{\varepsilon}_{\text{waves}}}\left[(x^{\varepsilon}_{\alpha}\,x^{\varepsilon}_{\beta} + y^{\varepsilon}_{\alpha}\,y^{\varepsilon}_{\beta})\,u^{\varepsilon}_{\alpha\beta} - (y^{\varepsilon}_{\alpha}\,x^{\varepsilon}_{\beta} - x^{\varepsilon}_{\alpha}\,y^{\varepsilon}_{\beta})\,v^{\varepsilon}_{\alpha\beta}\right] + \imath\underbrace{\left[(y^{\varepsilon}_{\alpha}\,x^{\varepsilon}_{\beta} - x^{\varepsilon}_{\alpha}\,y^{\varepsilon}_{\beta})\,u^{\varepsilon}_{\alpha\beta} + (x^{\varepsilon}_{\alpha}\,x^{\varepsilon}_{\beta} + y^{\varepsilon}_{\alpha}\,y^{\varepsilon}_{\beta})\,v^{\varepsilon}_{\alpha\beta}\right]}_{\equiv B^{\varepsilon}_{\alpha\beta}} + T^2_{\text{flat}}\right) \tag{D.4}$$

One can show that $\sum_{\alpha,\beta}^{N^{\varepsilon}_{\text{waves}}} B^{\varepsilon}_{\alpha\beta} = 0$ [1] so that

$$\frac{\partial A_z}{\partial x^{\tilde{\varepsilon}}_{\tilde{\alpha}}} = \sum_{\varepsilon=\pm1}\sum_{\alpha,\beta}^{N^{\varepsilon}_{\text{waves}}}\left[\frac{\partial x^{\varepsilon}_{\alpha}}{\partial x^{\tilde{\varepsilon}}_{\tilde{\alpha}}}\;x^{\varepsilon}_{\beta} + x^{\varepsilon}_{\alpha}\;\frac{\partial x^{\varepsilon}_{\beta}}{\partial x^{\tilde{\varepsilon}}_{\tilde{\alpha}}}\right]u^{\varepsilon}_{\alpha\beta} - \left[y^{\varepsilon}_{\alpha}\;\frac{\partial x^{\varepsilon}_{\beta}}{\partial x^{\tilde{\varepsilon}}_{\tilde{\alpha}}} - \frac{\partial x^{\varepsilon}_{\alpha}}{\partial x^{\tilde{\varepsilon}}_{\tilde{\alpha}}}\;y^{\varepsilon}_{\beta}\right]v^{\varepsilon}_{\alpha\beta} \tag{D.6}$$

Since

$$\frac{\partial x^{\varepsilon}_{\alpha}}{\partial x^{\tilde{\varepsilon}}_{\tilde{\alpha}}} = \delta_{\varepsilon\tilde{\varepsilon}}\,\delta_{\alpha\tilde{\alpha}} \tag{D.7}$$

the sum over ε collapses as do some of the sums over the waves

$$\frac{\partial A_z}{\partial x^{\tilde{\varepsilon}}_{\tilde{\alpha}}} = \sum_{\alpha,\beta}^{N^{\tilde{\varepsilon}}_{\text{waves}}}\left[\delta_{\alpha\tilde{\alpha}}\,x^{\tilde{\varepsilon}}_{\beta} + x^{\tilde{\varepsilon}}_{\alpha}\,\delta_{\beta\tilde{\alpha}}\right]u^{\tilde{\varepsilon}}_{\alpha\beta} - \left[y^{\tilde{\varepsilon}}_{\alpha}\,\delta_{\beta\tilde{\alpha}} - \delta_{\alpha\tilde{\alpha}}\,y^{\tilde{\varepsilon}}_{\beta}\right]v^{\tilde{\varepsilon}}_{\alpha\beta} \tag{D.8}$$

$$= \sum_{\beta}^{N^{\tilde{\varepsilon}}_{\text{waves}}} x^{\tilde{\varepsilon}}_{\beta}\,u^{\tilde{\varepsilon}}_{\tilde{\alpha}\beta} + \sum_{\alpha}^{N^{\tilde{\varepsilon}}_{\text{waves}}} x^{\tilde{\varepsilon}}_{\alpha}\,u^{\tilde{\varepsilon}}_{\alpha\tilde{\alpha}} - \sum_{\alpha}^{N^{\tilde{\varepsilon}}_{\text{waves}}} y^{\tilde{\varepsilon}}_{\alpha}\,v^{\tilde{\varepsilon}}_{\alpha\tilde{\alpha}} + \sum_{\beta}^{N^{\tilde{\varepsilon}}_{\text{waves}}} y^{\tilde{\varepsilon}}_{\beta}\,v^{\tilde{\varepsilon}}_{\tilde{\alpha}\beta} \tag{D.9}$$

Using the fact that the matrix $z^{\varepsilon}_{\alpha\beta}$ is hermitian [cf. equation (D.5)], we can combine the sums and

---

[1] We use the fact that $z^{\varepsilon}_{\alpha\beta}$ is a hermitian matrix with real diagonal elements so that

$$u^{\varepsilon}_{\alpha\beta} = u^{\varepsilon}_{\beta\alpha}, \qquad v^{\varepsilon}_{\alpha\beta} = -v^{\varepsilon}_{\beta\alpha} \qquad \text{and} \qquad v^{\varepsilon}_{\alpha\alpha} = 0 \tag{D.5}$$

Therefore

$$\begin{aligned}
\sum_{\alpha,\beta}^{N^{\varepsilon}_{\text{waves}}} B^{\varepsilon}_{\alpha\beta} &= \sum_{\alpha,\beta}^{N^{\varepsilon}_{\text{waves}}}\left[(y^{\varepsilon}_{\alpha}\,x^{\varepsilon}_{\beta} - x^{\varepsilon}_{\alpha}\,y^{\varepsilon}_{\beta})\,u^{\varepsilon}_{\alpha\beta} + (x^{\varepsilon}_{\alpha}\,x^{\varepsilon}_{\beta} + y^{\varepsilon}_{\alpha}\,y^{\varepsilon}_{\beta})\,v^{\varepsilon}_{\alpha\beta}\right] \\
&= \underbrace{\sum_{\alpha,\beta}^{N^{\varepsilon}_{\text{waves}}} y^{\varepsilon}_{\alpha}\,x^{\varepsilon}_{\beta}\,u^{\varepsilon}_{\alpha\beta} - \sum_{\beta,\alpha}^{N^{\varepsilon}_{\text{waves}}} y^{\varepsilon}_{\beta}\,x^{\varepsilon}_{\alpha}\,u^{\varepsilon}_{\beta\alpha}}_{=0} \\
&\quad + \sum_{\substack{\alpha,\beta\\ \beta>\alpha}}^{N^{\varepsilon}_{\text{waves}}} (x^{\varepsilon}_{\alpha}\,x^{\varepsilon}_{\beta} + y^{\varepsilon}_{\alpha}\,y^{\varepsilon}_{\beta})\,v^{\varepsilon}_{\alpha\beta} + \sum_{\substack{\alpha,\beta\\ \beta<\alpha}}^{N^{\varepsilon}_{\text{waves}}} (x^{\varepsilon}_{\alpha}\,x^{\varepsilon}_{\beta} + y^{\varepsilon}_{\alpha}\,y^{\varepsilon}_{\beta})\,v^{\varepsilon}_{\alpha\beta} \\
&= \sum_{\substack{\alpha,\beta\\ \beta>\alpha}}^{N^{\varepsilon}_{\text{waves}}} (x^{\varepsilon}_{\alpha}\,x^{\varepsilon}_{\beta} + y^{\varepsilon}_{\alpha}\,y^{\varepsilon}_{\beta})\,v^{\varepsilon}_{\alpha\beta} - \sum_{\substack{\beta,\alpha\\ \alpha>\beta}}^{N^{\varepsilon}_{\text{waves}}} (x^{\varepsilon}_{\beta}\,x^{\varepsilon}_{\alpha} + y^{\varepsilon}_{\beta}\,y^{\varepsilon}_{\alpha})\,v^{\varepsilon}_{\beta\alpha} \\
&= 0
\end{aligned}$$

finally arrive at

$$\frac{\partial A_z}{\partial x^{\tilde{\varepsilon}}_{\tilde{\alpha}}} = \sum_{\beta}^{N^{\tilde{\varepsilon}}_{\text{waves}}} x^{\tilde{\varepsilon}}_{\beta}\, u^{\tilde{\varepsilon}}_{\beta\tilde{\alpha}} + \sum_{\alpha}^{N^{\tilde{\varepsilon}}_{\text{waves}}} x^{\tilde{\varepsilon}}_{\alpha}\, u^{\tilde{\varepsilon}}_{\alpha\tilde{\alpha}} - \sum_{\alpha}^{N^{\tilde{\varepsilon}}_{\text{waves}}} y^{\tilde{\varepsilon}}_{\alpha}\, v^{\tilde{\varepsilon}}_{\alpha\tilde{\alpha}} - \sum_{\beta}^{N^{\tilde{\varepsilon}}_{\text{waves}}} y^{\tilde{\varepsilon}}_{\beta}\, v^{\tilde{\varepsilon}}_{\beta\tilde{\alpha}} \tag{D.10}$$

$$= 2 \sum_{\beta}^{N^{\tilde{\varepsilon}}_{\text{waves}}} \left[x^{\tilde{\varepsilon}}_{\beta}\, u^{\tilde{\varepsilon}}_{\beta\tilde{\alpha}} - y^{\tilde{\varepsilon}}_{\beta}\, v^{\tilde{\varepsilon}}_{\beta\tilde{\alpha}}\right] = 2 \sum_{\beta}^{N^{\tilde{\varepsilon}}_{\text{waves}}} \Re\mathfrak{e}\left[T^{\tilde{\varepsilon}}_{\beta}\, z^{\tilde{\varepsilon}}_{\beta\tilde{\alpha}}\right] \tag{D.11}$$

Note that the sum runs only over the waves with the same reflectivity.

The corresponding derivative with respect to the imaginary part of the transition amplitude can be derived in an analogous way. However, from equation (D.4) one sees that one just needs to exchange the roles of the x and y:

$$\frac{\partial A_z}{\partial y^{\tilde{\varepsilon}}_{\tilde{\alpha}}} = 2 \sum_{\beta}^{N^{\tilde{\varepsilon}}_{\text{waves}}} \left[y^{\tilde{\varepsilon}}_{\beta}\, u^{\tilde{\varepsilon}}_{\beta\tilde{\alpha}} + x^{\tilde{\varepsilon}}_{\beta}\, v^{\tilde{\varepsilon}}_{\beta\tilde{\alpha}}\right] = 2 \sum_{\beta}^{N^{\tilde{\varepsilon}}_{\text{waves}}} \Im\mathfrak{m}\left[T^{\tilde{\varepsilon}}_{\beta}\, z^{\tilde{\varepsilon}}_{\beta\tilde{\alpha}}\right] \tag{D.12}$$

Using equations (D.11) and (D.12) we can calculate the derivatives of $\ln\mathcal{L}$ with respect to the real and imaginary parts of $T^{\tilde{\varepsilon}}_{\tilde{\alpha}}$:

$$\frac{\partial \ln\mathcal{L}}{\partial x^{\tilde{\varepsilon}}_{\tilde{\alpha}}} = \frac{\partial}{\partial x^{\tilde{\varepsilon}}_{\tilde{\alpha}}} \left(\sum_{i=1}^{N} \ln\left[A_{D_i}\right] + A_{\mathcal{N}}\right) \tag{D.13}$$

$$= \sum_{i=1}^{N} \frac{1}{A_{D_i}}\, \frac{\partial A_{D_i}}{\partial x^{\tilde{\varepsilon}}_{\tilde{\alpha}}} + \frac{\partial A_{\mathcal{N}}}{\partial x^{\tilde{\varepsilon}}_{\tilde{\alpha}}} \tag{D.14}$$

$$= \sum_{i=1}^{N} \frac{2}{A_{D_i}} \sum_{\beta}^{N^{\tilde{\varepsilon}}_{\text{waves}}} \underbrace{\left[x^{\tilde{\varepsilon}}_{\beta}\, u^{\tilde{\varepsilon}}_{\beta\tilde{\alpha},i} - y^{\tilde{\varepsilon}}_{\beta}\, v^{\tilde{\varepsilon}}_{\beta\tilde{\alpha},i}\right]}_{=\Re\mathfrak{e}\left[T^{\tilde{\varepsilon}}_{\beta}\, D^{\tilde{\varepsilon}}_{\beta\tilde{\alpha},i}\right]} - 2 \sum_{\beta}^{N^{\tilde{\varepsilon}}_{\text{waves}}} \underbrace{\left[x^{\tilde{\varepsilon}}_{\beta}\, U^{\tilde{\varepsilon}}_{\beta\tilde{\alpha}} - y^{\tilde{\varepsilon}}_{\beta}\, V^{\tilde{\varepsilon}}_{\beta\tilde{\alpha}}\right]}_{=\Re\mathfrak{e}\left[T^{\tilde{\varepsilon}}_{\beta}\, \mathcal{N}^{\tilde{\varepsilon}}_{\beta\tilde{\alpha}}\right]} \tag{D.15}$$

Analogously one gets

$$\frac{\partial \ln\mathcal{L}}{\partial y^{\tilde{\varepsilon}}_{\tilde{\alpha}}} = \sum_{i=1}^{N} \frac{2}{A_{D_i}} \sum_{\beta}^{N^{\tilde{\varepsilon}}_{\text{waves}}} \underbrace{\left[y^{\tilde{\varepsilon}}_{\beta}\, u^{\tilde{\varepsilon}}_{\beta\tilde{\alpha},i} + x^{\tilde{\varepsilon}}_{\beta}\, v^{\tilde{\varepsilon}}_{\beta\tilde{\alpha},i}\right]}_{=\Im\mathfrak{m}\left[T^{\tilde{\varepsilon}}_{\beta}\, D^{\tilde{\varepsilon}}_{\beta\tilde{\alpha},i}\right]} - 2 \sum_{\beta}^{N^{\tilde{\varepsilon}}_{\text{waves}}} \underbrace{\left[y^{\tilde{\varepsilon}}_{\beta}\, U^{\tilde{\varepsilon}}_{\beta\tilde{\alpha}} + x^{\tilde{\varepsilon}}_{\beta}\, V^{\tilde{\varepsilon}}_{\beta\tilde{\alpha}}\right]}_{=\Im\mathfrak{m}\left[T^{\tilde{\varepsilon}}_{\beta}\, \mathcal{N}^{\tilde{\varepsilon}}_{\beta\tilde{\alpha}}\right]} \tag{D.16}$$

In both equations we used the definitions

$$D^{\varepsilon}_{\alpha\beta,i} \equiv u^{\varepsilon}_{\alpha b,i} + \imath v^{\varepsilon}_{\alpha b,i} \qquad \text{and} \qquad \mathcal{N}^{\varepsilon}_{\alpha\beta} \equiv U^{\varepsilon}_{\alpha\beta} + \imath V^{\varepsilon}_{\alpha\beta} \tag{D.17}$$

D.2 Hessian Matrix of the Likelihood Function

In order to calculate the matrix of second partial derivatives of the likelihood function with respect to the real and imaginary parts of the transition amplitudes we start from the first partial derivatives as given in equations (D.15) and (D.16).

The second partial derivatives with respect to to the real parts of the transition amplitudes $T^{\tilde{\varepsilon}}_{\tilde{\alpha}}$ and T^{ε}_{α} are

$$\frac{\partial^2 \ln \mathcal{L}}{\partial x^{\varepsilon}_{\alpha} \partial x^{\tilde{\varepsilon}}_{\tilde{\alpha}}} = \frac{\partial}{\partial x^{\varepsilon}_{\alpha}} \left(\sum_{i=1}^{N} \frac{1}{A_{D_i}} \frac{\partial A_{D_i}}{\partial x^{\tilde{\varepsilon}}_{\tilde{\alpha}}} - \frac{\partial A_{\mathcal{N}}}{\partial x^{\tilde{\varepsilon}}_{\tilde{\alpha}}} \right) \tag{D.18}$$

$$= -\sum_{i=1}^{N} \frac{1}{A^2_{D_i}} \frac{\partial A_{D_i}}{\partial x^{\varepsilon}_{\alpha}} \frac{\partial A_{D_i}}{\partial x^{\tilde{\varepsilon}}_{\tilde{\alpha}}} + \sum_{i=1}^{N} \frac{1}{A_{D_i}} \frac{\partial^2 A_{D_i}}{\partial x^{\varepsilon}_{\alpha} \partial x^{\tilde{\varepsilon}}_{\tilde{\alpha}}} + \frac{\partial^2 A_{\mathcal{N}}}{\partial x^{\varepsilon}_{\alpha} \partial x^{\tilde{\varepsilon}}_{\tilde{\alpha}}} \tag{D.19}$$

Using equation (D.11) we know the first-derivative terms in the equation above and can calculate the second derivatives with equation (D.7):

$$\frac{\partial^2 A_z}{\partial x^{\varepsilon}_{\alpha} \partial x^{\tilde{\varepsilon}}_{\tilde{\alpha}}} = \frac{\partial}{\partial x^{\varepsilon}_{\alpha}} \left(2 \sum_{\beta}^{N^{\tilde{\varepsilon}}_{\text{waves}}} \left[x^{\tilde{\varepsilon}}_{\beta} u^{\tilde{\varepsilon}}_{\beta\tilde{\alpha}} - y^{\tilde{\varepsilon}}_{\beta} v^{\tilde{\varepsilon}}_{\beta\tilde{\alpha}} \right] \right) \tag{D.20}$$

$$= 2\delta_{\tilde{\varepsilon}\varepsilon} u^{\tilde{\varepsilon}}_{\alpha\tilde{\alpha}} \tag{D.21}$$

Therefore

$$\frac{\partial^2 \ln \mathcal{L}}{\partial x^{\varepsilon}_{\alpha} \partial x^{\tilde{\varepsilon}}_{\tilde{\alpha}}} = -\sum_{i=1}^{N} \frac{4}{A^2_{D_i}} \left(\sum_{\beta}^{N^{\varepsilon}_{\text{waves}}} \underbrace{\left[x^{\varepsilon}_{\beta} u^{\varepsilon}_{\beta\alpha,i} - y^{\varepsilon}_{\beta} v^{\varepsilon}_{\beta\alpha,i} \right]}_{=\Re\mathrm{e}\left[T^{\varepsilon}_{\beta} D^{\varepsilon}_{\beta\alpha,i}\right]} \right) \left(\sum_{\beta}^{N^{\tilde{\varepsilon}}_{\text{waves}}} \underbrace{\left[x^{\tilde{\varepsilon}}_{\beta} u^{\tilde{\varepsilon}}_{\beta\tilde{\alpha},i} - y^{\tilde{\varepsilon}}_{\beta} v^{\tilde{\varepsilon}}_{\beta\tilde{\alpha},i} \right]}_{=\Re\mathrm{e}\left[T^{\tilde{\varepsilon}}_{\beta} D^{\tilde{\varepsilon}}_{\beta\tilde{\alpha},i}\right]} \right)$$
$$2\delta_{\tilde{\varepsilon}\varepsilon} \left(\sum_{i=1}^{N} \frac{u^{\tilde{\varepsilon}}_{\alpha\tilde{\alpha},i}}{A_{D_i}} - U^{\tilde{\varepsilon}}_{\alpha\tilde{\alpha}} \right) \tag{D.22}$$

Similarly

$$\frac{\partial^2 A_z}{\partial y^{\varepsilon}_{\alpha} \partial y^{\tilde{\varepsilon}}_{\tilde{\alpha}}} = 2\delta_{\tilde{\varepsilon}\varepsilon} u^{\tilde{\varepsilon}}_{\alpha\tilde{\alpha}} \tag{D.23}$$

$$\frac{\partial^2 A_z}{\partial y^{\varepsilon}_{\alpha} \partial x^{\tilde{\varepsilon}}_{\tilde{\alpha}}} = -2\delta_{\tilde{\varepsilon}\varepsilon} v^{\tilde{\varepsilon}}_{\alpha\tilde{\alpha}} \tag{D.24}$$

$$\frac{\partial^2 A_z}{\partial x^{\varepsilon}_{\alpha} \partial y^{\tilde{\varepsilon}}_{\tilde{\alpha}}} = 2\delta_{\tilde{\varepsilon}\varepsilon} v^{\tilde{\varepsilon}}_{\alpha\tilde{\alpha}} \tag{D.25}$$

and so

$$\frac{\partial^2 \ln \mathcal{L}}{\partial y^{\varepsilon}_{\alpha} \partial y^{\tilde{\varepsilon}}_{\tilde{\alpha}}} = -\sum_{i=1}^{N} \frac{4}{A^2_{D_i}} \left(\sum_{\beta}^{N^{\varepsilon}_{\text{waves}}} \underbrace{\left[y^{\varepsilon}_{\beta}\, u^{\varepsilon}_{\beta\alpha,i} + x^{\varepsilon}_{\beta}\, v^{\varepsilon}_{\beta\alpha,i} \right]}_{=\Im\mathfrak{m}\left[T^{\varepsilon}_{\beta}\, D^{\varepsilon}_{\beta\alpha,i} \right]} \right) \left(\sum_{\beta}^{N^{\tilde{\varepsilon}}_{\text{waves}}} \underbrace{\left[y^{\tilde{\varepsilon}}_{\beta}\, u^{\tilde{\varepsilon}}_{\beta\tilde{\alpha},i} + x^{\tilde{\varepsilon}}_{\beta}\, v^{\tilde{\varepsilon}}_{\beta\tilde{\alpha},i} \right]}_{=\Im\mathfrak{m}\left[T^{\tilde{\varepsilon}}_{\beta}\, D^{\tilde{\varepsilon}}_{\beta\tilde{\alpha},i} \right]} \right) + 2\delta_{\tilde{\varepsilon}\varepsilon} \left(\sum_{i=1}^{N} \frac{u^{\tilde{\varepsilon}}_{\alpha\tilde{\alpha},i}}{A_{D_i}} - U^{\tilde{\varepsilon}}_{\alpha\tilde{\alpha}} \right) \tag{D.26}$$

$$\frac{\partial^2 \ln \mathcal{L}}{\partial y^{\varepsilon}_{\alpha} \partial x^{\tilde{\varepsilon}}_{\tilde{\alpha}}} = -\sum_{i=1}^{N} \frac{4}{A^2_{D_i}} \left(\sum_{\beta}^{N^{\varepsilon}_{\text{waves}}} \underbrace{\left[y^{\varepsilon}_{\beta}\, u^{\varepsilon}_{\beta\alpha,i} + x^{\varepsilon}_{\beta}\, v^{\varepsilon}_{\beta\alpha,i} \right]}_{=\Im\mathfrak{m}\left[T^{\varepsilon}_{\beta}\, D^{\varepsilon}_{\beta\alpha,i} \right]} \right) \left(\sum_{\beta}^{N^{\tilde{\varepsilon}}_{\text{waves}}} \underbrace{\left[x^{\tilde{\varepsilon}}_{\beta}\, u^{\tilde{\varepsilon}}_{\beta\tilde{\alpha},i} - y^{\tilde{\varepsilon}}_{\beta}\, v^{\tilde{\varepsilon}}_{\beta\tilde{\alpha},i} \right]}_{=\Re\mathfrak{e}\left[T^{\tilde{\varepsilon}}_{\beta}\, D^{\tilde{\varepsilon}}_{\beta\tilde{\alpha},i} \right]} \right) - 2\delta_{\tilde{\varepsilon}\varepsilon} \left(\sum_{i=1}^{N} \frac{v^{\tilde{\varepsilon}}_{\alpha\tilde{\alpha},i}}{A_{D_i}} - V^{\tilde{\varepsilon}}_{\alpha\tilde{\alpha}} \right) \tag{D.27}$$

$$\frac{\partial^2 \ln \mathcal{L}}{\partial x^{\varepsilon}_{\alpha} \partial y^{\tilde{\varepsilon}}_{\tilde{\alpha}}} = -\sum_{i=1}^{N} \frac{4}{A^2_{D_i}} \left(\sum_{\beta}^{N^{\varepsilon}_{\text{waves}}} \underbrace{\left[x^{\varepsilon}_{\beta}\, u^{\varepsilon}_{\beta\alpha,i} - y^{\varepsilon}_{\beta}\, v^{\varepsilon}_{\beta\alpha,i} \right]}_{=\Re\mathfrak{e}\left[T^{\varepsilon}_{\beta}\, D^{\varepsilon}_{\beta\alpha,i} \right]} \right) \left(\sum_{\beta}^{N^{\tilde{\varepsilon}}_{\text{waves}}} \underbrace{\left[y^{\tilde{\varepsilon}}_{\beta}\, u^{\tilde{\varepsilon}}_{\beta\tilde{\alpha},i} + x^{\tilde{\varepsilon}}_{\beta}\, v^{\tilde{\varepsilon}}_{\beta\tilde{\alpha},i} \right]}_{=\Im\mathfrak{m}\left[T^{\tilde{\varepsilon}}_{\beta}\, D^{\tilde{\varepsilon}}_{\beta\tilde{\alpha},i} \right]} \right) + 2\delta_{\tilde{\varepsilon}\varepsilon} \left(\sum_{i=1}^{N} \frac{v^{\tilde{\varepsilon}}_{\alpha\tilde{\alpha},i}}{A_{D_i}} - V^{\tilde{\varepsilon}}_{\alpha\tilde{\alpha}} \right) \tag{D.28}$$

APPENDIX E

Intensity Plots for All Waves of the Combined Wave Set

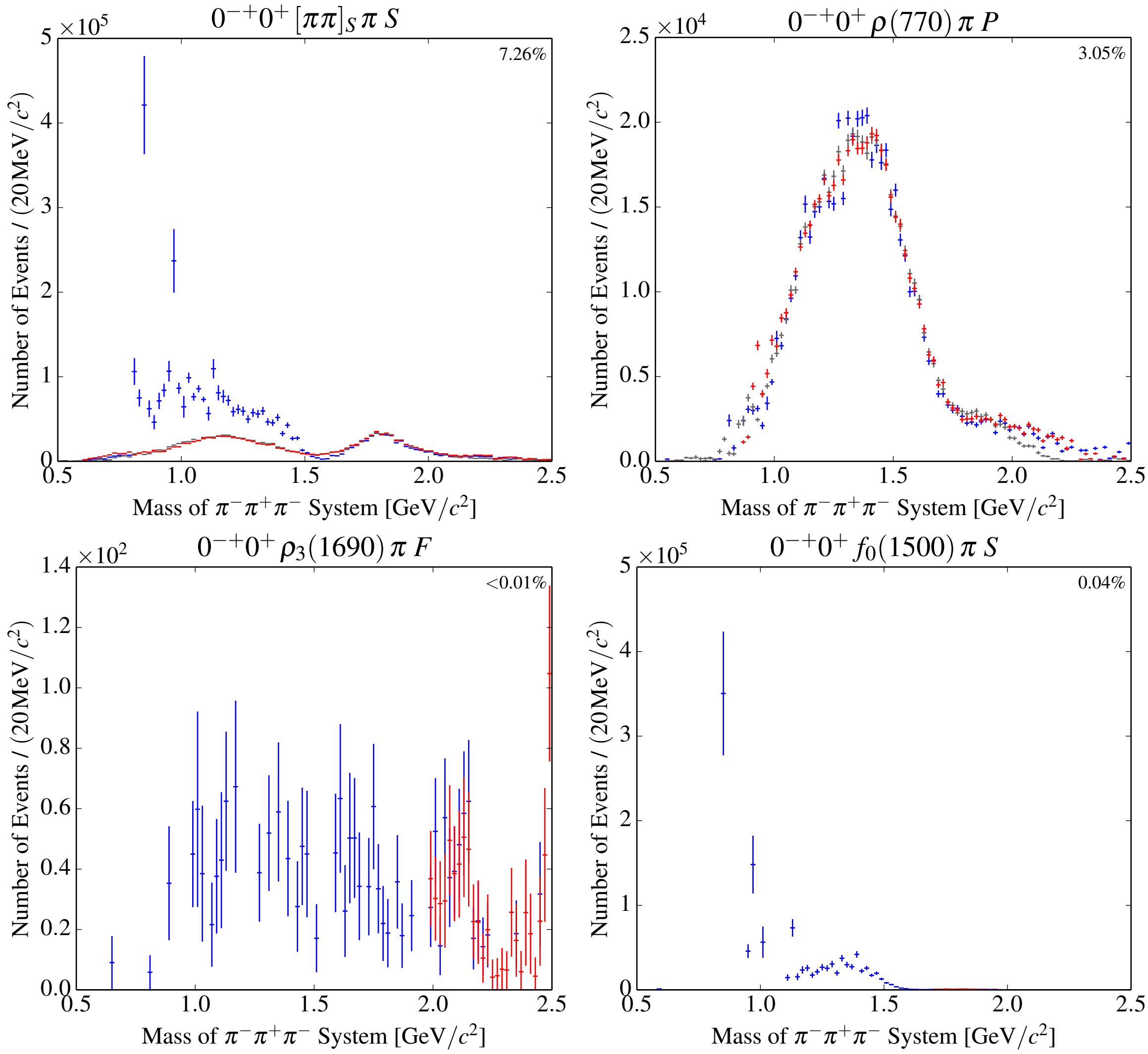

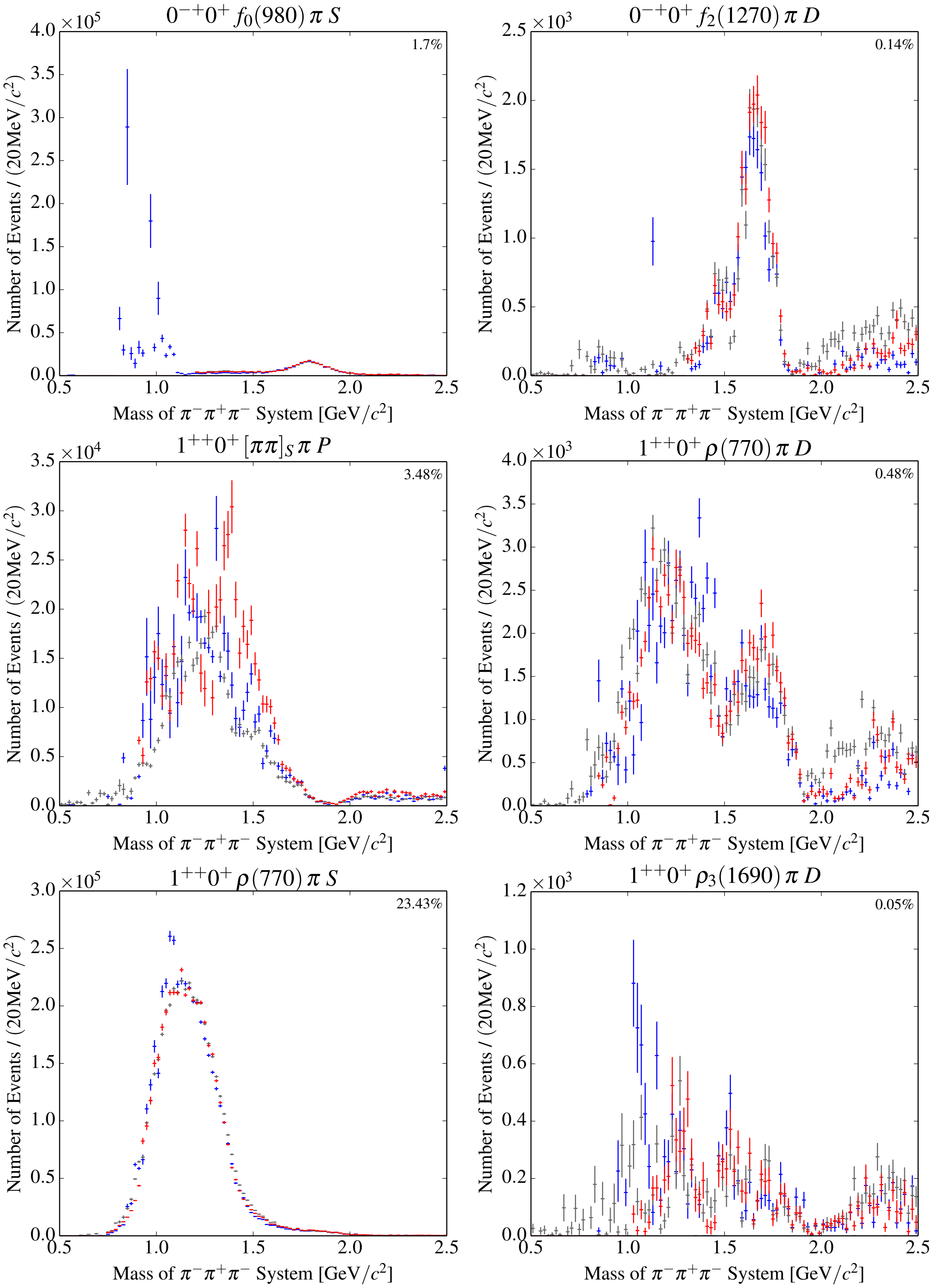
$0^{-+}0^{+}\, f_0(980)\,\pi\, S$
1.7%
$0^{-+}0^{+}\, f_2(1270)\,\pi\, D$
0.14%
$1^{++}0^{+}\, [\pi\pi]_S\,\pi\, P$
3.48%
$1^{++}0^{+}\, \rho(770)\,\pi\, D$
0.48%
$1^{++}0^{+}\, \rho(770)\,\pi\, S$
23.43%
$1^{++}0^{+}\, \rho_3(1690)\,\pi\, D$
0.05%
Number of Events / (20MeV/c^2)
Mass of $\pi^-\pi^+\pi^-$ System [GeV/c^2]
$\times 10^5$
$\times 10^3$
$\times 10^4$

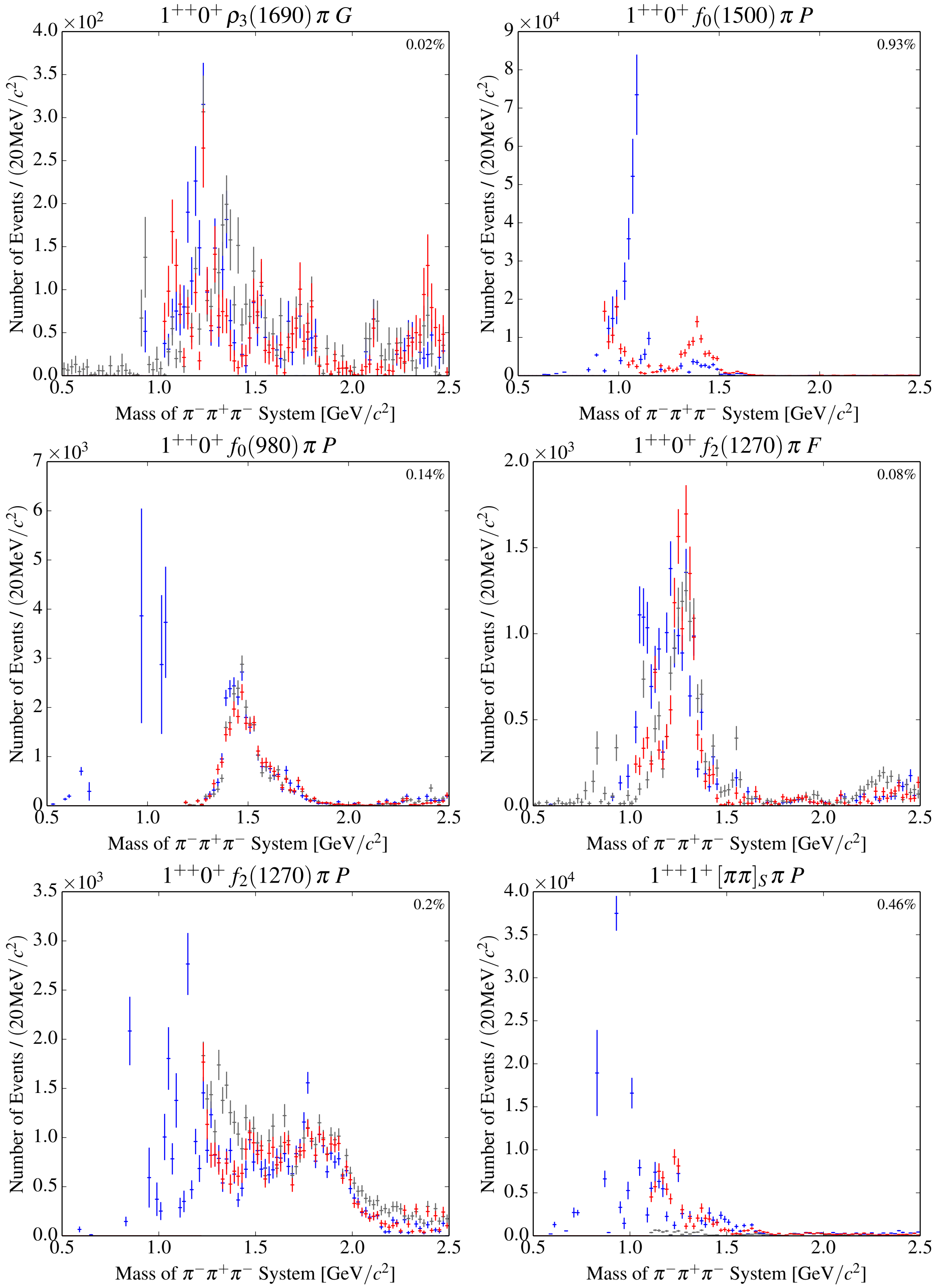

1++0+ ρ3(1690) π G
0.02%
×10^2
Number of Events / (20MeV/c^2)
Mass of π−π+π− System [GeV/c^2]
1++0+ f0(1500) π P
0.93%
×10^4
1++0+ f0(980) π P
0.14%
×10^3
1++0+ f2(1270) π F
0.08%
×10^3
1++0+ f2(1270) π P
0.2%
×10^3
1++1+ [ππ]S π P
0.46%
×10^4

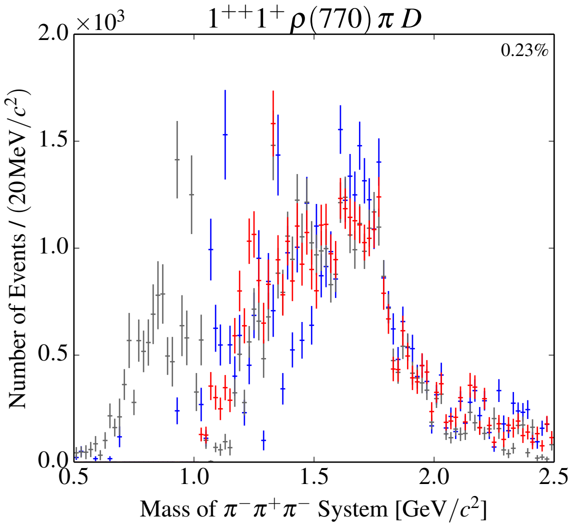
$1^{++}1^{+}\rho(770)\,\pi\,D$
0.23%
$\times10^{3}$
Number of Events / (20MeV/c^2)
Mass of $\pi^-\pi^+\pi^-$ System [GeV/c^2]

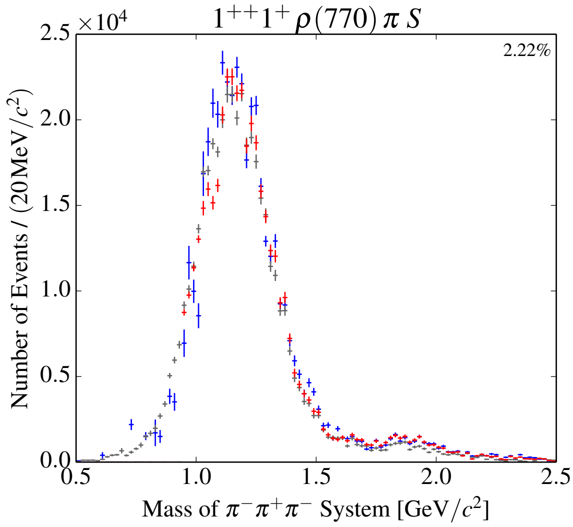
$1^{++}1^{+}\rho(770)\,\pi\,S$
2.22%
$\times10^{4}$
Number of Events / (20MeV/c^2)
Mass of $\pi^-\pi^+\pi^-$ System [GeV/c^2]

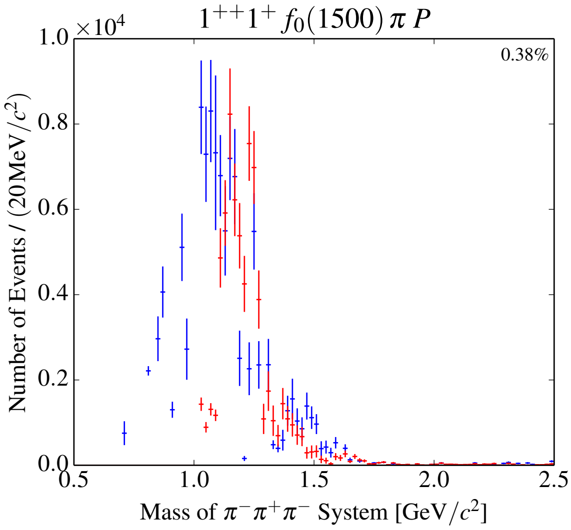
$1^{++}1^{+}f_0(1500)\,\pi\,P$
0.38%
$\times10^{4}$
Number of Events / (20MeV/c^2)
Mass of $\pi^-\pi^+\pi^-$ System [GeV/c^2]

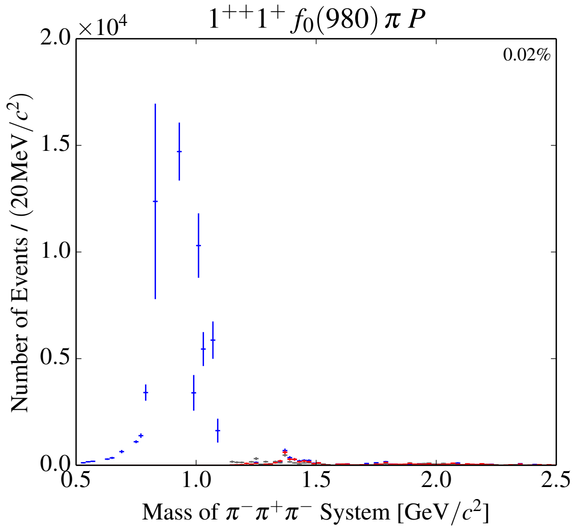
$1^{++}1^{+}f_0(980)\,\pi\,P$
0.02%
$\times10^{4}$
Number of Events / (20MeV/c^2)
Mass of $\pi^-\pi^+\pi^-$ System [GeV/c^2]

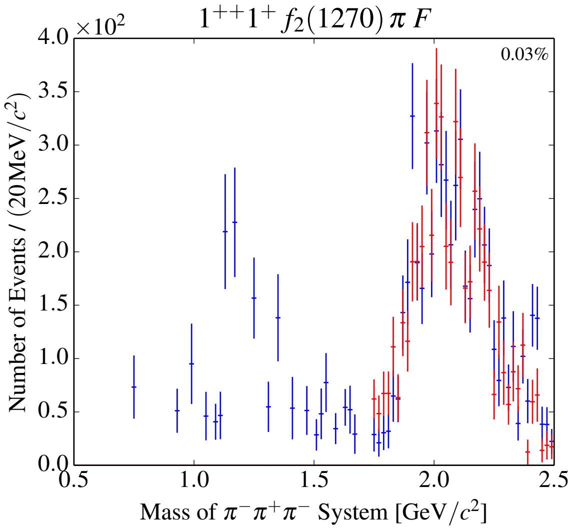
$1^{++}1^{+}f_2(1270)\,\pi\,F$
0.03%
$\times10^{2}$
Number of Events / (20MeV/c^2)
Mass of $\pi^-\pi^+\pi^-$ System [GeV/c^2]

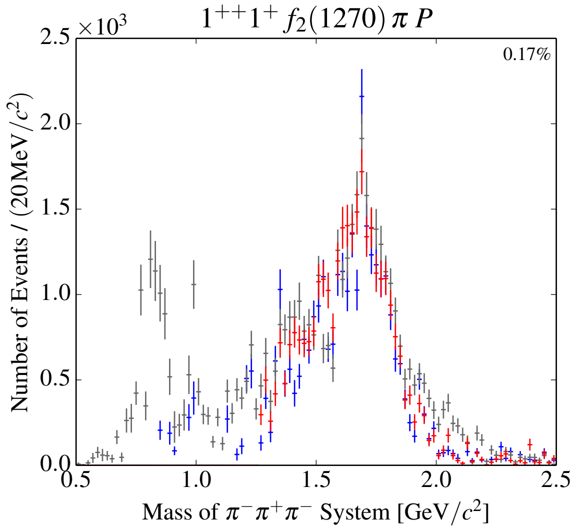
$1^{++}1^{+}f_2(1270)\,\pi\,P$
0.17%
$\times10^{3}$
Number of Events / (20MeV/c^2)
Mass of $\pi^-\pi^+\pi^-$ System [GeV/c^2]

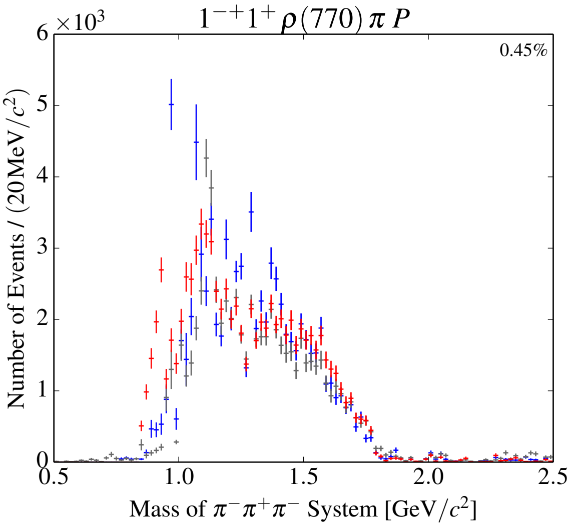
$1^{-+}1^{+}\rho(770)\,\pi\,P$
0.45%
Number of Events / (20MeV/c^2)
Mass of $\pi^-\pi^+\pi^-$ System [GeV/c^2]

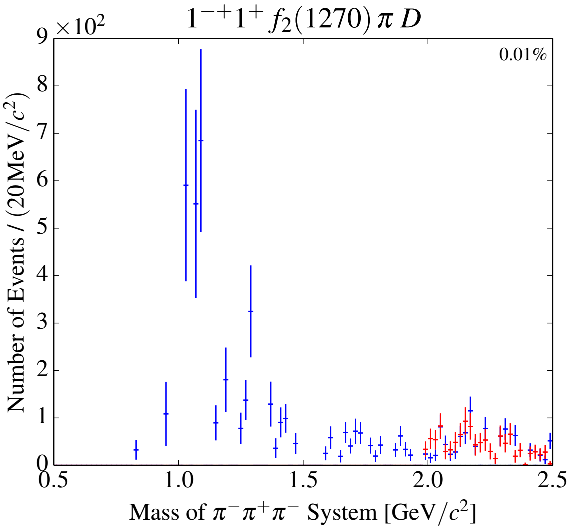
$1^{-+}1^{+}f_2(1270)\,\pi\,D$
0.01%
Number of Events / (20MeV/c^2)
Mass of $\pi^-\pi^+\pi^-$ System [GeV/c^2]

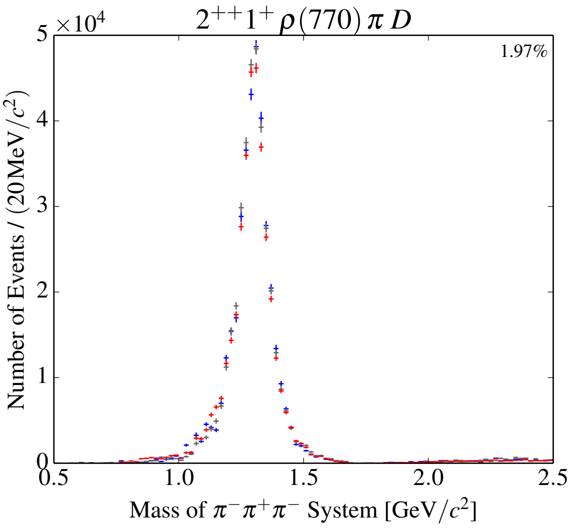
$2^{++}1^{+}\rho(770)\,\pi\,D$
1.97%
Number of Events / (20MeV/c^2)
Mass of $\pi^-\pi^+\pi^-$ System [GeV/c^2]

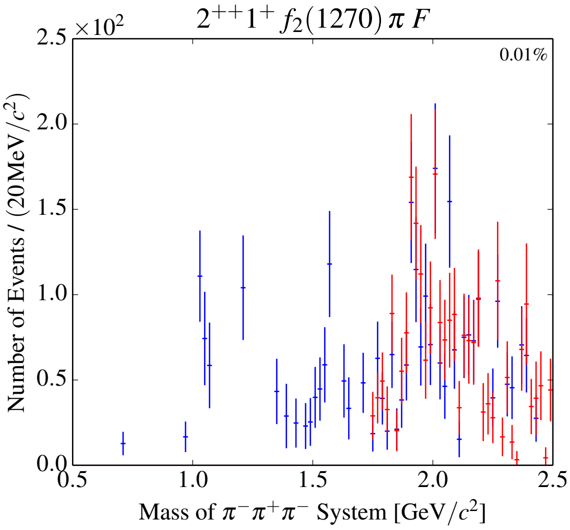
$2^{++}1^{+}f_2(1270)\,\pi\,F$
0.01%
Number of Events / (20MeV/c^2)
Mass of $\pi^-\pi^+\pi^-$ System [GeV/c^2]

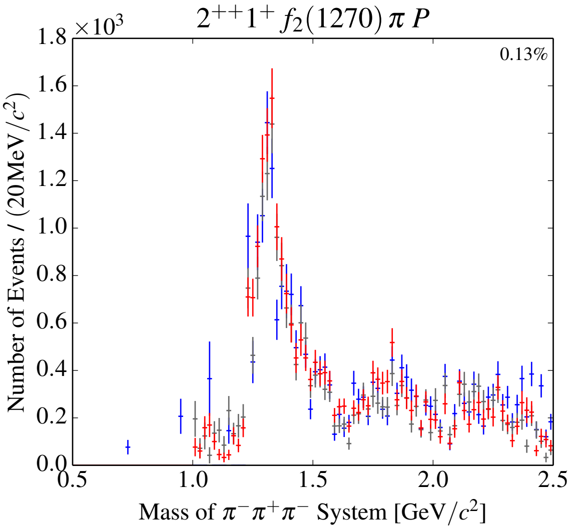
$2^{++}1^{+}f_2(1270)\,\pi\,P$
0.13%
Number of Events / (20MeV/c^2)
Mass of $\pi^-\pi^+\pi^-$ System [GeV/c^2]

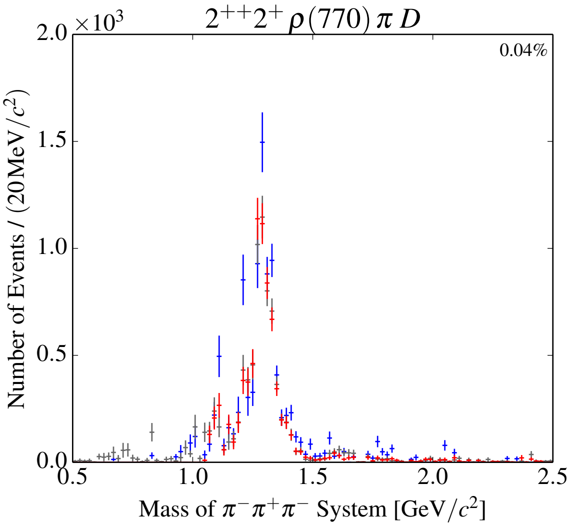
$2^{++}2^{+}\rho(770)\,\pi\,D$
0.04%
Number of Events / (20MeV/c^2)
Mass of $\pi^-\pi^+\pi^-$ System [GeV/c^2]

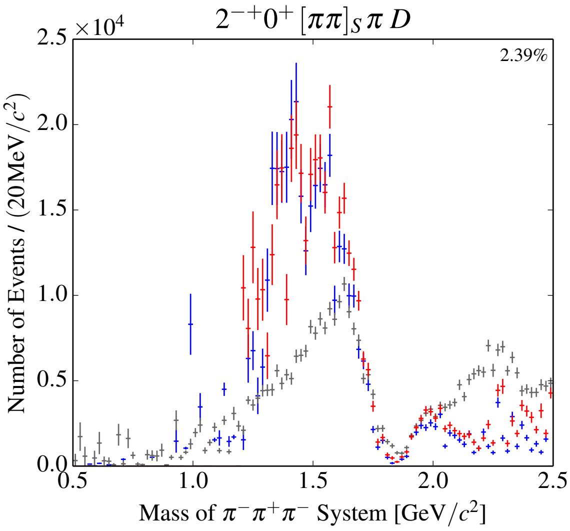
$2^{-+}0^{+}\,[\pi\pi]_S\,\pi\,D$
$\times 10^4$
2.39%
Number of Events / (20MeV/c^2)
Mass of $\pi^-\pi^+\pi^-$ System [GeV/c^2]

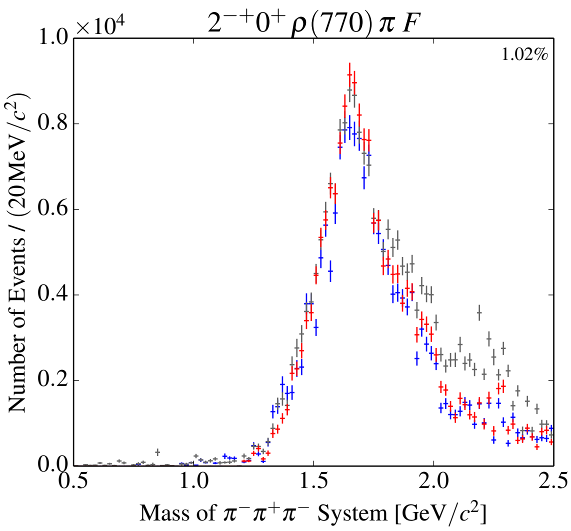
$2^{-+}0^{+}\,\rho(770)\,\pi\,F$
$\times 10^4$
1.02%
Number of Events / (20MeV/c^2)
Mass of $\pi^-\pi^+\pi^-$ System [GeV/c^2]

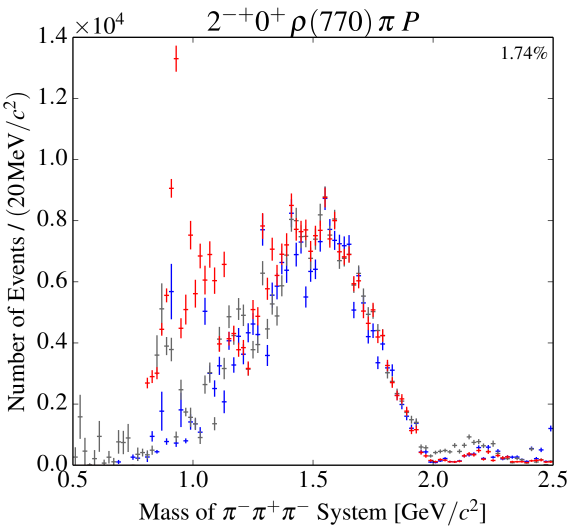
$2^{-+}0^{+}\,\rho(770)\,\pi\,P$
$\times 10^4$
1.74%
Number of Events / (20MeV/c^2)
Mass of $\pi^-\pi^+\pi^-$ System [GeV/c^2]

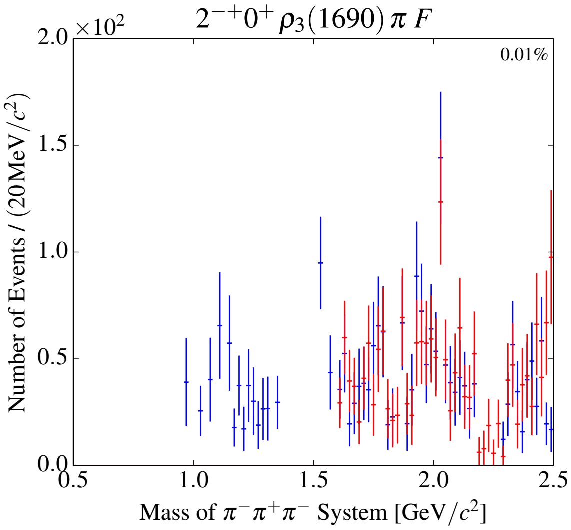
$2^{-+}0^{+}\,\rho_3(1690)\,\pi\,F$
$\times 10^2$
0.01%
Number of Events / (20MeV/c^2)
Mass of $\pi^-\pi^+\pi^-$ System [GeV/c^2]

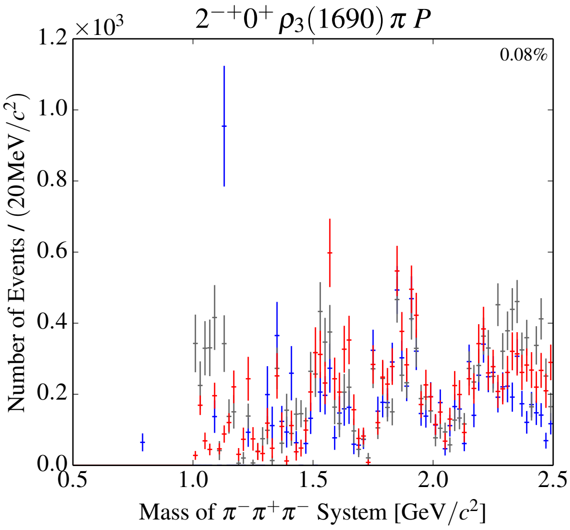
$2^{-+}0^{+}\,\rho_3(1690)\,\pi\,P$
$\times 10^3$
0.08%
Number of Events / (20MeV/c^2)
Mass of $\pi^-\pi^+\pi^-$ System [GeV/c^2]

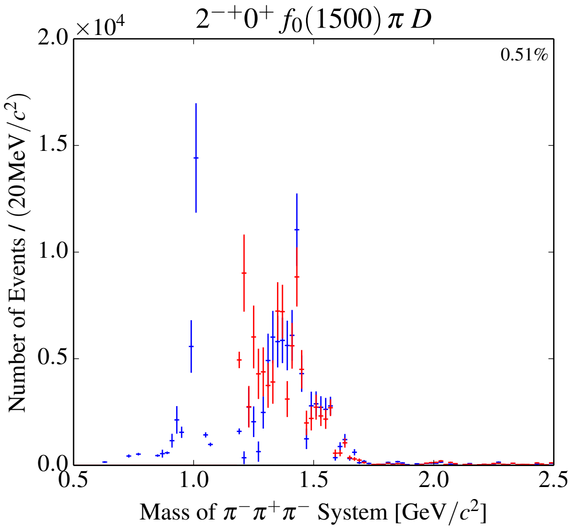
$2^{-+}0^{+}\,f_0(1500)\,\pi\,D$
$\times 10^4$
0.51%
Number of Events / (20MeV/c^2)
Mass of $\pi^-\pi^+\pi^-$ System [GeV/c^2]

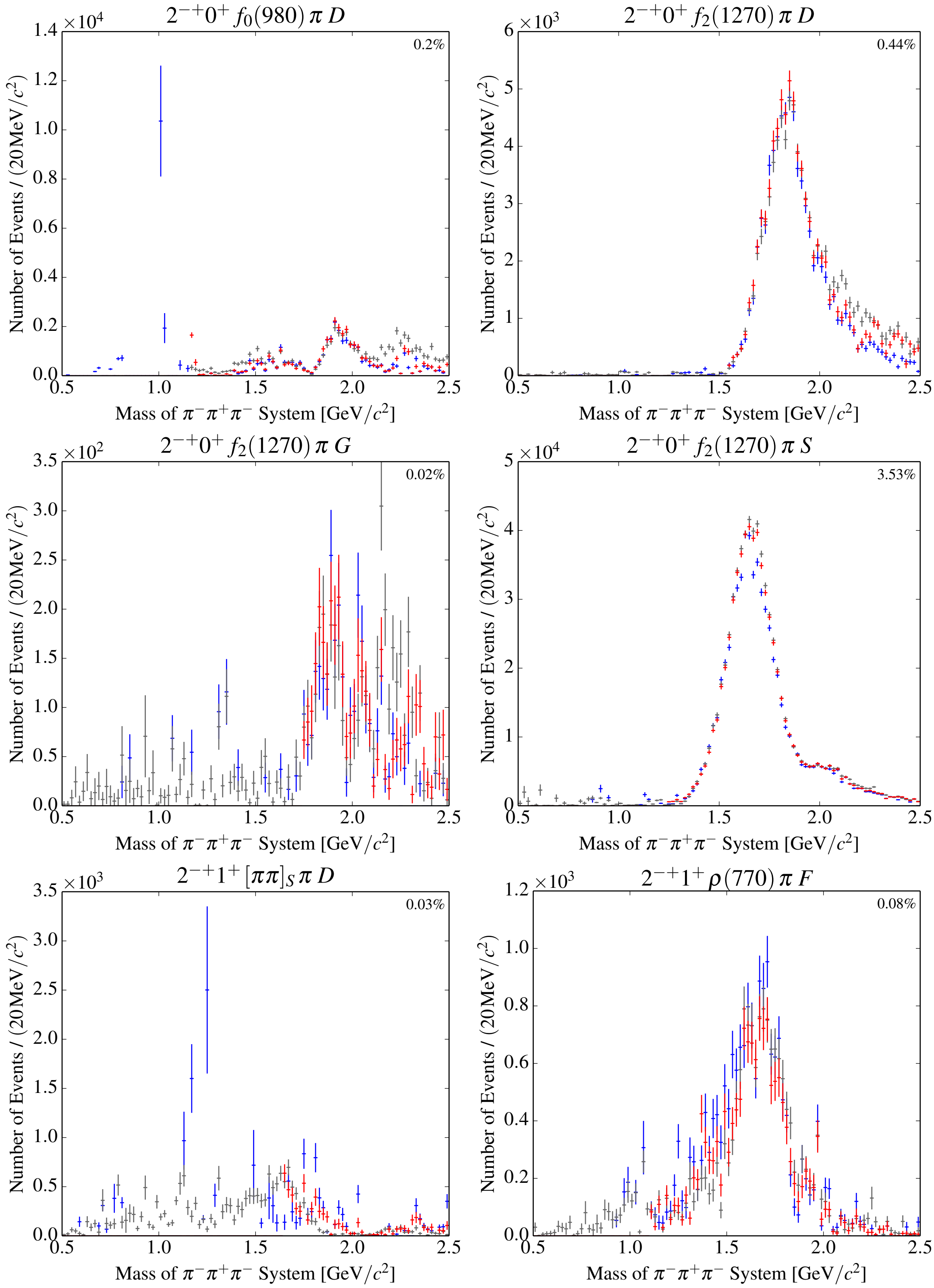
$2^{-+}0^{+}\, f_0(980)\,\pi\, D$
0.2%
$2^{-+}0^{+}\, f_2(1270)\,\pi\, D$
0.44%
$2^{-+}0^{+}\, f_2(1270)\,\pi\, G$
0.02%
$2^{-+}0^{+}\, f_2(1270)\,\pi\, S$
3.53%
$2^{-+}1^{+}\, [\pi\pi]_S\,\pi\, D$
0.03%
$2^{-+}1^{+}\, \rho(770)\,\pi\, F$
0.08%
Number of Events / (20MeV/c^2)
Mass of $\pi^-\pi^+\pi^-$ System [GeV/c^2]

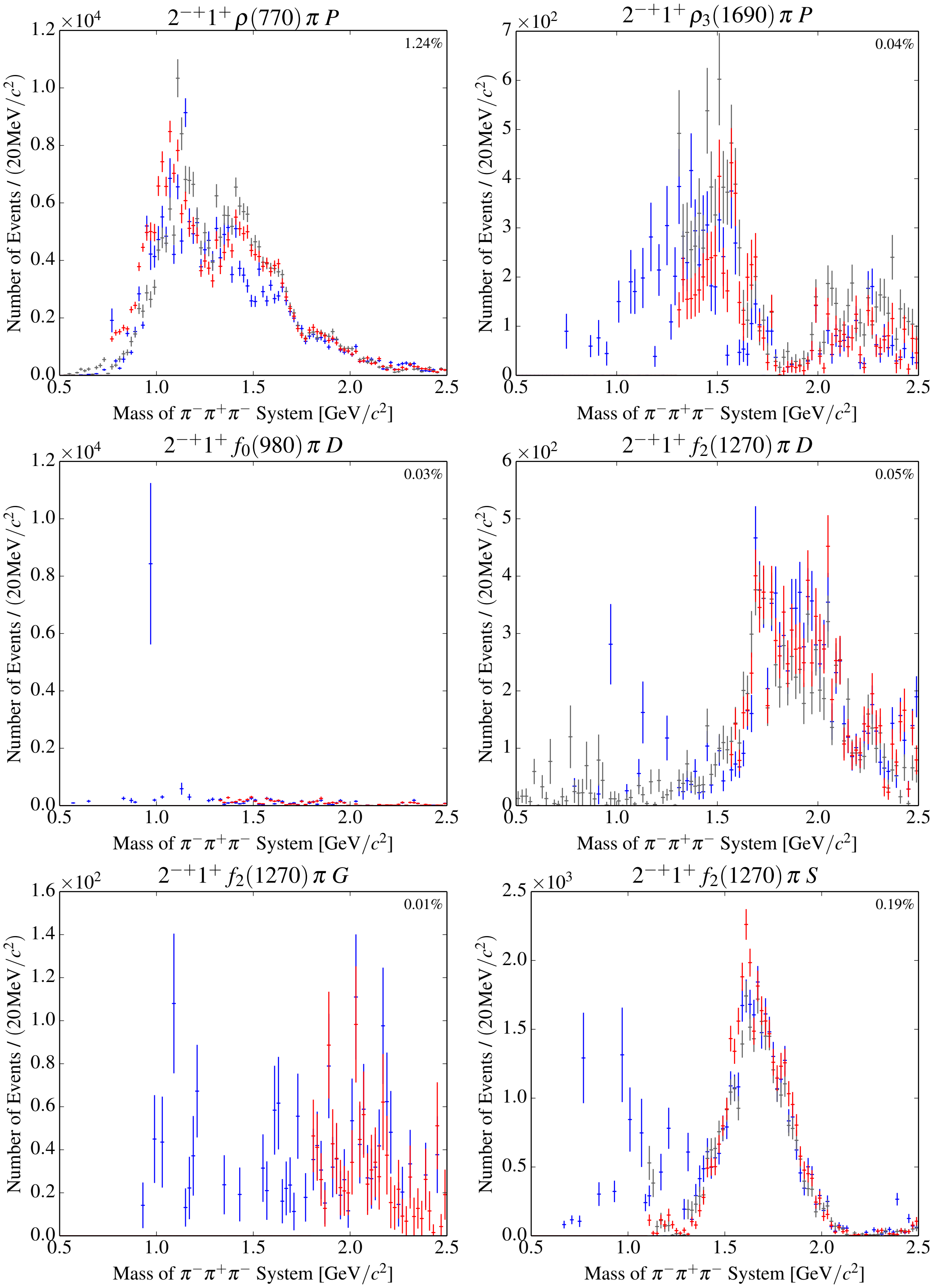
$2^{-+}1^+ \rho(770)\,\pi\, P$
1.24%
$2^{-+}1^+ \rho_3(1690)\,\pi\, P$
0.04%
$2^{-+}1^+ f_0(980)\,\pi\, D$
0.03%
$2^{-+}1^+ f_2(1270)\,\pi\, D$
0.05%
$2^{-+}1^+ f_2(1270)\,\pi\, G$
0.01%
$2^{-+}1^+ f_2(1270)\,\pi\, S$
0.19%
Number of Events / (20MeV/c^2)
Mass of $\pi^-\pi^+\pi^-$ System [GeV/c^2]

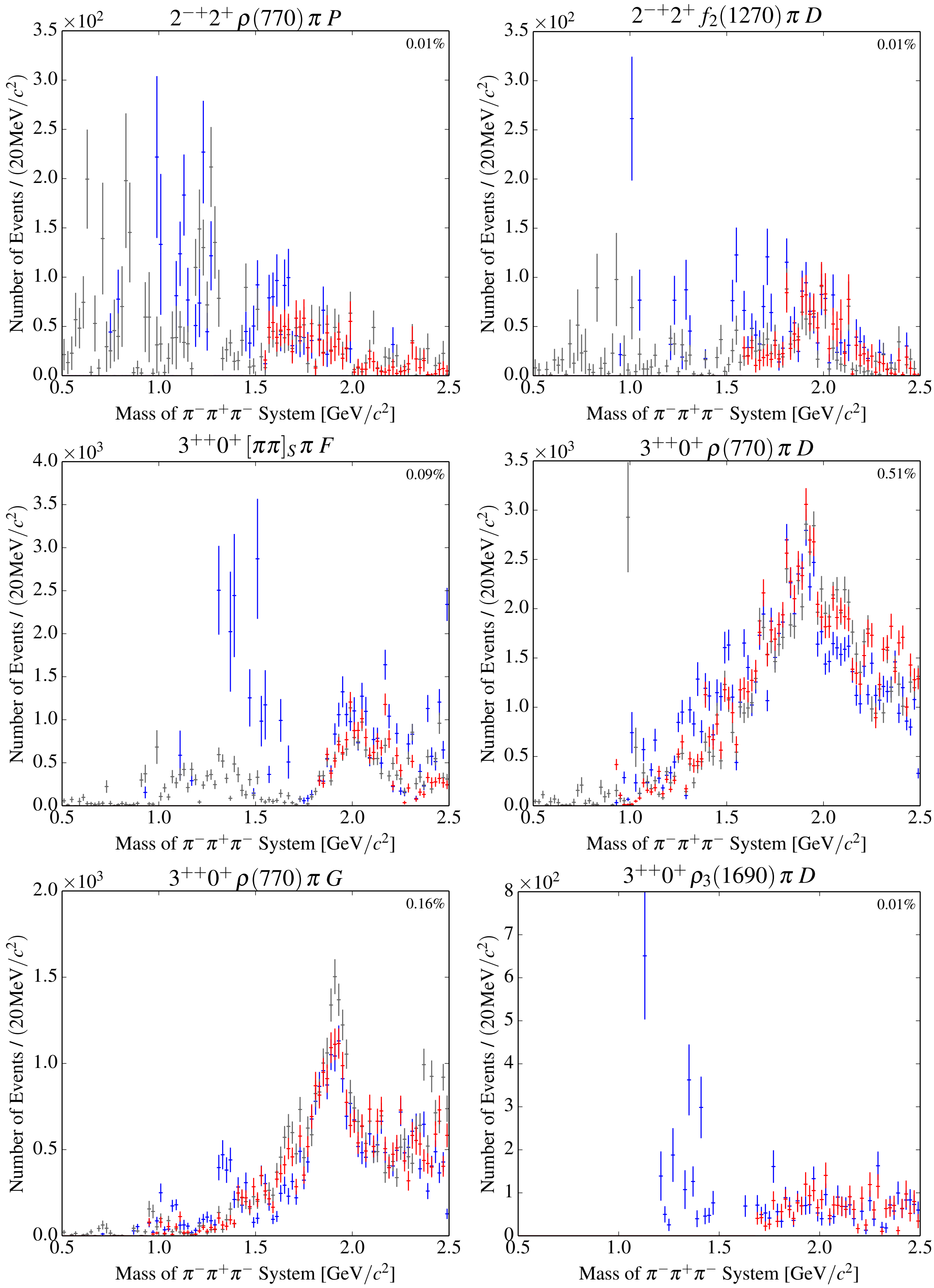

$2^{-+}2^{+}\,\rho(770)\,\pi\,P$
0.01%
$\times 10^{2}$
Number of Events / (20MeV/c^2)
Mass of $\pi^-\pi^+\pi^-$ System [GeV/c^2]
$2^{-+}2^{+}\,f_2(1270)\,\pi\,D$
0.01%
$\times 10^{2}$
Number of Events / (20MeV/c^2)
Mass of $\pi^-\pi^+\pi^-$ System [GeV/c^2]
$3^{++}0^{+}\,[\pi\pi]_S\,\pi\,F$
0.09%
$\times 10^{3}$
Number of Events / (20MeV/c^2)
Mass of $\pi^-\pi^+\pi^-$ System [GeV/c^2]
$3^{++}0^{+}\,\rho(770)\,\pi\,D$
0.51%
$\times 10^{3}$
Number of Events / (20MeV/c^2)
Mass of $\pi^-\pi^+\pi^-$ System [GeV/c^2]
$3^{++}0^{+}\,\rho(770)\,\pi\,G$
0.16%
$\times 10^{3}$
Number of Events / (20MeV/c^2)
Mass of $\pi^-\pi^+\pi^-$ System [GeV/c^2]
$3^{++}0^{+}\,\rho_3(1690)\,\pi\,D$
0.01%
$\times 10^{2}$
Number of Events / (20MeV/c^2)
Mass of $\pi^-\pi^+\pi^-$ System [GeV/c^2]

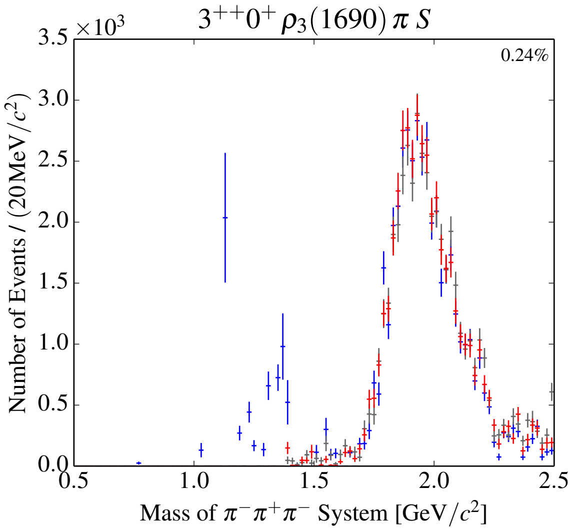
$3^{++}0^{+}\,\rho_3(1690)\,\pi\,S$
0.24%
$\times10^3$
Number of Events / (20MeV/c^2)
Mass of $\pi^-\pi^+\pi^-$ System [GeV/c^2]

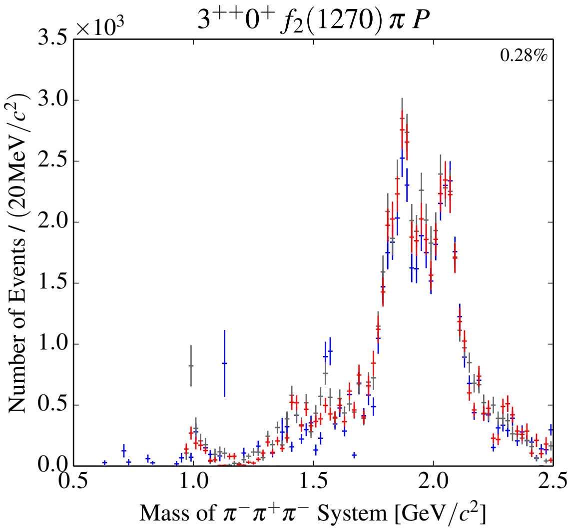
$3^{++}0^{+}\,f_2(1270)\,\pi\,P$
0.28%
$\times10^3$
Number of Events / (20MeV/c^2)
Mass of $\pi^-\pi^+\pi^-$ System [GeV/c^2]

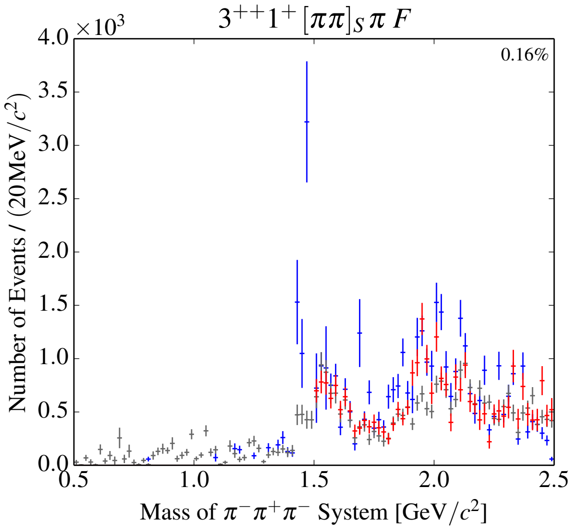
$3^{++}1^{+}\,[\pi\pi]_S\,\pi\,F$
0.16%
$\times10^3$
Number of Events / (20MeV/c^2)
Mass of $\pi^-\pi^+\pi^-$ System [GeV/c^2]

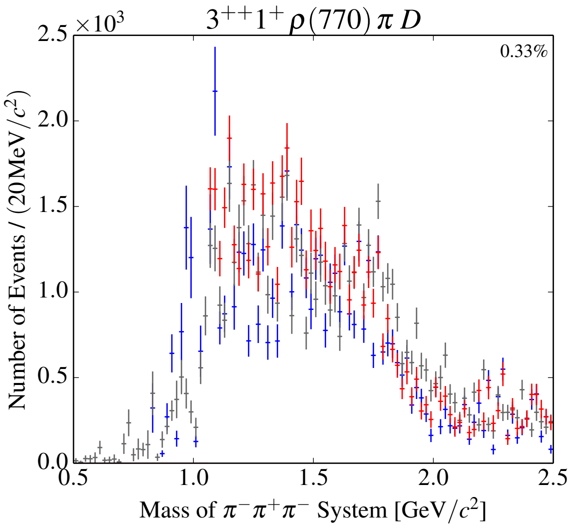
$3^{++}1^{+}\,\rho(770)\,\pi\,D$
0.33%
$\times10^3$
Number of Events / (20MeV/c^2)
Mass of $\pi^-\pi^+\pi^-$ System [GeV/c^2]

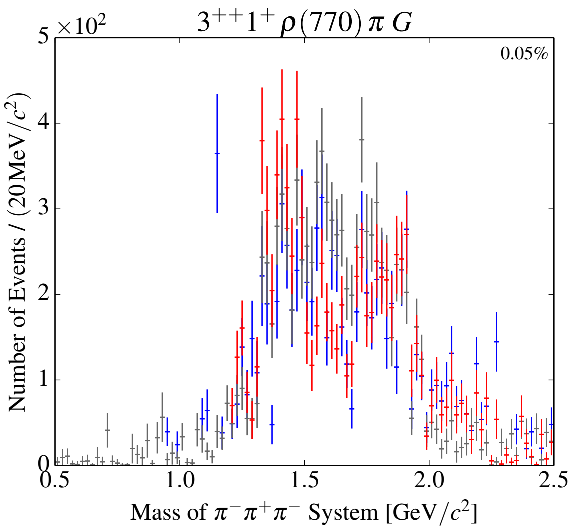
$3^{++}1^{+}\,\rho(770)\,\pi\,G$
0.05%
$\times10^2$
Number of Events / (20MeV/c^2)
Mass of $\pi^-\pi^+\pi^-$ System [GeV/c^2]

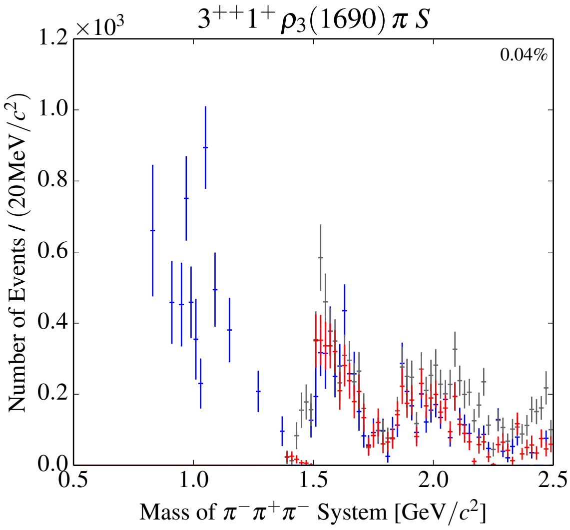
$3^{++}1^{+}\,\rho_3(1690)\,\pi\,S$
0.04%
$\times10^3$
Number of Events / (20MeV/c^2)
Mass of $\pi^-\pi^+\pi^-$ System [GeV/c^2]

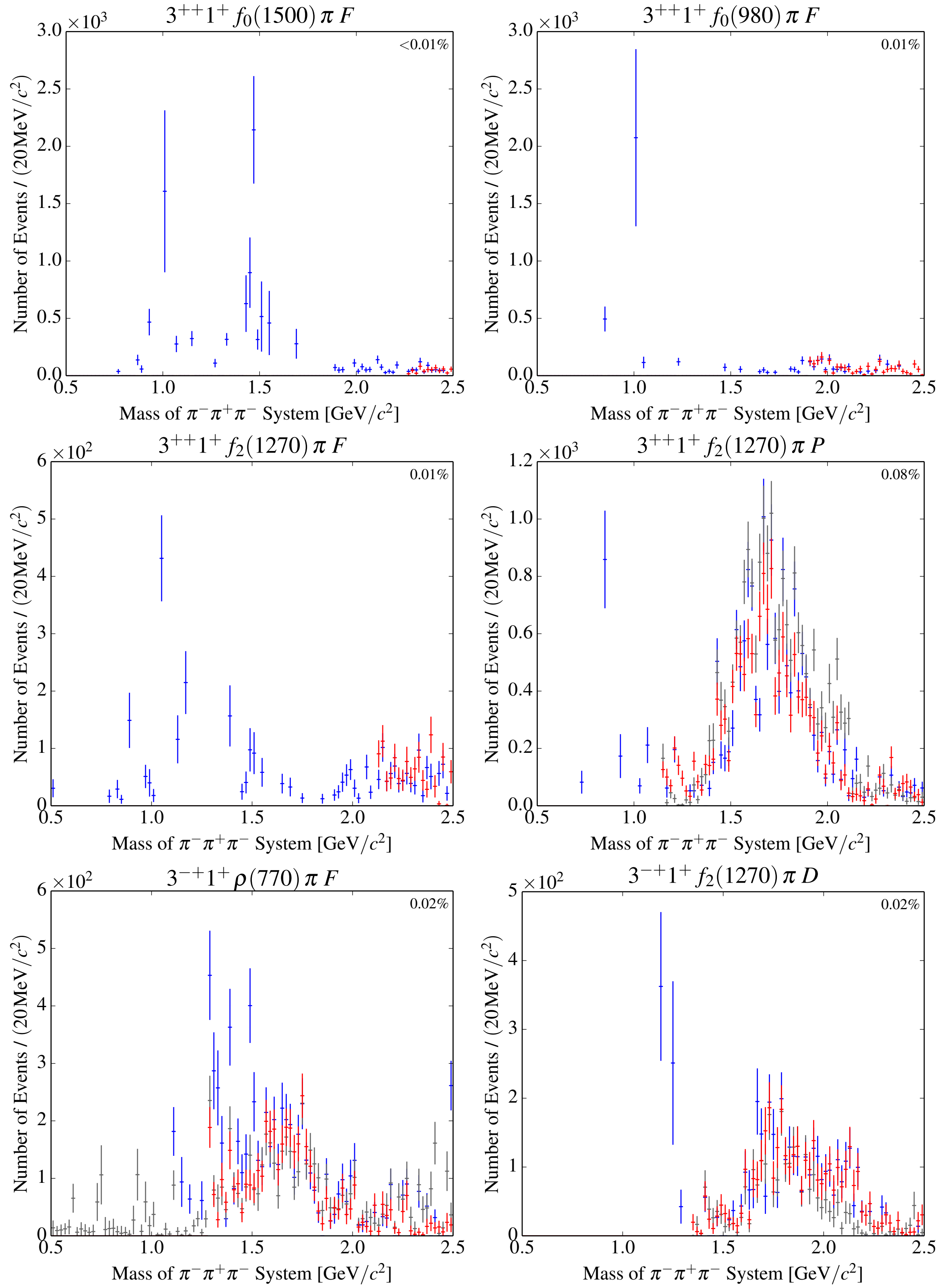

3++1+ f0(1500) π F
<0.01%
3++1+ f0(980) π F
0.01%
3++1+ f2(1270) π F
0.01%
3++1+ f2(1270) π P
0.08%
3−+1+ ρ(770) π F
0.02%
3−+1+ f2(1270) π D
0.02%
Number of Events / (20MeV/c2)
Mass of π−π+π− System [GeV/c2]

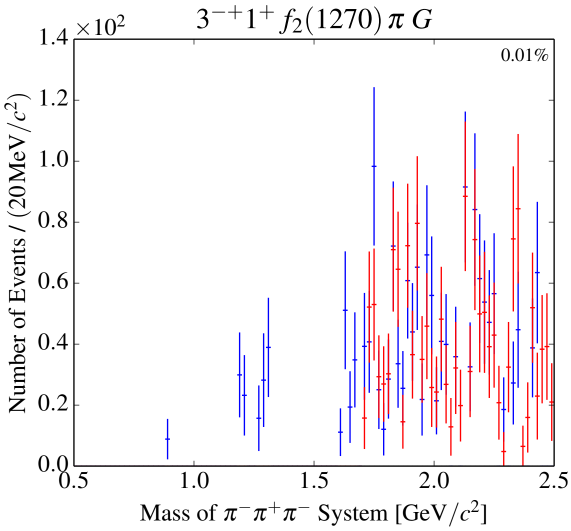

$3^{-+}1^{+}\,f_2(1270)\,\pi\,G$
0.01%
$\times10^2$
Number of Events / $(20\,\mathrm{MeV}/c^2)$
Mass of $\pi^-\pi^+\pi^-$ System [GeV/c^2]

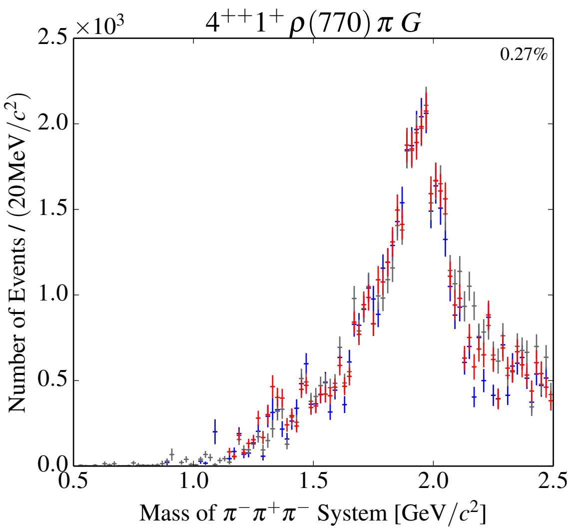

$4^{++}1^{+}\,\rho(770)\,\pi\,G$
0.27%
$\times10^3$
Number of Events / $(20\,\mathrm{MeV}/c^2)$
Mass of $\pi^-\pi^+\pi^-$ System [GeV/c^2]

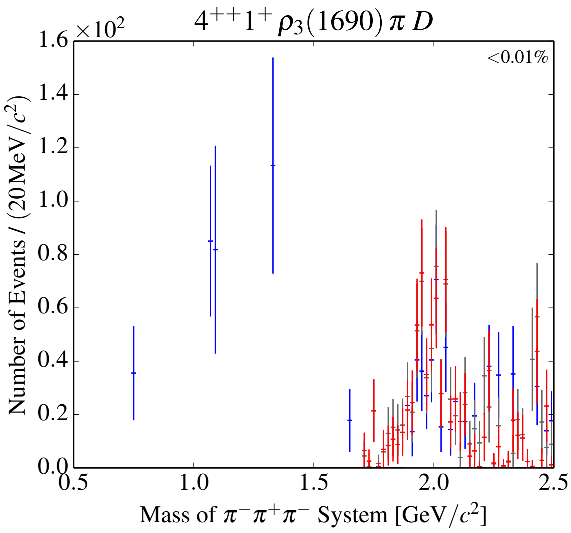

$4^{++}1^{+}\,\rho_3(1690)\,\pi\,D$
<0.01%
$\times10^2$
Number of Events / $(20\,\mathrm{MeV}/c^2)$
Mass of $\pi^-\pi^+\pi^-$ System [GeV/c^2]

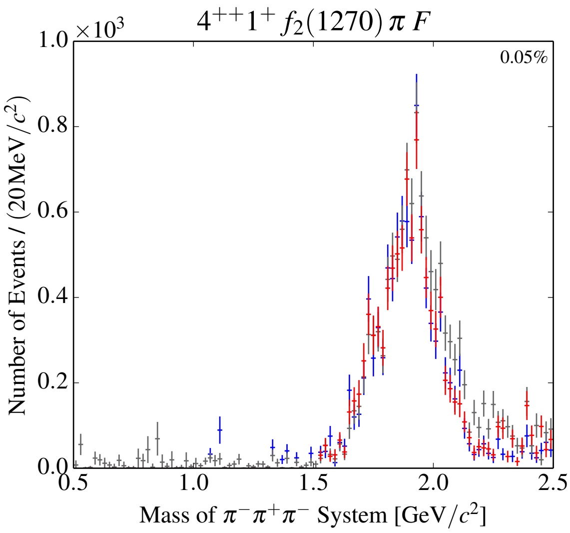

$4^{++}1^{+}\,f_2(1270)\,\pi\,F$
0.05%
$\times10^3$
Number of Events / $(20\,\mathrm{MeV}/c^2)$
Mass of $\pi^-\pi^+\pi^-$ System [GeV/c^2]

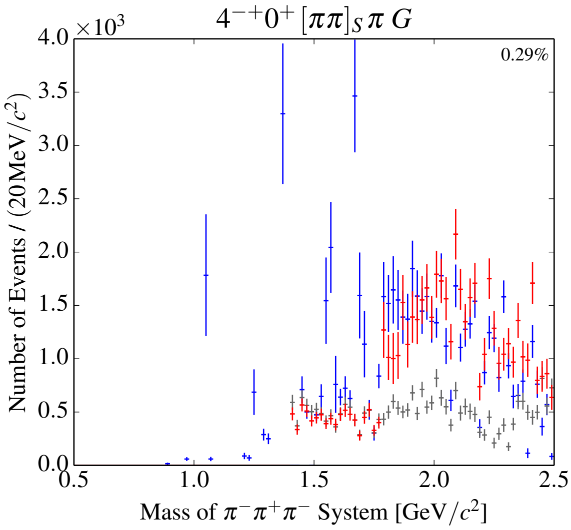

$4^{-+}0^{+}\,[\pi\pi]_S\,\pi\,G$
0.29%
$\times10^3$
Number of Events / $(20\,\mathrm{MeV}/c^2)$
Mass of $\pi^-\pi^+\pi^-$ System [GeV/c^2]

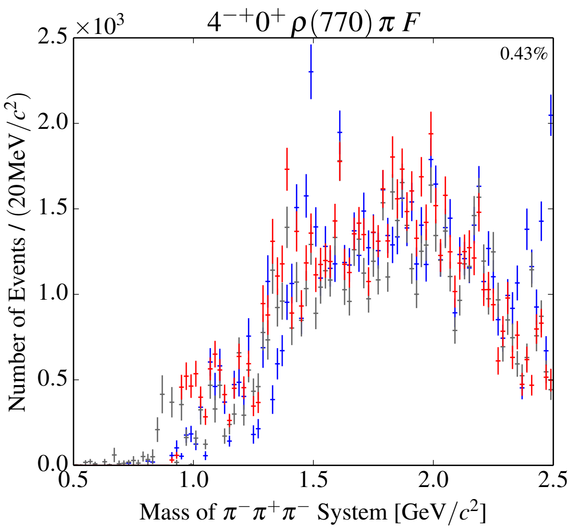

$4^{-+}0^{+}\,\rho(770)\,\pi\,F$
0.43%
$\times10^3$
Number of Events / $(20\,\mathrm{MeV}/c^2)$
Mass of $\pi^-\pi^+\pi^-$ System [GeV/c^2]

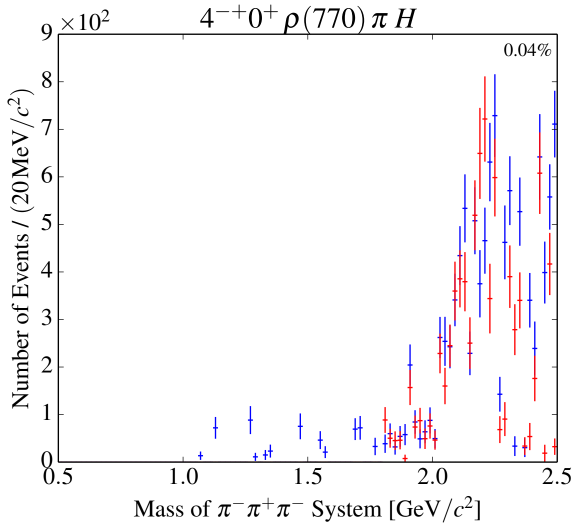
$4^{-+}0^{+}\ \rho(770)\,\pi\ H$
0.04%
$\times10^{2}$
Number of Events / (20MeV/c^2)
Mass of $\pi^-\pi^+\pi^-$ System [GeV/c^2]

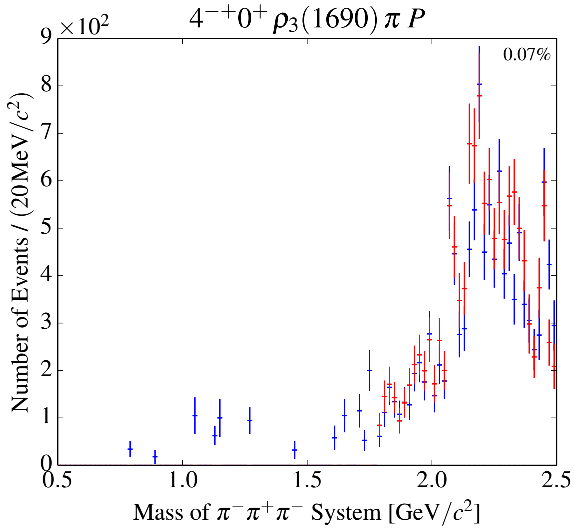
$4^{-+}0^{+}\ \rho_3(1690)\,\pi\ P$
0.07%
$\times10^{2}$
Number of Events / (20MeV/c^2)
Mass of $\pi^-\pi^+\pi^-$ System [GeV/c^2]

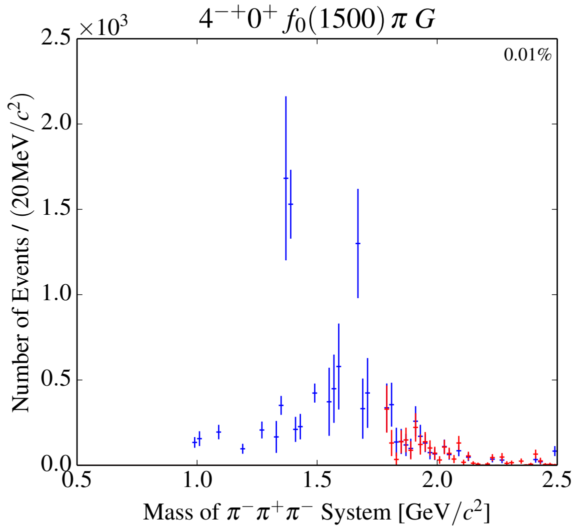
$4^{-+}0^{+}\ f_0(1500)\,\pi\ G$
0.01%
$\times10^{3}$
Number of Events / (20MeV/c^2)
Mass of $\pi^-\pi^+\pi^-$ System [GeV/c^2]

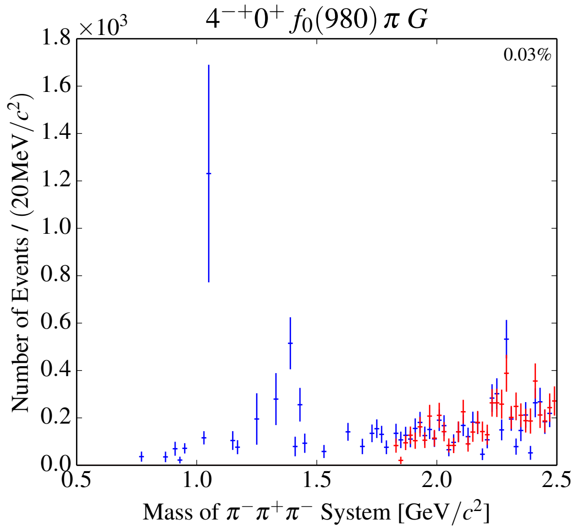
$4^{-+}0^{+}\ f_0(980)\,\pi\ G$
0.03%
$\times10^{3}$
Number of Events / (20MeV/c^2)
Mass of $\pi^-\pi^+\pi^-$ System [GeV/c^2]

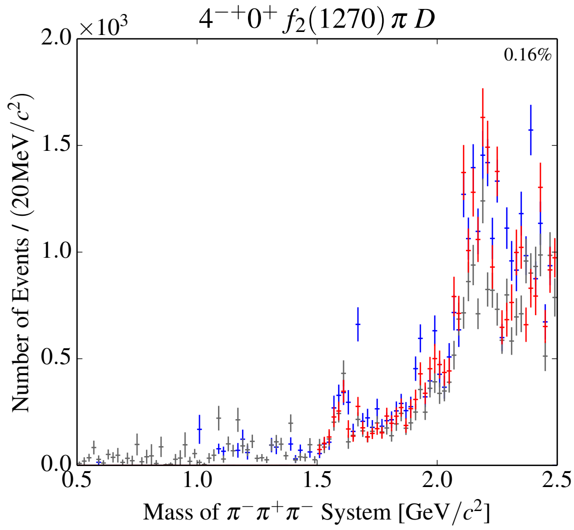
$4^{-+}0^{+}\ f_2(1270)\,\pi\ D$
0.16%
$\times10^{3}$
Number of Events / (20MeV/c^2)
Mass of $\pi^-\pi^+\pi^-$ System [GeV/c^2]

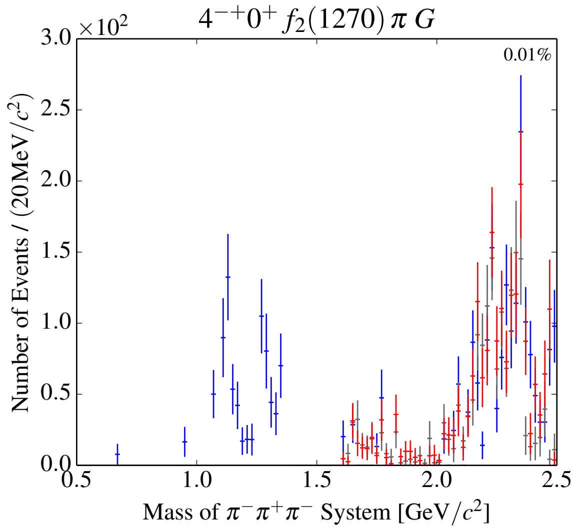
$4^{-+}0^{+}\ f_2(1270)\,\pi\ G$
0.01%
$\times10^{2}$
Number of Events / (20MeV/c^2)
Mass of $\pi^-\pi^+\pi^-$ System [GeV/c^2]

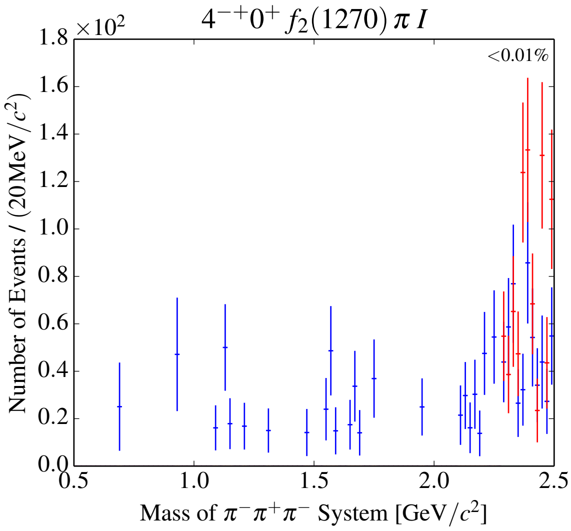
$4^{-+}0^{+}\, f_2(1270)\,\pi\, I$
$\times 10^2$
<0.01%
Number of Events / (20MeV/c^2)
Mass of $\pi^-\pi^+\pi^-$ System [GeV/c^2]

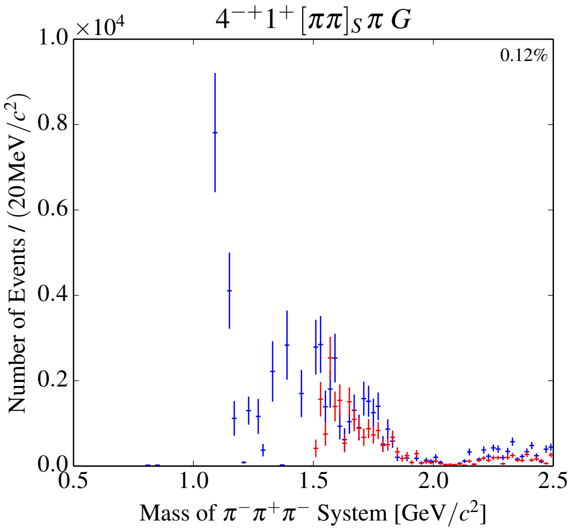
$4^{-+}1^{+}\, [\pi\pi]_S\,\pi\, G$
$\times 10^4$
0.12%
Number of Events / (20MeV/c^2)
Mass of $\pi^-\pi^+\pi^-$ System [GeV/c^2]

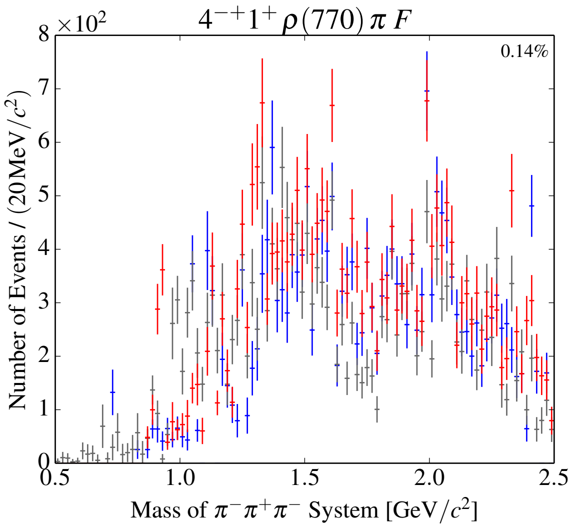
$4^{-+}1^{+}\, \rho(770)\,\pi\, F$
$\times 10^2$
0.14%
Number of Events / (20MeV/c^2)
Mass of $\pi^-\pi^+\pi^-$ System [GeV/c^2]

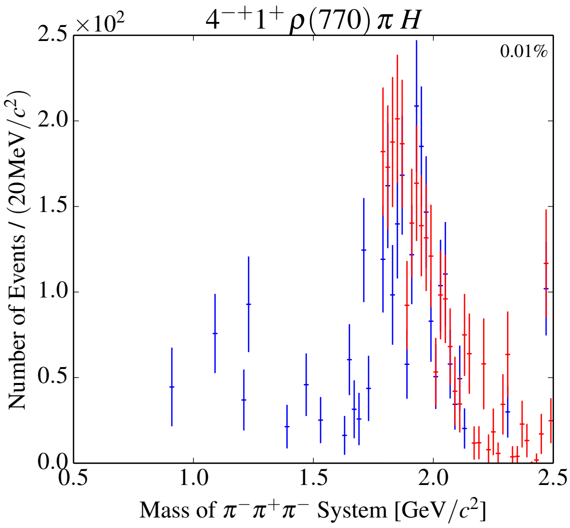
$4^{-+}1^{+}\, \rho(770)\,\pi\, H$
$\times 10^2$
0.01%
Number of Events / (20MeV/c^2)
Mass of $\pi^-\pi^+\pi^-$ System [GeV/c^2]

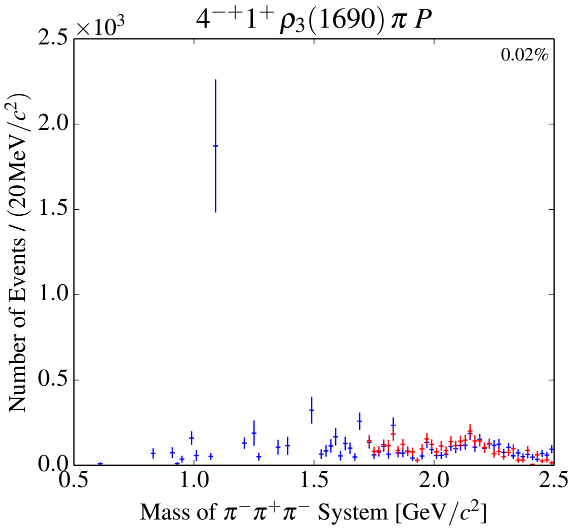
$4^{-+}1^{+}\, \rho_3(1690)\,\pi\, P$
$\times 10^3$
0.02%
Number of Events / (20MeV/c^2)
Mass of $\pi^-\pi^+\pi^-$ System [GeV/c^2]

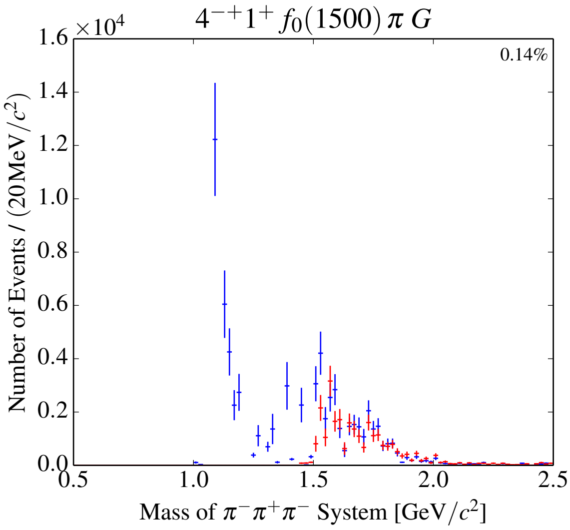
$4^{-+}1^{+}\, f_0(1500)\,\pi\, G$
$\times 10^4$
0.14%
Number of Events / (20MeV/c^2)
Mass of $\pi^-\pi^+\pi^-$ System [GeV/c^2]

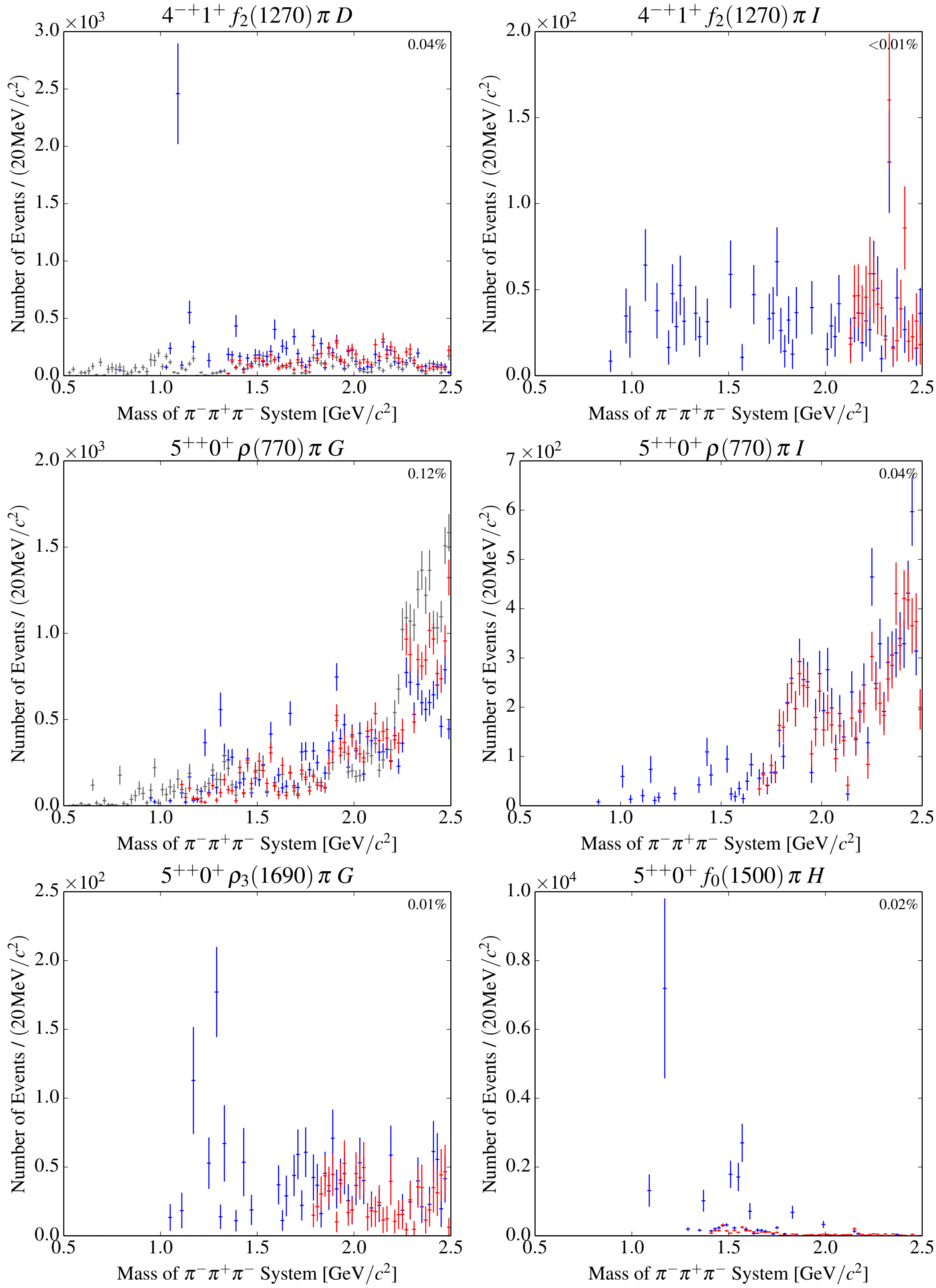
$4^{-+}1^{+}\, f_2(1270)\,\pi\, D$
0.04%
$4^{-+}1^{+}\, f_2(1270)\,\pi\, I$
<0.01%
$5^{++}0^{+}\, \rho(770)\,\pi\, G$
0.12%
$5^{++}0^{+}\, \rho(770)\,\pi\, I$
0.04%
$5^{++}0^{+}\, \rho_3(1690)\,\pi\, G$
0.01%
$5^{++}0^{+}\, f_0(1500)\,\pi\, H$
0.02%
Number of Events / (20MeV/c^2)
Mass of $\pi^-\pi^+\pi^-$ System [GeV/c^2]

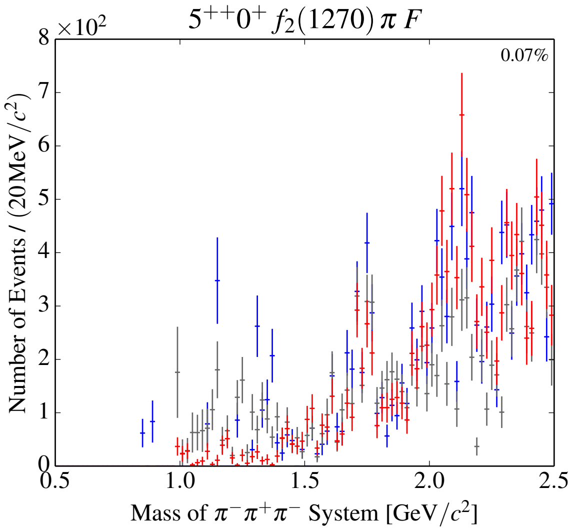
$5^{++}0^{+}\, f_2(1270)\, \pi\, F$
0.07%
$\times 10^2$
Number of Events / (20MeV/c^2)
Mass of $\pi^-\pi^+\pi^-$ System [GeV/c^2]

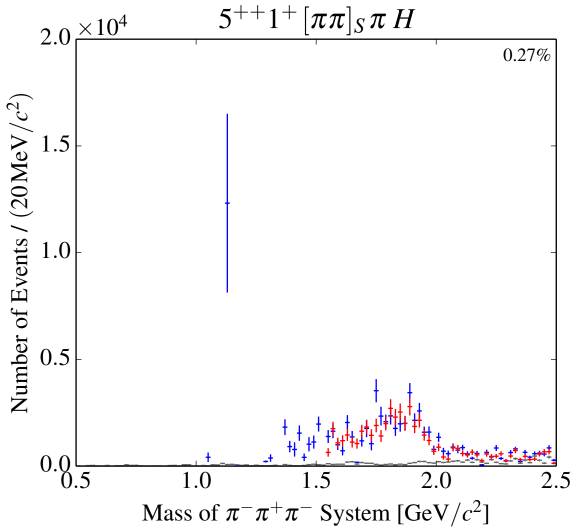
$5^{++}1^{+}\, [\pi\pi]_S\, \pi\, H$
0.27%
$\times 10^4$
Number of Events / (20MeV/c^2)
Mass of $\pi^-\pi^+\pi^-$ System [GeV/c^2]

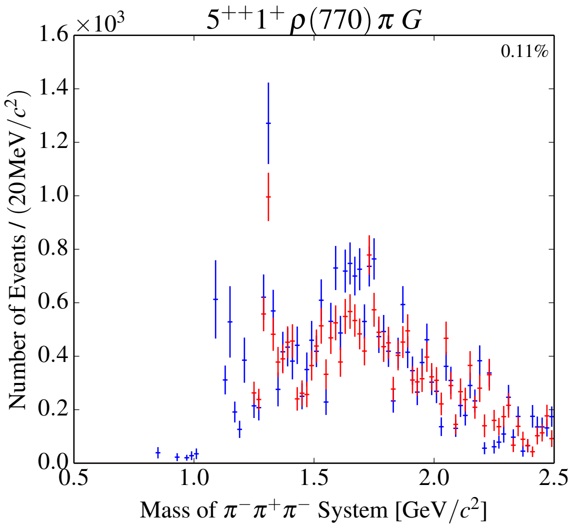
$5^{++}1^{+}\, \rho(770)\, \pi\, G$
0.11%
$\times 10^3$
Number of Events / (20MeV/c^2)
Mass of $\pi^-\pi^+\pi^-$ System [GeV/c^2]

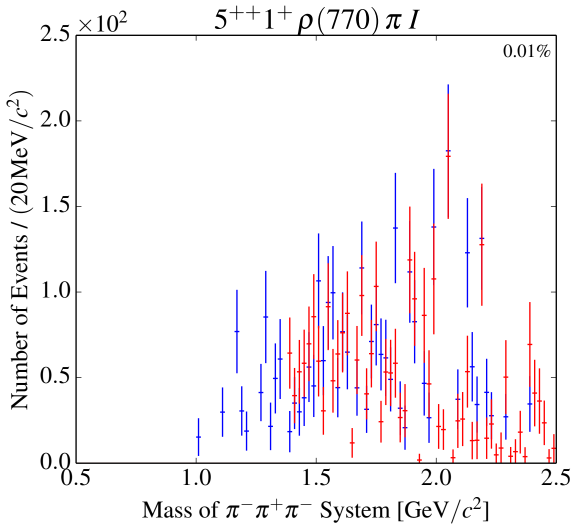
$5^{++}1^{+}\, \rho(770)\, \pi\, I$
0.01%
$\times 10^2$
Number of Events / (20MeV/c^2)
Mass of $\pi^-\pi^+\pi^-$ System [GeV/c^2]

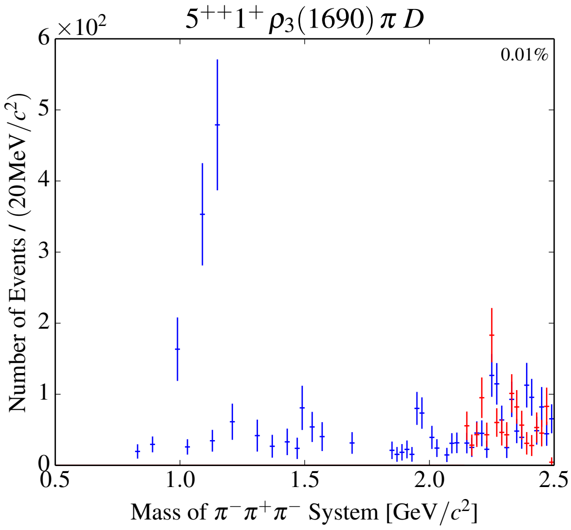
$5^{++}1^{+}\, \rho_3(1690)\, \pi\, D$
0.01%
$\times 10^2$
Number of Events / (20MeV/c^2)
Mass of $\pi^-\pi^+\pi^-$ System [GeV/c^2]

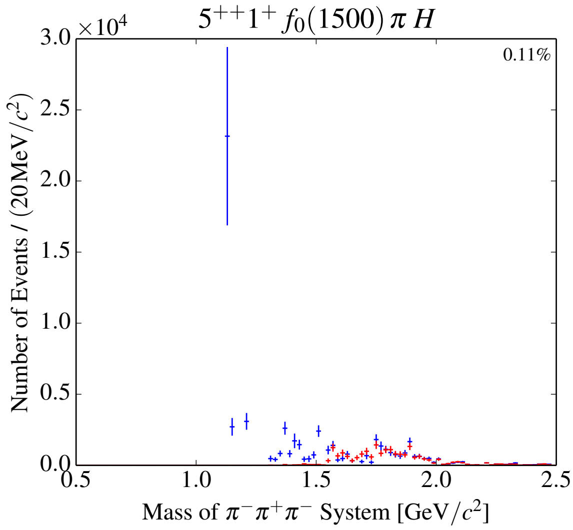
$5^{++}1^{+}\, f_0(1500)\, \pi\, H$
0.11%
$\times 10^4$
Number of Events / (20MeV/c^2)
Mass of $\pi^-\pi^+\pi^-$ System [GeV/c^2]

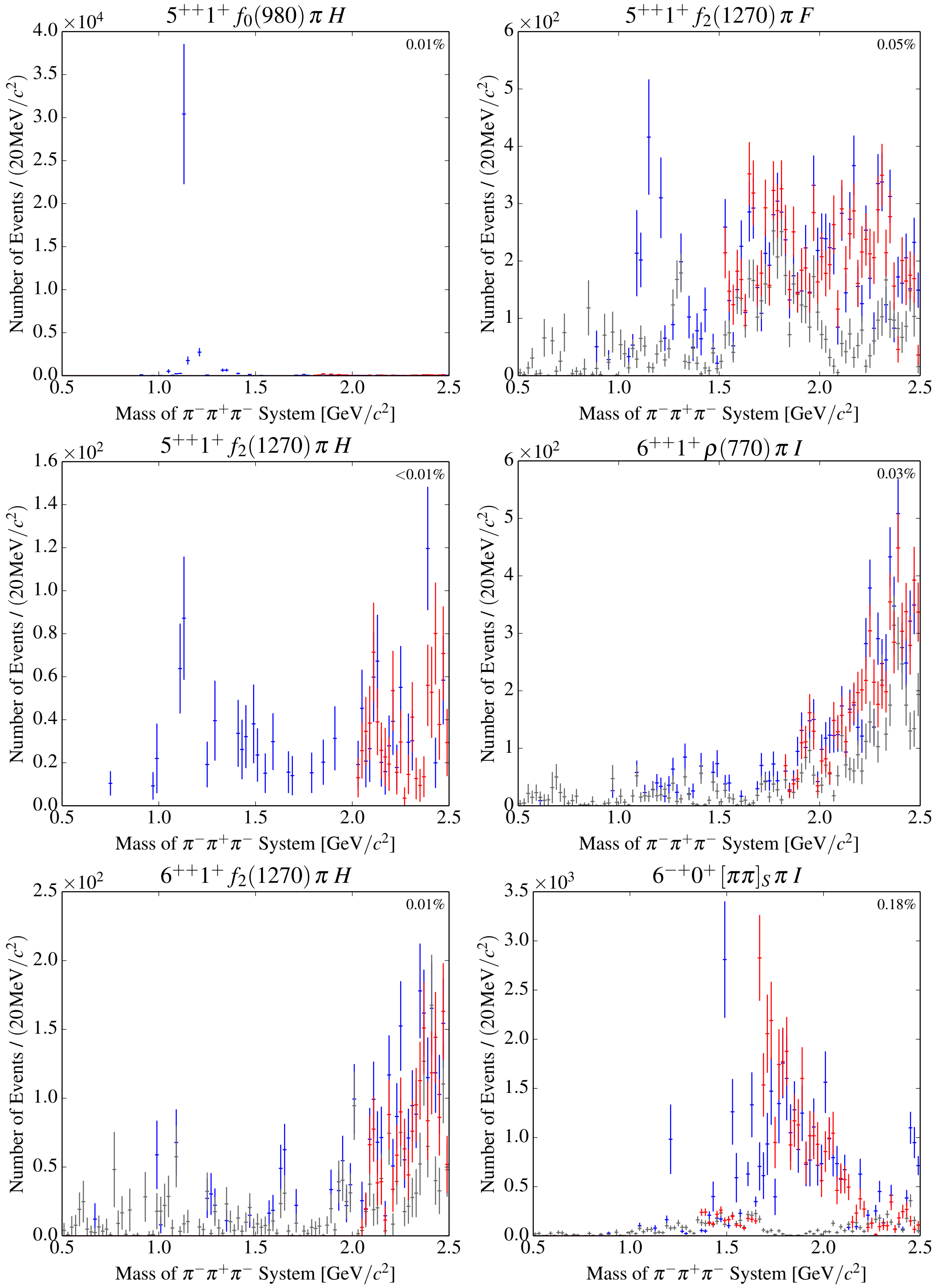
$5^{++}1^{+}\,f_0(980)\,\pi\,H$
$5^{++}1^{+}\,f_2(1270)\,\pi\,F$
$5^{++}1^{+}\,f_2(1270)\,\pi\,H$
$6^{++}1^{+}\,\rho(770)\,\pi\,I$
$6^{++}1^{+}\,f_2(1270)\,\pi\,H$
$6^{-+}0^{+}\,[\pi\pi]_S\,\pi\,I$
0.01%
0.05%
<0.01%
0.03%
0.01%
0.18%
Number of Events / (20MeV/c^2)
Mass of $\pi^-\pi^+\pi^-$ System [GeV/c^2]
$\times10^4$
$\times10^2$
$\times10^3$

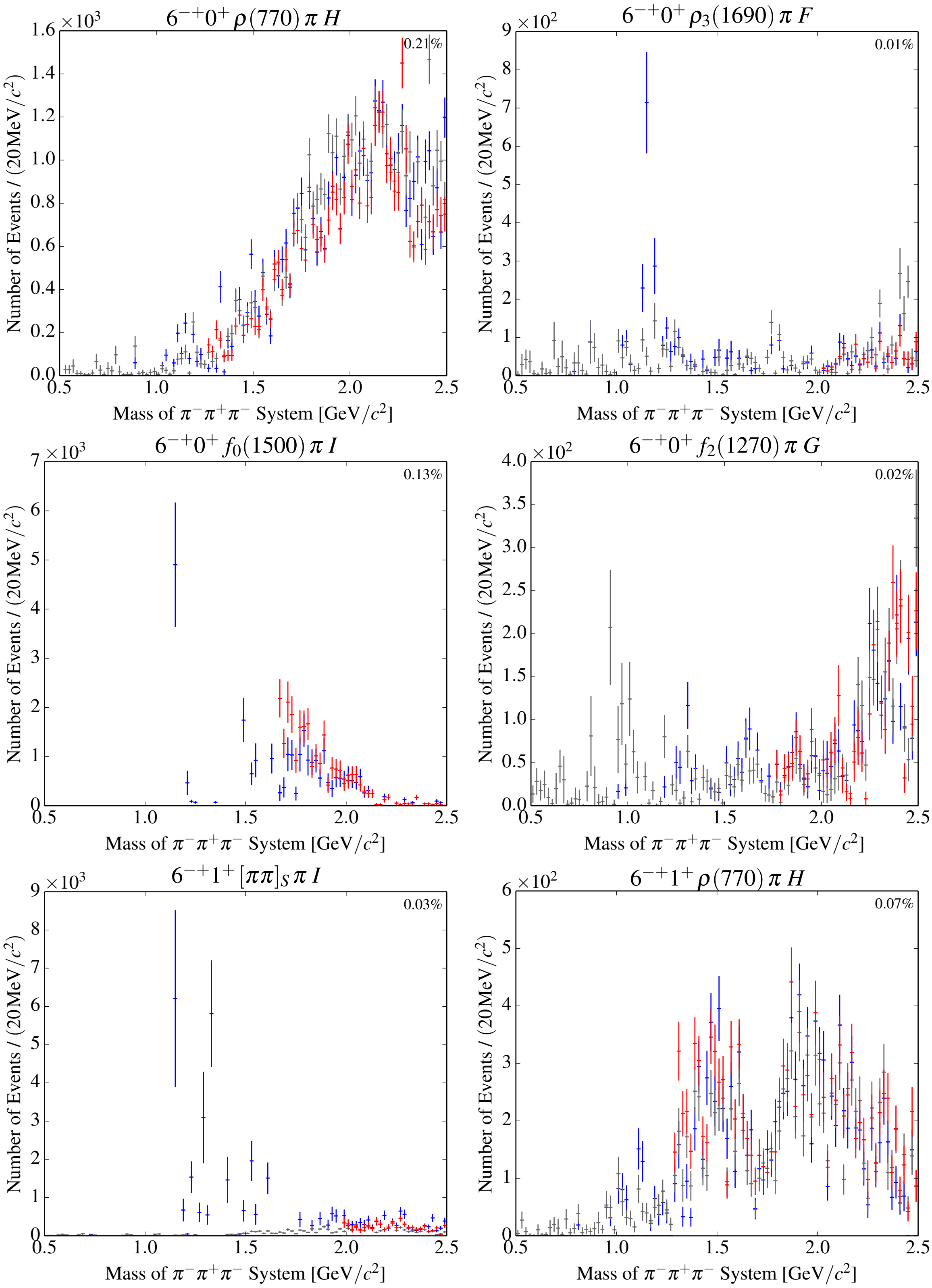
$6^{-+}0^{+}\,\rho(770)\,\pi\,H$
0.21%
$\times10^{3}$
Number of Events / (20MeV/c^2)
Mass of $\pi^-\pi^+\pi^-$ System [GeV/c^2]
$6^{-+}0^{+}\,\rho_3(1690)\,\pi\,F$
0.01%
$\times10^{2}$
$6^{-+}0^{+}\,f_0(1500)\,\pi\,I$
0.13%
$\times10^{3}$
$6^{-+}0^{+}\,f_2(1270)\,\pi\,G$
0.02%
$\times10^{2}$
$6^{-+}1^{+}\,[\pi\pi]_S\,\pi\,I$
0.03%
$\times10^{3}$
$6^{-+}1^{+}\,\rho(770)\,\pi\,H$
0.07%
$\times10^{2}$

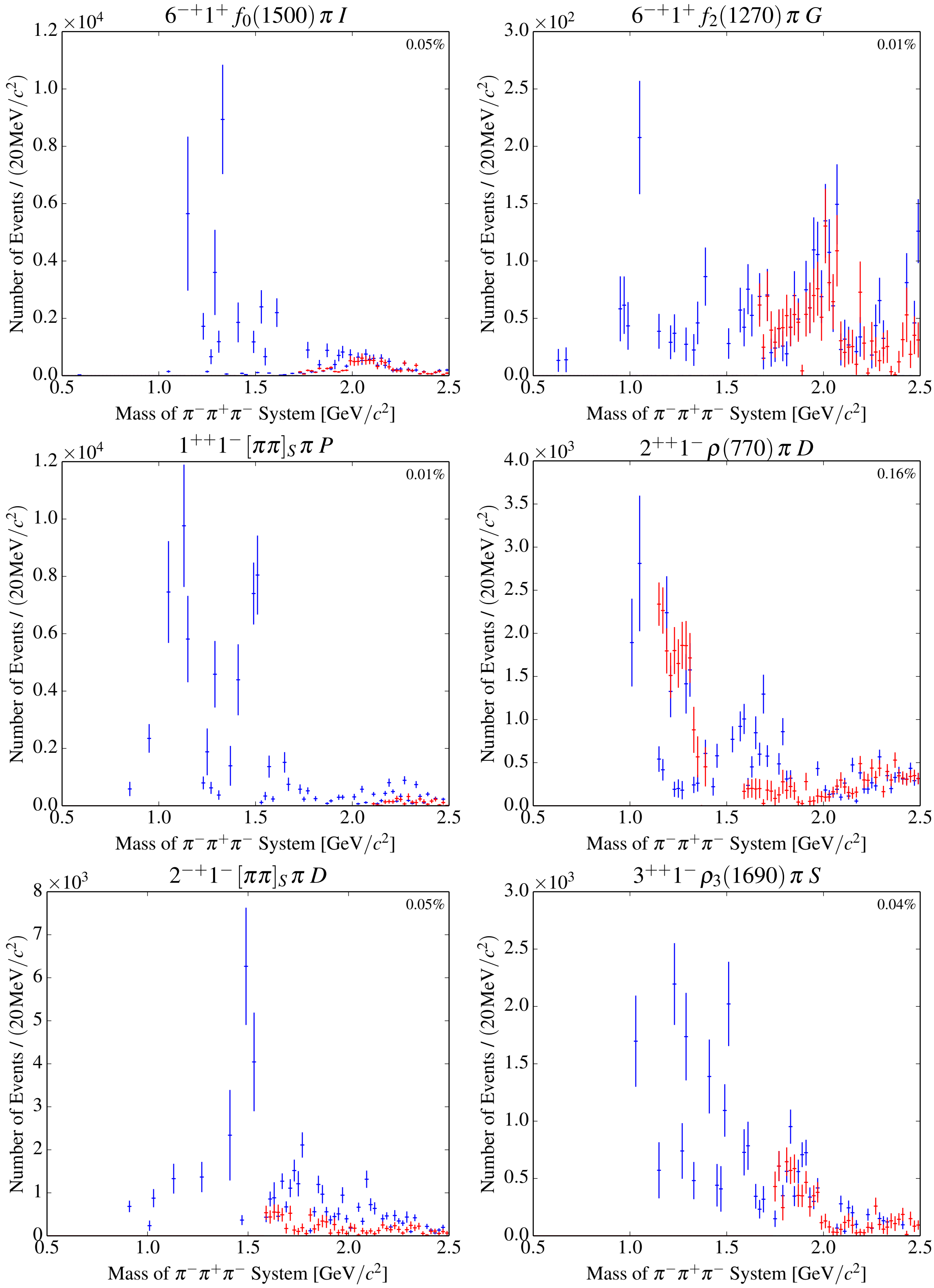

$6^{-+}1^{+}\ f_0(1500)\,\pi\ I$
0.05%
$6^{-+}1^{+}\ f_2(1270)\,\pi\ G$
0.01%
$1^{++}1^{-}\ [\pi\pi]_S\,\pi\ P$
0.01%
$2^{++}1^{-}\ \rho(770)\,\pi\ D$
0.16%
$2^{-+}1^{-}\ [\pi\pi]_S\,\pi\ D$
0.05%
$3^{++}1^{-}\ \rho_3(1690)\,\pi\ S$
0.04%
Number of Events / (20MeV/c^2)
Mass of $\pi^-\pi^+\pi^-$ System [GeV/c^2]

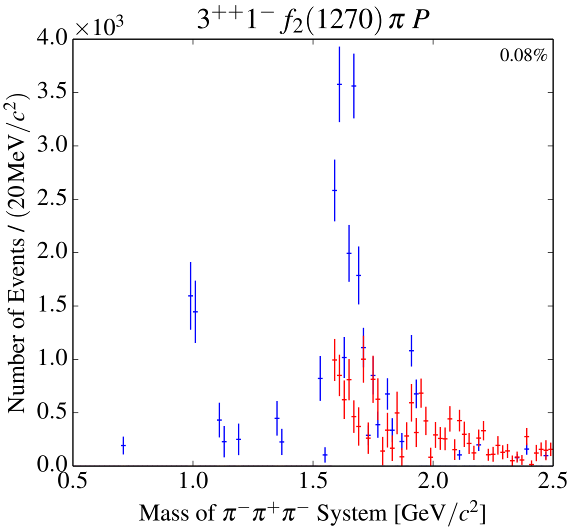
$3^{++}1^{-}\ f_2(1270)\,\pi\ P$
0.08%
$\times 10^3$
Number of Events / (20MeV/c^2)
Mass of $\pi^-\pi^+\pi^-$ System [GeV/c^2]

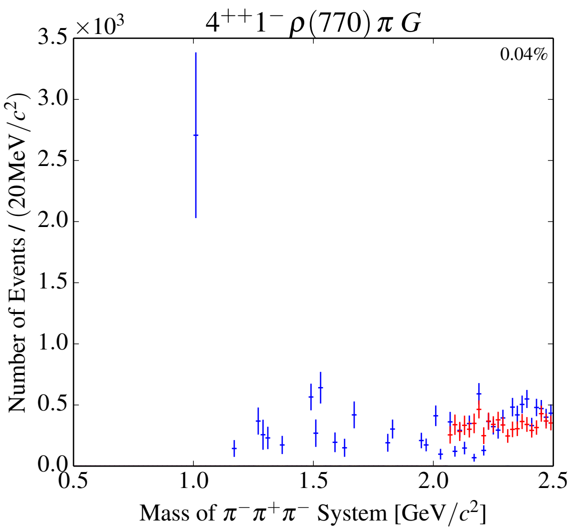
$4^{++}1^{-}\ \rho(770)\,\pi\ G$
0.04%
$\times 10^3$
Number of Events / (20MeV/c^2)
Mass of $\pi^-\pi^+\pi^-$ System [GeV/c^2]

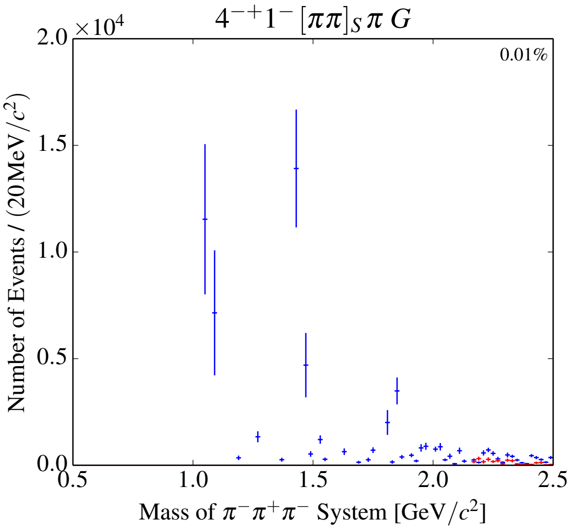
$4^{-+}1^{-}\ [\pi\pi]_S\,\pi\ G$
0.01%
$\times 10^4$
Number of Events / (20MeV/c^2)
Mass of $\pi^-\pi^+\pi^-$ System [GeV/c^2]

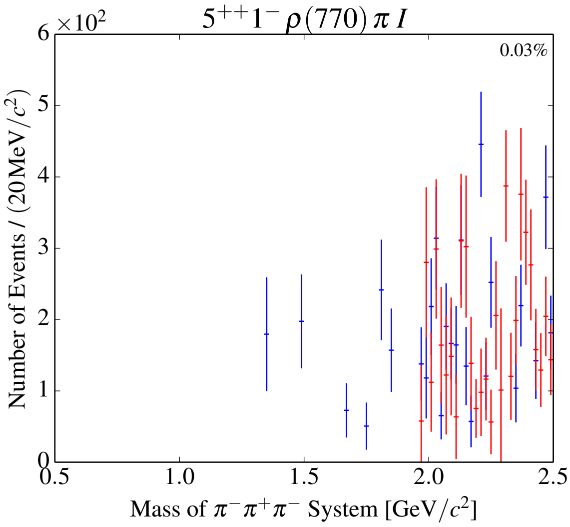
$5^{++}1^{-}\ \rho(770)\,\pi\ I$
0.03%
$\times 10^2$
Number of Events / (20MeV/c^2)
Mass of $\pi^-\pi^+\pi^-$ System [GeV/c^2]

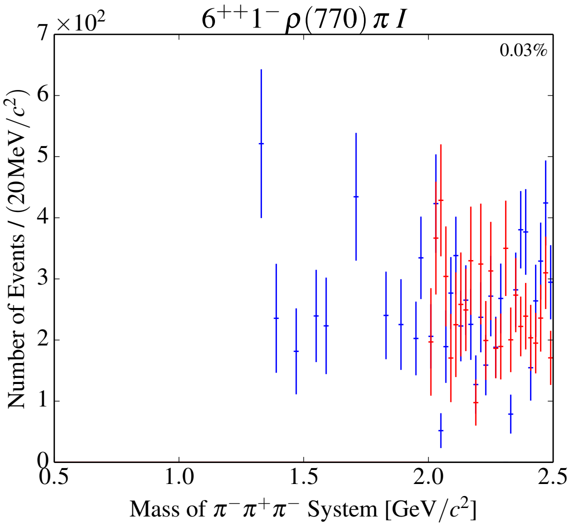
$6^{++}1^{-}\ \rho(770)\,\pi\ I$
0.03%
$\times 10^2$
Number of Events / (20MeV/c^2)
Mass of $\pi^-\pi^+\pi^-$ System [GeV/c^2]

Bibliography

[1] G. P. Lepage, "Lattice QCD for novices," *Strong interactions at low and intermediate energies. Proceedings, 13th Annual Hampton University Graduate Studies, HUGS'98, Newport News, USA, May 26-June 12, 1998*, 1998 49–90, arXiv: hep-lat/0506036 [hep-lat]. (Cited on page 3)

[2] R. T. Deck, "Kinematical Interpretation of the First $\pi - p$ Resonance," Phys. Rev. Lett. **13** (5 1964) 169–173, URL: http://link.aps.org/doi/10.1103/PhysRevLett.13.169. (Cited on pages 7, 46)

[3] F. Haas, "Two-Dimensional Partial-Wave Analysis of Exclusive 190 GeV $\pi^- p$ Scattering into the $\pi^-\pi^-\pi^+$ Final State at COMPASS (CERN)," PhD thesis: Munich, Tech. U., 2014, URL: http://inspirehep.net/record/1296581/files/949072551_CERN-THESIS-2013-277.pdf. (Cited on pages 9, 10, 12, 13, 19, 32, 43, 45, 67, 68)

[4] P. Abbon et al., "The COMPASS Setup for Physics with Hadron Beams," Nucl. Instrum. Meth. **A779** (2015) 69–115, arXiv: 1410.1797 [physics.ins-det]. (Cited on page 9)

[5] COMPASS collaboration, "Resonance Production and $\pi\pi$ S-wave in $\pi^- + p \to \pi^-\pi^-\pi^+ + p_{\text{recoil}}$ at $190\,\text{GeV}/c$," (to be published) (2015). (Cited on pages 11–15, 19–21, 32, 35, 45, 67, 68)

[6] P. Abbon et al., "The COMPASS Setup for Physics with Hadron Beams," Nucl. Instrum. Meth. **A779** (2015) 69–115, arXiv: 1410.1797 [physics.ins-det]. (Cited on page 11)

[7] K. Bicker, "Model Selection for and Partial-Wave Analysis of a Five-Pion Final State at the COMPASS Experiment at CERN," PhD thesis: Munich, Tech. U., 2015. (Cited on pages 13, 16, 45, 69)

[8] J. Blatt and V. Weisskopf, *Theoretical nuclear physics*, Wiley, 1952, URL: https://books.google.de/books?id=0f1QAAAAMAAJ. (Cited on pages 17, 19)

[9] F. von Hippel and C. Quigg, "Centrifugal-Barrier Effects in Resonance Partial Decay Widths, Shapes, and Production Amplitudes," Phys. Rev. D **5** (3 1972) 624–638,
URL: http://link.aps.org/doi/10.1103/PhysRevD.5.624. (Cited on page 17)

[10] G. Breit and E. Wigner, "Capture of Slow Neutrons," Phys. Rev. **49** (7 1936) 519–531,
URL: http://link.aps.org/doi/10.1103/PhysRev.49.519. (Cited on page 19)

[11] S. Flatté, "On the nature of 0+ mesons," Physics Letters B **63**.2 (1976) 228–230,
ISSN: 0370-2693,
URL: http://www.sciencedirect.com/science/article/pii/0370269376906559.
(Cited on page 19)

[12] M. Ablikim et al., "Resonances in and," Physics Letters B **607**.3–4 (2005) 243–253,
ISSN: 0370-2693,
URL: http://www.sciencedirect.com/science/article/pii/S0370269304017265.
(Cited on pages 19, 21)

[13] K. L. Au, D. Morgan, and M. R. Pennington,
"Meson dynamics beyond the quark model: Study of final-state interactions,"
Phys. Rev. D **35** (5 1987) 1633–1664,
URL: http://link.aps.org/doi/10.1103/PhysRevD.35.1633. (Cited on page 19)

[14] S. Wallner, "Extraction of Resonance Parameters of Light Meson Resonances in the Charged Three-Pion Final State at the COMPASS Experiment (CERN)," MA thesis: TU Munich, 2015.
(Cited on pages 24, 45, 49)

[15] S. Schmeing, "Resonance Extraction in Diffractive 3π Production using 190 GeV/c π^- at the COMPASS Experiment (CERN)," MA thesis: TU Munich, 2014. (Cited on pages 24, 45, 49)

[16] J. Nocedal, "Updating Quasi-Newton Matrices with Limited Storage,"
Mathematics of Computation **35**.151 (1980) 773–782,
URL: http://www.jstor.org/stable/2006193. (Cited on page 25)

[17] D. C. Liu and J. Nocedal,
"On the Limited Memory BFGS Method for Large Scale Optimization,"
Math. Program. **45**.3 (1989) 503–528, ISSN: 0025-5610,
URL: http://dx.doi.org/10.1007/BF01589116. (Cited on page 25)

[18] D. Amelin et al., "Study of resonance production in diffractive reaction $\pi^- A \to \pi^+\pi^-\pi^- A$," Physics Letters B **356**.4 (1995) 595–600, ISSN: 0370-2693,
URL: http://www.sciencedirect.com/science/article/pii/037026939500864H.
(Cited on page 43)

[19] K. Bicker, personal communication, 2015. (Cited on page 69)

List of Figures

List of Tables

Acknowledgements

First of all I would like to thank Stephan Paul for the possibility to work on this interesting thesis.

Many thanks go to Boris Grube and Karl Bicker for guiding me for this whole year. I very much appreciate all the time you spent to help me, no matter how small the problem. I also appreciate all the gummy bears, beef jerky, M&Ms and Flugzeuge. I would also like to thank Sebastian Uhl, for magically fixing everything, no matter what you throw at him. Your regex magic will haunt me for years.

I would also like to thank my officemates Stefan Huber, Tillmann Mayer, Dmytro Levit and, for a much too short time, Alexander Austregesilo for the always nice atmosphere. I sincerely thank everyone working at E18, it was a pleasure to work here.

Special thanks to my dear friends Bernhard Hohlweger and Tillmann Gaida. I will look forward to your acknowledgements, if you make it. Also thank you Konstantin Sabaß for saving my studies. I will never forget.

Vielen, vielen Dank geht an meine Eltern. Ihr seid sehr geduldig mit mir und ich weiß das zu schätzen. Ich liebe euch.

And last but not least, my sincerest thanks go to my wife Maxi for always being there for me. I will return the favour.